Biomechanical analysis and modeling of contact interface as applied in tonometry and bio-inspired skin sensors

A Dissertation Presented

by

Jun Nishiyama

to

The Graduate School

in Partial Fulfillment of the

Requirements

for the Degree of

Doctor of Philosophy

in

Mechanical Engineering

Stony Brook University

August 2014

Stony Brook University

The Graduate School

Jun Nishiyama

We, the dissertation committee for the above candidate for the
Doctor of Philosophy degree,
hereby recommend acceptance of this dissertation.

Dr. Imin Kao, Advisor
Mechanical Engineering, SUNY at Stony Brook

Dr. Robert Kukta
Mechanical Engineering, SUNY at Stony Brook

Dr. David Hwang
Mechanical Engineering, SUNY at Stony Brook

Dr. Mary D. Frame
Biomedical Engineering, SUNY at Stony Brook

This dissertation is accepted by the Graduate School

Charles Taber
Dean of the Graduate School

Abstract of the Dissertation

Biomechanical analysis and modeling of contact interface as applied in tonometry and bio-inspired skin sensors

by

Jun Nishiyama

Doctor of Philosophy

in

Mechanical Engineering

Stony Brook University

2014

The modeling of contact interface, in which two entities are brought to interact with each other, either through direct contact or non-direct contact, is crucial in the understanding of robotics and biomedical research where such interface will determine important engineering properties. The modeling and analysis of direct contact interface and non-direct interface are studied in this dissertation, as applied in tonometry (non-contact) and skin sensors (contact). The stiffness of human organs or tissues is an important factor for medical diagnoses, and the accurate measurement of contact properties are very important. For instance, cancerous tissue has higher stiffness, and stiffer eyeballs with higher Intra-Ocular Pressure (IOP) have higher risk of glaucoma. In principle, the stiffness is estimated by measuring the deformation due to an applied force. Tonometry refers to a technique to measure the IOP of eyes, including that with a direct contact, such as the Goldman Applanation tonometry, or non-direct contact, such as the air-puff tonometry. The non-direct contact interface in the air-puff tonometry is analyzed and modeled to enhance the accuracy of IOP measurement in this dissertation. In addition, human organs or tissues demonstrate time-dependent responses of viscoelastic phenomena which affect the estimation of the stiffness and other engineering properties. Furthermore, prototypes of artificial skin, inspired by human skin, are fabricated to study the viscoelastic property and other engineering properties by different types of stimuli. The responses are also compared with those of biological skins in the context of interface with direct contact.

Table of Contents

List of Figures

List of Tables

List of Abbreviations

Abbreviation	Description
c	Viscous damping coefficient
CCT	Central cornea thickness
CL	Contact lenses
CNT	Carbon nanotube
D	Diopter (the power of lenses)
DOF	Degree of Freedom
F	Force
FEM	Finite element method
GAT	Goldmann applanation tonometer
IOP	Intra-Ocular pressure
k	Spring constant
LS	Least-squares
m	Mass
NCL	No contact lenses
NCT	Non-contact tonometer
R	Electric resistance
2D	two-dimensional

Acknowledgements

First and foremost, I would like to express my appreciation to my advisor, Professor Imin Kao, for his guidance and encouragement throughout this research. Professor Kao's expert insights into the subjects of robotics and contact modeling provided the inspiration for my research. I would also like to thank him for providing me with a comfortable and supportive research environment.

It is my pleasure to acknowledge Professor Robert Kukta, Professor David Hwang, and Professor Marry Frame for taking on the responsibilities of being on my dissertation reading committee. I heartily appreciate their efforts in reading through my dissertation and providing comments and criticisms despite their busy schedules. I am especially grateful to Professor Makoto Kaneko and Professor Hwang for their support and providing me with their laboratories for conducting experimental studies. Many thanks are also due to Professor Hirai Shinichi, Dr. Van Ho, and Professor Mitsuru Higashimori for fruitful discussions.

I have particularly enjoyed the friendship and many thought-provoking discussions with my colleagues, Dylan Tsai, Paul Arauz, Mika Lai, and others in the lab. The road in pursuing the Ph.D. program would not be as smooth without the support from all the friends I have met at Stony Brook.

Last but not least, I would like to express my love and gratitude to my family. Their continuous encouragement has helped me push through these learning and trying years. Without their spiritual support, this dissertation would not have been possible.

Chapter 1

Introduction

Biomechanical analysis and modeling of contact interface help to provide accurate stiffness-based medical diagnoses and give us inspiration for new design of tactile sensors. Stiffness is an important factor in pathology as abnormal stiffness properties of tissue can be a sign of diseases. For instance, tumor tissue is usually stiffer than normal tissue and the excessive stiffness of the eyeball because of higher Intra-Ocular Pressure (IOP) can signal high risk for glaucoma. Therefore, accurate measurement of the stiffness is very important in medical diagnosis.

In a physical examination, physicians may touch patient's body and make diagnoses based on the sense of touch. This diagnosis is called palpation. Human fingertips are incredibly sensitive and the palpation gives a lot of information. However, medical doctors interpret the information by their intuitive experience and not by quantifying the information. The diagnosis by experienced physician is versatile but its weak points are universality and objectivity supported by numerical data. Biomechanical analysis and modeling of the contact interface, by using an external force and measuring the resulting displacement to estimate the stiffness, can help to improve the measurements of the stiffness of human organs and tissues to complement physician's expertise.

The contact interface onto which the external force is applied has two types as shown in Fig. 1.1: (a) direct contact interface, and (b) indirect contact interface. In the direct contact interface, the external force is applied by a solid object, such as a probe, as shown in Fig. 1.1(a). In the indirect contact interface, the external force is applied by a liquid or gas, such as water or air, as shown in Fig. 1.1(b). The direct contact interface can utilize various types of sensors in the tip of the probe to accurately measure the contact force. The indirect contact interface typically has lower risk in damaging tissues due to unexpected stress/strain concentration. Both types of contact interfaces have advantages and disadvantages. The choice of which type to use will be determined by the situation.

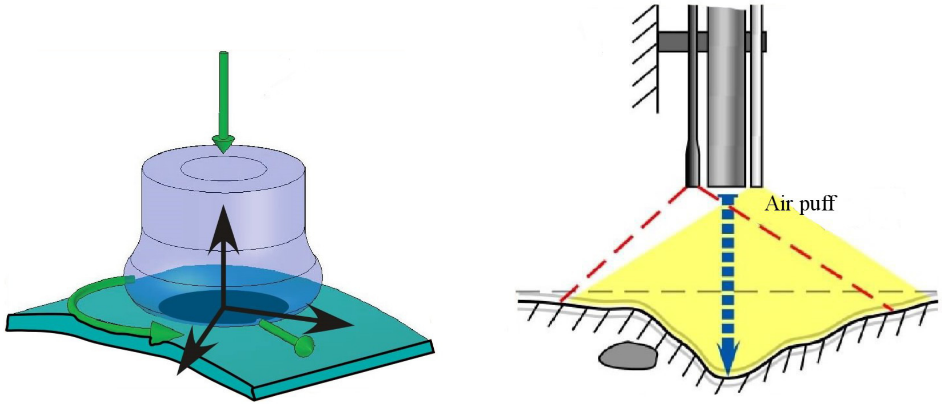

(a) Direct contact interface (b) Indirect contact interface

Figure 1.1: Direct/Indirect contact interfaces

The contact interface with soft materials, such as human organs or tissues, may have complex deformation pattern and pressure distribution, such as that shown in Fig. 1.1(b). Thus, modeling and analysis of contact interface is necessary to estimate the stiffens based on the deformation due to an external force. Unlike linear elastic material for which the Hooke's Law will apply, the biomechanical and soft materials are typically nonlinear, and hence more complex to model. In addition, human organs and tissues are viscoelastic and exhibit time-dependent viscoelastic responses, as described by Y. C. Fung [6] in 1993, which can be ignored in elastic materials such as steel. Therefore, the analysis and modeling of contact interface is necessary to improve the biomedical diagnosis.

In this dissertation, both direct and indirect contact interfaces are studied. In Chapters 2 and 3, the IOP (pressure and stiffness of eyeballs) measurement which includes both direct and indirect contact interfaces is studied. In Chapters 4-7, bio-inspired artificial skin sensor which includes direct contact interface is studied. Thereafter, in Chapter 8, the contribution of this research for better quality of life is presented. Finally, future work is proposed in Chapter 9.

1.1 Introduction of IOP measurement

IOP measurement is categorized into invasive or non-invasive means of measurement. The non-invasive method is further categorized into contact or non-contact tonometry, as illustrated in Fig. 1.2. The invasive measurement is conducted by inserting a needle into the eyeball and directly measuring the pressure. This method is arguably the most accurate. However, this method can only be used as a part of a surgical procedure because inserting a needle can cause some damage on tissues. Such invasive measurement is excessive and cannot be used as a regular means of IOP measurement. In the non-invasive measurement, external force is applied on the eyeball to estimate the internal pressure (IOP) either through direct contact or indirect contact interface. The direct contact measurement, such as the Goldmann applanation tonometry, applies an external force by a probe to measure the IOP. The non-contact measurement, such as an air-puff tonometer, applies an external

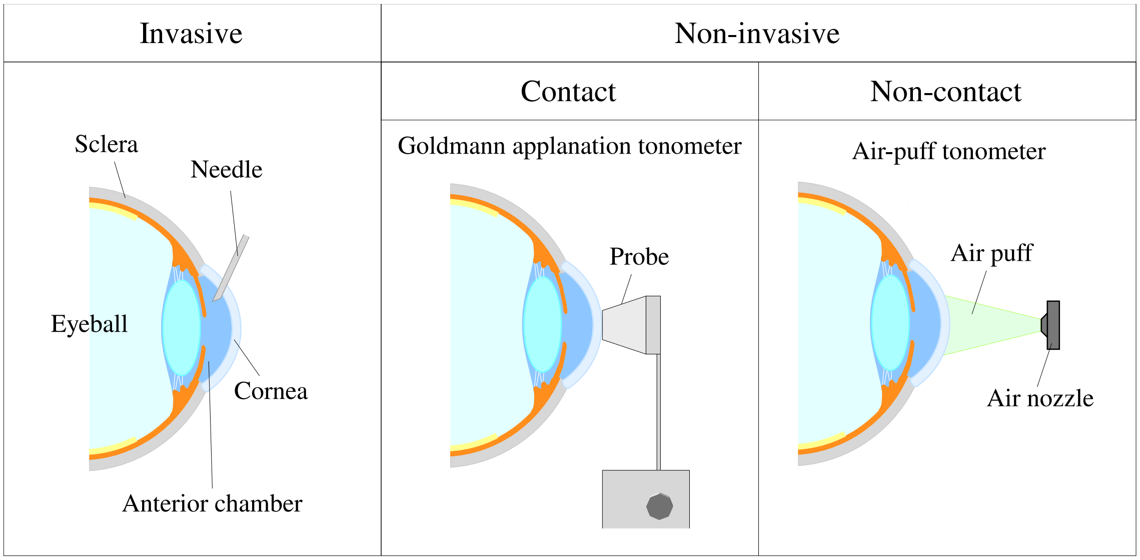

Figure 1.2: The category of tonometries

force by air puff. The air-puff tonometry is less accurate than the Goldmann applanation tonometry. However, the non-contact tonometry is easier to operate because anesthesia and rigorous sterilization are not necessary. Thus, the air-puff tonometry is often used by optometrists to measure IOP.

It has been widely suggested that many factors, such as mechanical properties of the cornea, can affect the IOP measurement. Most studies in this area are conducted by statistical analysis with the results which are not consistent to each other. It appears that one reason for such inconsistency may be due to the difficulty to conduct parameter study by varying only one parameter while keeping other parameters the same when working with human subjects. For instance, changing only the elasticity of the cornea and measuring IOP to determine the effect of the elasticity of the cornea on IOP measurement is unrealistic with human subjects. In addition, different subjects may have different corneal elasticity while other parameters, such as thickness and curvature, are also different. With an accurate mechanical model, one can conduct simulation of parameter study to understand the effect of a specific parameter on the results.

In Chapter 2, the effect of wearing contact lenses on IOP measurement by air-puff tonometry is studied. In Chapter 3, the human eyeball is modeled with discrete mass, damper, and spring system, and the deformation of eyeball due to externally applied force is modeled and analyzed by the linear system theory.

1.2 Introduction of Bio-inspired skin sensor

Artificial skin sensors which are as sensitive and durable as human fingertips can improve the grasping and dexterous manipulations of robot hands. Human fingertips are incredibly sensitive when tracing a surface with small force and can detect a tiny step less than few micrometers height and at the same time durable when strongly grasping an object although the sensitivity is decreased. It is also known that humans are controlling the grasping force by detecting the initiation of slip between fingertips and the target objects. In order to design artificial skin sensors, anatomically analyzing human skin can give us inspiration. Human skin is composed of epidermis, dermis, and different types of mechanoreceptors which have different shapes and configurations as shown in Fig 1.3. Literature on this field shows that epidermis and dermis will amplify and filter stimuli, and each mechanoreceptor detects the different types of stimuli.

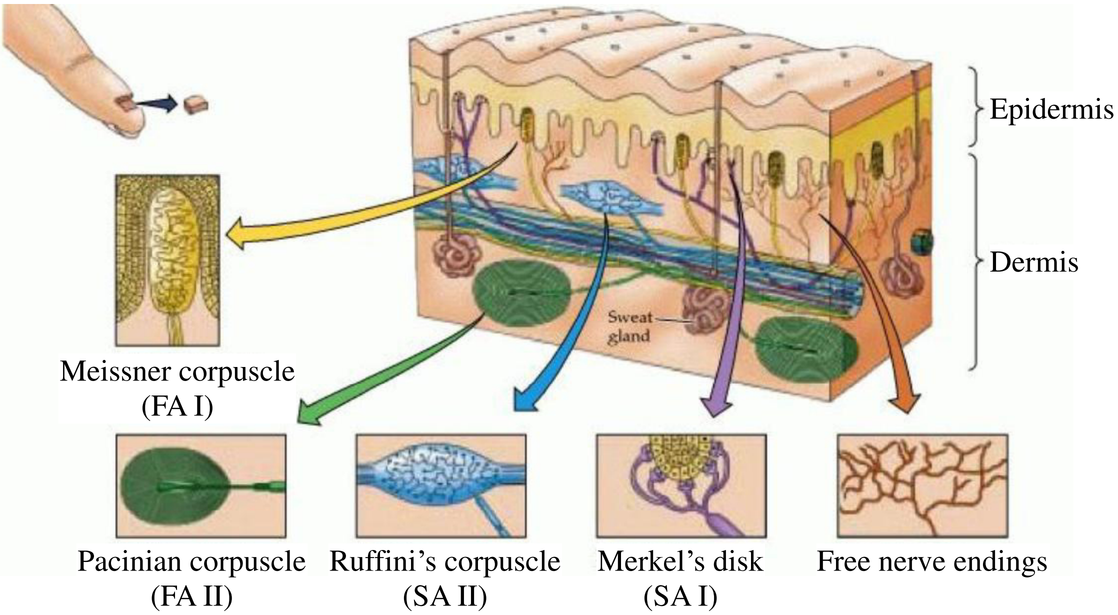

Figure 1.3: The cross section of human finger [1]

Therefore, different types of tactile sensors are fabricated and tested with different types of stimuli. In Chapter 4, an artificial skin sensor is fabricated by silicone rubber with embedded strain gages. Silicone materials have mechanical properties similar to human skin and strain gages are used to mimic mechanoreceptors. The sensor is evaluated under static and dynamic stimuli typically found at contact interface. It is observed during the experiments that the stiffness mismatch between the strain gages and silicone can cause complex strain concentration, and sometimes this may result in unreasonable deviation from the known patterns. In addition, the strain gages can be delaminated from silicone if large deformation is repeatedly applied. CNT based tactile sensor is a prominent candidate to solve the problems. Therefore, in Chapter 6, a prototype of tactile sensor based on carbon nanotubes (CNTs) is fabricated. In Chapter 7, the artificial fingertips composed of a hard core covered with soft artificial skin are studied.

Chapter 2

A theoretical analysis of the effect of wearing soft contact lenses on non-contact tonometry

2.1 Introduction

Accurate measurement of the intra-ocular pressure (IOP) is indispensable for ocular examinations, especially for preventing glaucoma. IOP is the internal fluid pressure in the anterior chamber, the space between cornea and iris, filled with liquid called aqueous humour. Tonometry is the method by which one measures the IOP with a tonometer. The IOP is maintained by the aqueous humour secreted from the ciliary body to the posterior and anterior chambers and flows out from the Schlemm's canal as shown in Fig. 2.1. If the exit flow rate is decreased, the IOP becomes higher and the optic nerve or retina can be damaged by the excessive pressure, which is called glaucoma. Therefore, if the IOP is too high, it should be decreased by medicine or other means as soon as possible because the damage is irrecoverable, so accurate measurement of the IOP is very important.

The effect of corneal curvature on IOP measurement is widely discussed, although a consensus about how much corneal curvature affects the IOP measurement has not yet been achieved. Therefore, in this Chapter, the effect of corneal curvature on the IOP measurement is studied with artificially changing corneal curvature by wearing soft contact lenses. It is assumed that wearing soft contact lenses changes only corneal curvature. In each subject, IOPs are measured with and without wearing contact lenses and the effect of changing

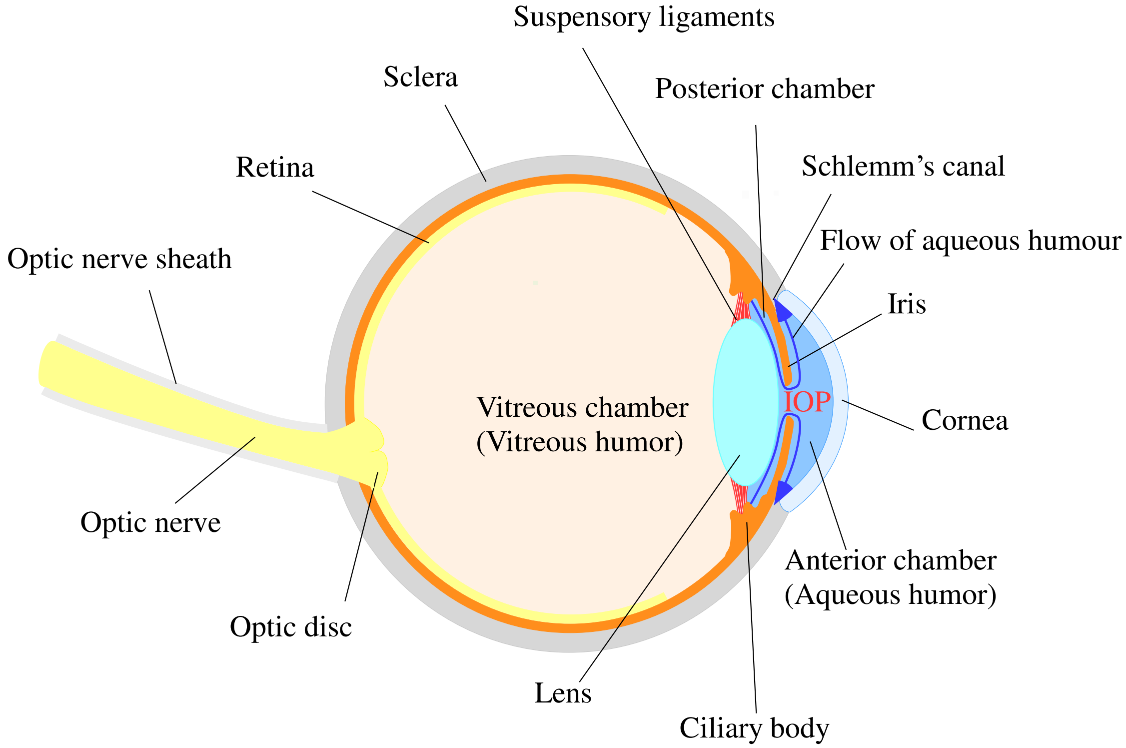

Figure 2.1: The cross section of human eyeball

corneal curvature by wearing soft contact lenses is measured. The experimental data are analyzed by an algorithm of constrained least-squares best fit. The effects of corneal curvature on the IOP measurement are discussed. All experiments with human subjects are conducted in Hiroshima and Osaka University in Japan.

The related works are summarized in Section 2.2 and the mechanism of air-puff tonometry and soft contact lenses are explained in Section 2.3.1 and Section 2.3.2. The expected effect of wearing contact lenses on the air-puff tonometry is then proposed based on the mechanism. By following that, the experimental results with human subjects are analyzed in Section 2.4 by the least-squares best fit proposed in Section 2.3.3. The results are discussed in Section 2.6.

2.2 Literature review

The influence of soft contact lens on the IOP measurement by air-puff tonometer was studied in [7, 8, 9, 10, 11, 12, 13]. In general, measuring IOP while wearing myopia lens underestimates the IOP, while with hyperopia lens, the IOP is often overestimated. The magnitude of error is proportional to the lens power D (Diopter). However, the magnitude of error and the conclusion as to whether the influence of soft contact lens is significant or insignificant are inconsistent. The effects of therapeutic contact lenses on IOP measurement by air-puff tonometer is studied in [14, 15, 16] and report that therapeutic contact lenses do not significantly affect the IOP measurement.

The influence of biomechanical properties of cornea on the IOP measured by GAT is studied by [17, 18, 19, 20, 21]. Kohlhass *et al.* [20] and Feltgen *et al.* [21] measured true IOP by direct intracameral manometry, with a needle inserted into the anterior chamber, and compared the results with the IOP measured by GAT with the cooperation of patients who were scheduled for intraocular surgery. Kohlhass *et al.* [20] calibrated IOP by adding adjustable saline and closed the cannula, and then measured IOP by GAT. They reported that the IOP measured by GAT is significantly affected by central cornea thickness (CCT), about $1mmHg/25\mu m$, but not significantly affected by corneal curvature. However, Feltgen *et al.* [21] reported that the IOP measured by GAT is not significantly affected by CCT. They measured IOP by GAT first, then measured the true IOP before surgery. The influence of CCT and corneal curvature on the IOP measured by non-contact tonometer (NCT) is studied in [22, 23] which reported that NCT also has similar results to GAT. In general, the IOP measured by applanation tonometer is proportional to CCT and corneal curvature and the influence of CCT is more significant than corneal curvature. However, the magnitudes of the effect of CCT and corneal curvature are different depending on the literature.

Kaneko *et al.* recorded the deformation of the cornea by high speed camera, using an air-puff tonometer [2, 3]. They proposed a dynamic model of human eye and experimentally estimated the stiffness and damping of the cornea and eyeball [24].

2.3 Theoretical Background

2.3.1 The working principle of air-puff tonometry

All experiments with human subjects are conducted in Prof. Kaneko's lab in Hiroshima and Osaka University in Japan. This study was approved by the Institutional Review Board of Hiroshima University, Japan. All study procedures adhered to the tenets of the Declaration of Helsinki. Written informed consent was obtained from each subject after informing them of the nature and possible complications of the examination procedures.

An air-puff tonometer works by sending an air puff from the air nozzle to flatten the center of the cornea as shown in Fig. 2.2(b). The applanation is detected by an infrared light emitter and detector pair. The direction of the reflected infrared light varies while the center of the cornea deforms as shown in Fig. 2.2(a-c). In the beginning of the examination, the position of the infrared emitter and detector pair is adjusted to the infrared light will be reflected from the surface of the cornea to the detector. However, this is only successful if the center of the cornea is deformed by a specific amount. Fig. 2.2(b) shows that maximum light is reflected onto the detector when the center of the cornea is flattened. Fig. 2.2(a) shows that the reflected light is dispersed when the center of the cornea is not deformed at all. Fig. 2.2(c) shows that the reflected light also moves away from the detector when the cornea becomes concave. Fig. 2.3 shows the output signals of the infrared light detector shown in Fig. 2.2. The output signal has a peak when the cornea is flattened, as shown in Fig. 2.2(b). The signals have two peaks with the cornea being flattened twice. The second peak is in the recovery phase after the maximum deformation. The IOP of the air-puff tonometer is estimated based on the time to the first peak of the applanation signals. Fig. 2.4 shows the correlation between the first peak time and IOP. Ogbuehi [25] reported that there is no statistically significant difference between IOP measured by the Goldmann applanation tonometer (GAT) and the air-puff tonometer.

Fig. 2.5 shows a series of photos during the IOP measurement by an air-puff tonome-

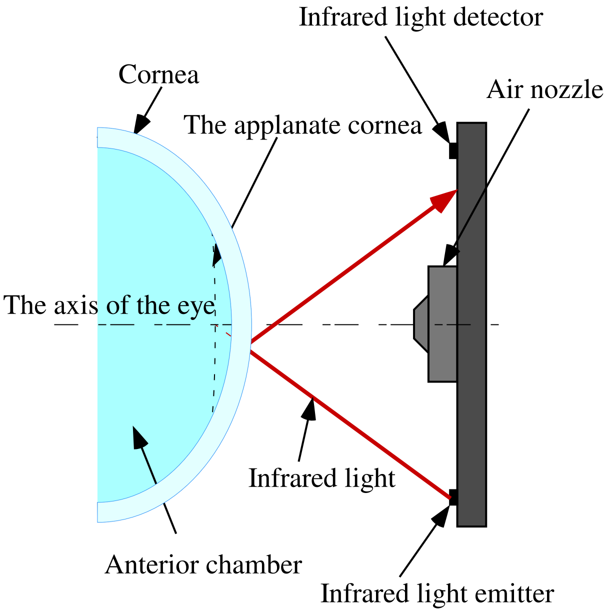

(a) Original state

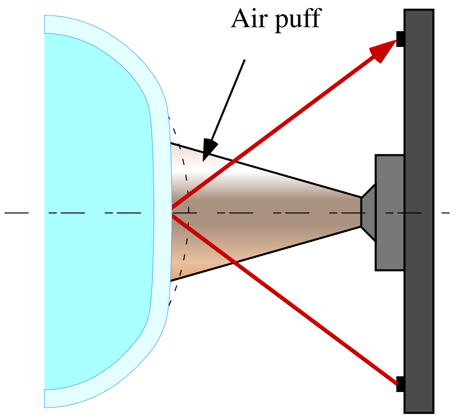

(b) Applanation

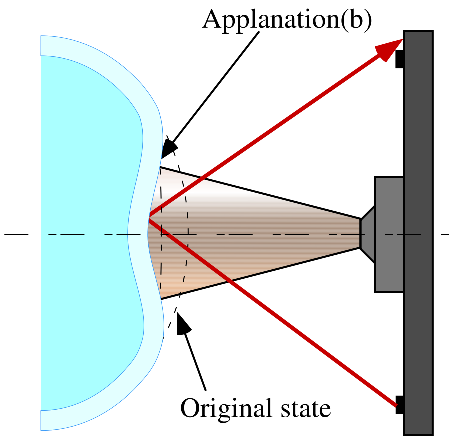

(c) Maximum deformation

Figure 2.2: The deformation process of the cornea when air-puff is applied

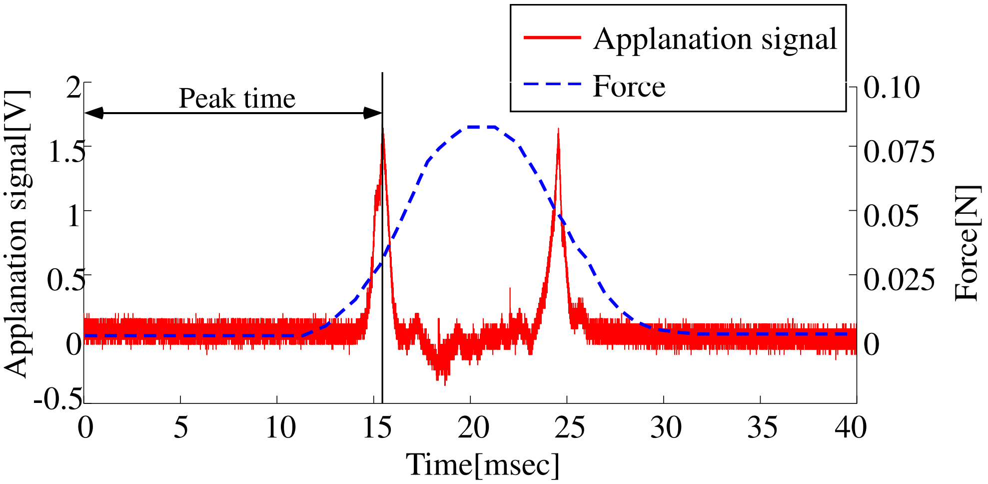

Figure 2.3: The applanation signal (Provided by Prof. Kaneko)

ter. Fig. 2.5(a) is the original shape of the human eye. Fig. 2.5(b) shows the shape of the eye when the applanation signal has the first peak corresponding to Fig. 2.2(b). In Fig. 2.5(d), the actual shape of the central cornea is concave as shown in 2.2(c). However, the photos are taken from the side so the central cornea looks flat.

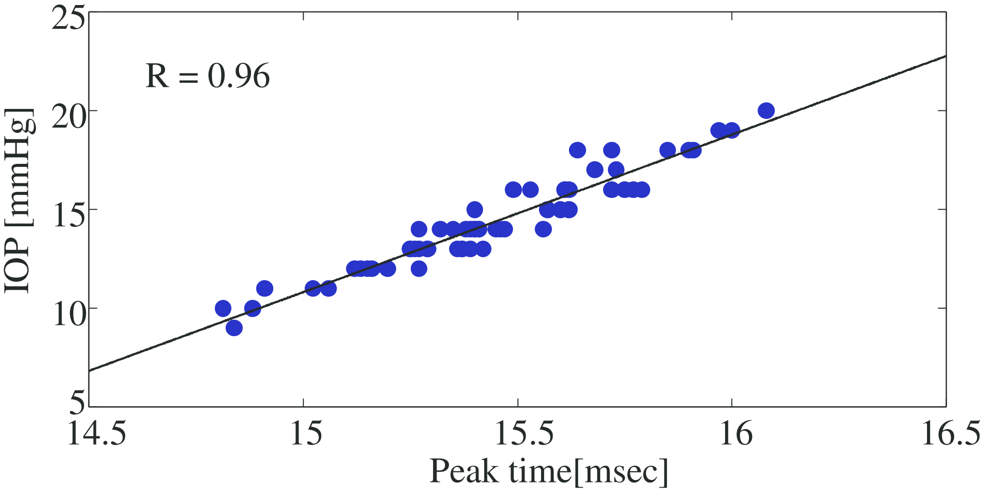

Figure 2.4: The relationship between IOP and the peak time (Provided by Prof. Kaneko)

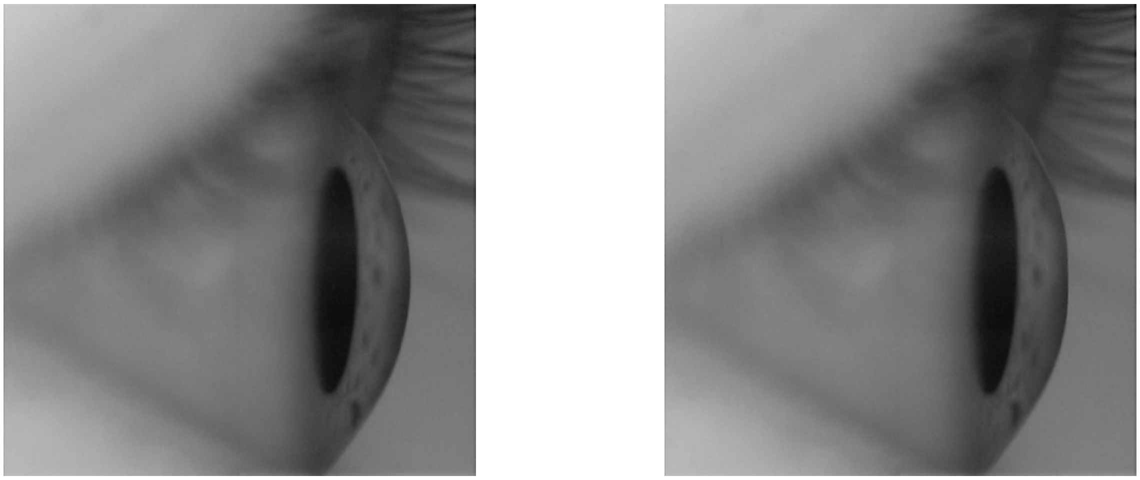

(a) $t = 0$[msec] (c) $t = 15.6$[msec]

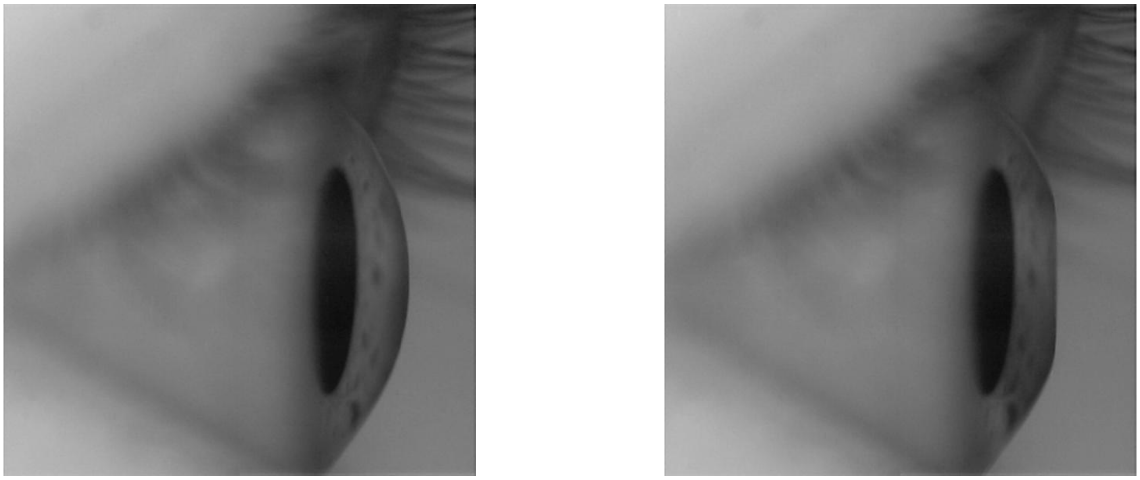

(b) $t = 15$[msec] (d) $t = 20$[msec]

Figure 2.5: A series of photos during IOP measurement by an air-puff tonometer (Provided by Prof. Kaneko)

2.3.2 The expected effects of contact lens on air-puff tonometry

Contact lenses are devices which artificially change corneal curvature to correct the refraction errors, such as myopia (nearsightedness) and hyperopia (farsightedness). A contact lens has two surfaces whose radius of curvature are R_1 and R_0 as shown in Fig. 2.6. The front surface with the radius of curvature R_1 is close to light source and the back surface with the radius of curvature R_0 makes contact with the cornea. Therefore, R_0 is designed to match with the radius of cornea, R; R_1 is designed to adjust the refractive rate. For instance, contact lenses for myopia have smaller curvature, as shown in Fig. 2.6(b); while contact lenses for hyperopia have larger curvature, as shown in Fig. 2.6(c). Equation (2.1) shows the lensmaker's equation where D (Diopter) is the power of the lens, f is the focal length, n is the refractive index, d is the thickness of the lens, and R_1 and R_0 are shown in Fig. 2.6 (a). The units of f, R_1, R_0, d are meters.

$$D = \frac{1}{f} = (n-1)\left[\frac{1}{R_1} - \frac{1}{R_0} + \frac{(n-1)d}{nR_1R_0}\right] \tag{2.1}$$

By assuming that $d \ll R_1, R_0$, equation (2.1) becomes

$$D = (n-1)\left[\frac{1}{R_1} - \frac{1}{R_0}\right] \tag{2.2}$$

The diopter D becomes negative for the myopia lens and positive for the hyperopia lens. By solving the equation (2.1) for R_1, the radius of the front-side surface R_1 is

$$R_1 = \frac{1}{\frac{D}{n-1} + \frac{1}{R_0}} \tag{2.3}$$

The correction of curvature by contact lens changes the necessary displacement to flatten the specific circle area of the cornea, and the change of the distance affects the IOP measurement by air-puff tonometry. The relationship between the necessary deformation of the center of the cornea into the direction of the axis of eye, d, and the radius of cornea R is shown in equation (2.4) and Fig. 2.7, where α is the radius of the flattened area when the output signal from the infrared light detector has the first peak.

$$d_{NCL} = R - \sqrt{R^2 - \alpha^2} \tag{2.4}$$

R_0: The radius of the lens surface making contact with cornea

R_1: The radius of the lens surface close to the light source

R_{1_m}: The radius of the myopia lens surface close to the light source

R_{1_h}: The radius of the hyperopia lens surface close to the light source

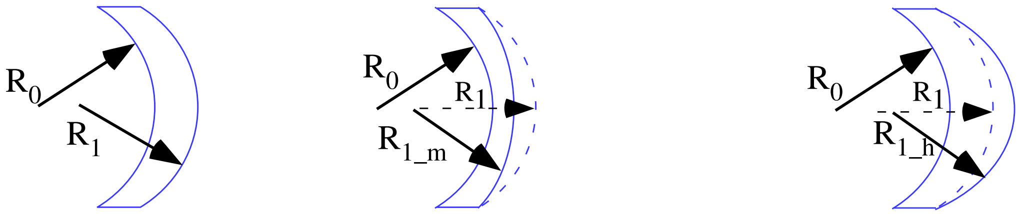

$R_1 = R_0$

(a) Contact lens
of equal curvature

$R_{1\_m} > R_0$
Decrease the refraction

(b) Contact lens
for myopia

$R_{1\_h} < R_0$
Increase the refraction

(c) Contact lens
for hyperopia

Figure 2.6: Contact lens for myopia and hyperopia

When wearing contact lenses, the necessary deformation d_{CL} becomes

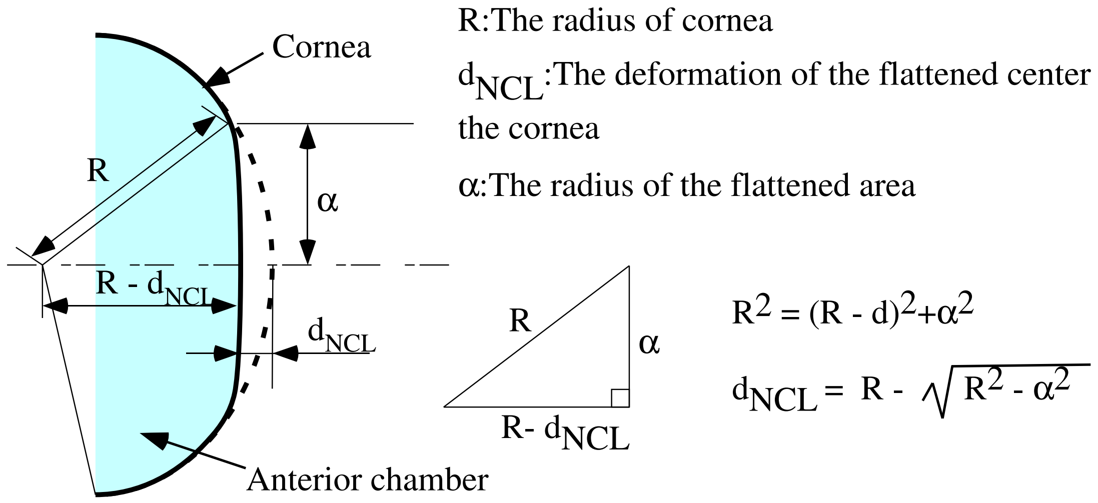

Figure 2.7: Illustration of the eyeball when the center of the cornea is flattened

$$d_{CL} = R_1 - \sqrt{{R_1}^2 - \alpha^2} \tag{2.5}$$

It is assumed that the infrared is reflected on the front surface of the contact lens, not on the surface of the cornea. The change of the necessary deformation by wearing contact lenses Δd is

$$\Delta d = d_{CL} - d_{NCL} \tag{2.6}$$

By substituting equations (2.3), (2.4), and (2.5) into (2.6), we obtain

$$\Delta d = \frac{1}{\frac{D}{n-1} + \frac{1}{R}} - \sqrt{\left(\frac{1}{\frac{D}{n-1} + \frac{1}{R}}\right)^2 - \alpha^2} - \left[R - \sqrt{R^2 - \alpha^2}\right] \tag{2.7}$$

Fig. 2.8 illustrates the Δd in myopia lens, Δ_m, and in hyperopia lens, Δ_h. Fig. 2.9 shows the relationship between Δd in percentage and D (Diopter). Three lines are plotted in the figure with three values of the radius of curvature of cornea, 7.4mm, 7.8mm, and 8.2mm; the refractive index of the lens n is assumed to be 1.4. The figure shows that Δd is proportional to D.

Fig. 2.10 shows how to convert the Δd to ΔIOP. Fig. 2.10 (a) shows the conversion from the peak time to IOP and Fig. 2.10 (b) shows the experimental data of the displacement

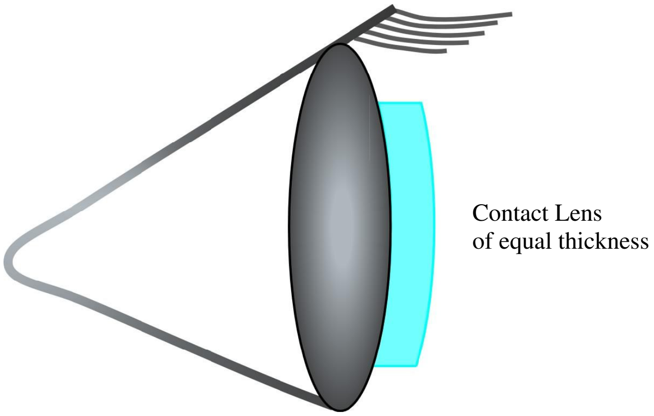

(a) Equal thickness

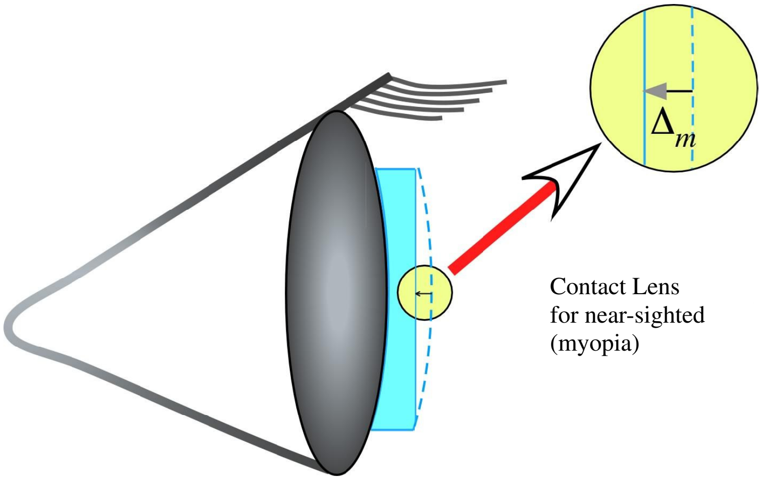

(b) For myopia

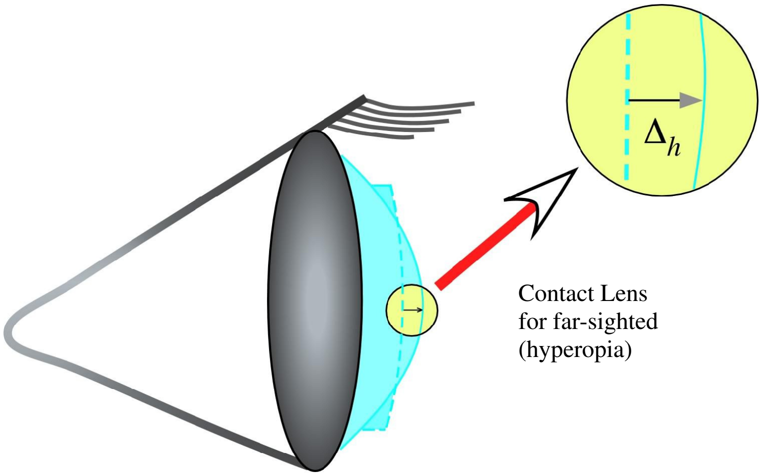

(c) For hyperopia

Figure 2.8: Example of Δd

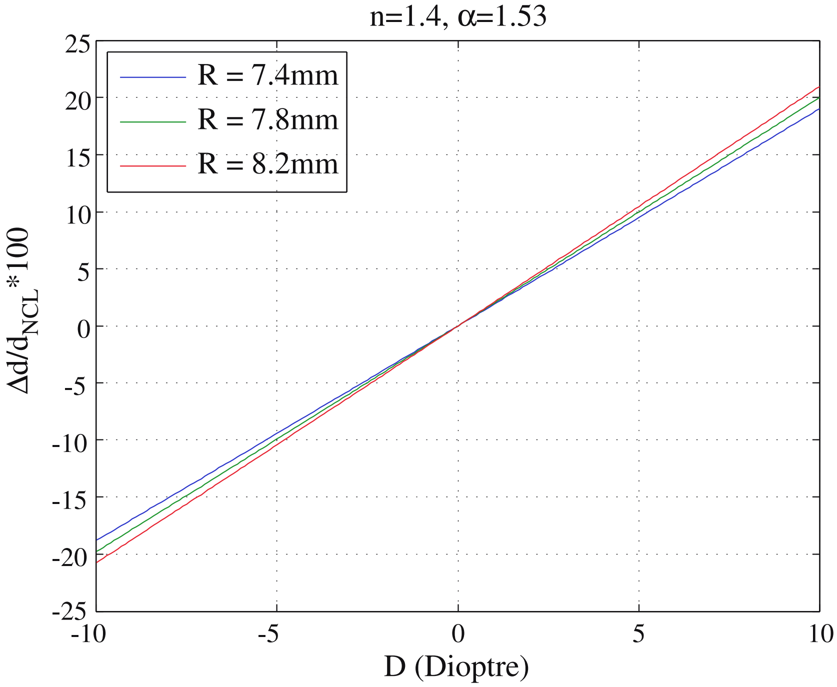

Figure 2.9: The relationship between the power of lens and the change of the displacement to the applanation.

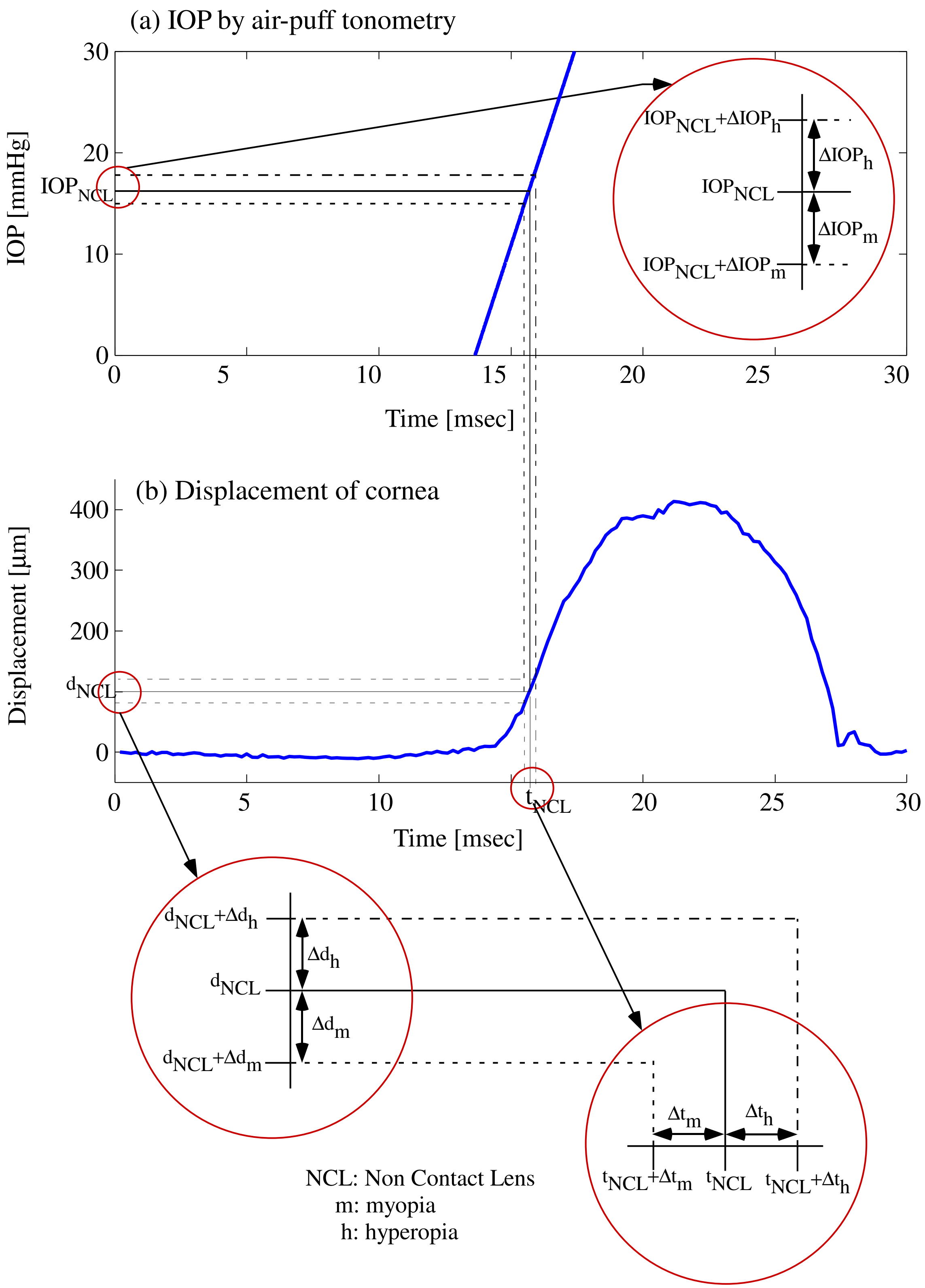

Figure 2.10: The relationship between Δd and ΔIOP. (Original date is provided by Prof. Kaneko)

of cornea. A contact lens changes the displacement when the applanation signal has peak, d_{NCL}. The hyperopia lens increases Δd_h and the myopia lens decreases Δd_m as shown in the vertical axis in Fig. 2.10(b). Then, when applanation signal has its first peak, delay Δt_h for a hyperopia lens and advance Δt_m for a myopia lens as shown in the horizontal axis in Fig. 2.10(b) will be expected. Therefore, the measured IOP will increase ΔIOP_h for hyperopia lens and decrease ΔIOP_m for myopia lens as shown in Fig. 2.10(a). In Fig. 2.10, d_{NCL}, Δt_{NCL}, and IOP_{NCL} are the values without contact lens. The ΔIOP can be estimated by

$$\Delta IOP \propto \frac{\Delta d}{\bar{v}} \tag{2.8}$$

where $\bar{v}$ is the average velocity of the deformation between t_{NCL} and $t_{NCL} + \Delta t$. The Δd is proportional to the power of lens D as shown in Fig. 2.9, so ΔIOP is proportional to the power of lens D. If we can assume that the $\bar{v}$ is constant, ΔIOP is only a function of the power of lens. Therefore, ΔIOP for each D can be experimentally obtained by the LS best fit with the constraint of slope as 1.

2.3.3 Derivation of the LS best fit as an optimization problem

The least-squares (LS) best fit is a common method for analyzing experimental data [26]. We derive a LS best fit algorithm by approaching it as an optimization problem. The linear equation (2.9) with n set of experimental data points of (x_i, y_i) can be arranged in the following matrix equation (2.10).

$$y = mx + \beta \tag{2.9}$$

$$\mathbf{Az} = \mathbf{b} \Longrightarrow \begin{bmatrix} x_1 & 1 \\ x_2 & 1 \\ \vdots & \vdots \\ x_n & 1 \end{bmatrix} \begin{bmatrix} m \\ \beta \end{bmatrix} = \begin{bmatrix} y_1 \\ y_2 \\ \vdots \\ y_n \end{bmatrix} \tag{2.10}$$

where $z = [m \;\; \beta]^T$ contains the slope and the intercept of the LS best fit, while constraining the slope of the linear fitting line to 1, can be formulated as follows:

$$\text{minimize:} \quad \frac{1}{2}||(\mathbf{Az} - \mathbf{b})||^2 \tag{2.11}$$

$$\text{subject to:} \quad \mathbf{Cz} = \mathbf{d} \tag{2.12}$$

where $C = [1 \;\; 0]$ and $d = 1$. The quadratic term of the objective function in equation (2.11) is prefixed with a factor $\frac{1}{2}$ for convenience in differentiation. The constraint equation $\mathbf{Cz} = \mathbf{d}$ requires that the slope is 1; *i.e.* $m = 1$.

The Lagrangian of this optimization problem is

$$\begin{aligned} \mathscr{L}(z, \lambda) &= \frac{1}{2}||\mathbf{Az} - \mathbf{b}||^2 + \lambda^T(\mathbf{Cz} - \mathbf{d}) \\ &= \frac{1}{2}\mathbf{z}^T\mathbf{A}^T\mathbf{Az} - \mathbf{b}^T\mathbf{Az} + \frac{1}{2}\mathbf{b}^T\mathbf{b} + \lambda^T\mathbf{Cz} - \lambda^T\mathbf{d} \end{aligned} \tag{2.13}$$

The optimality condition requires the following derivatives to be zero

$$\begin{aligned} \nabla_z \mathscr{L} &= \mathbf{A}^T\mathbf{Az} - \mathbf{A}^T\mathbf{b} + \mathbf{C}^T\lambda = 0 \\ \nabla_\lambda \mathscr{L} &= \mathbf{Cz} - \mathbf{d} = 0 \end{aligned}$$

The above equations can be put in a block matrix form as

$$\begin{bmatrix} \mathbf{A}^T\mathbf{A} & \mathbf{C}^T \\ \mathbf{C} & 0 \end{bmatrix} \begin{bmatrix} \mathbf{z} \\ \lambda \end{bmatrix} = \begin{bmatrix} \mathbf{A}^T\mathbf{b} \\ \mathbf{d} \end{bmatrix} \tag{2.14}$$

If the block diagonal matrix in equation (2.14) is invertible[1] , the solution can be obtained as

$$\begin{bmatrix} \mathbf{z} \\ \lambda \end{bmatrix} = \begin{bmatrix} \mathbf{A}^T\mathbf{A} & \mathbf{C}^T \\ \mathbf{C} & 0 \end{bmatrix}^{-1} \begin{bmatrix} \mathbf{A}^T\mathbf{b} \\ \mathbf{d} \end{bmatrix} \tag{2.15}$$

The vector **z** contains the parameters of the linear regression (a line) that satisfies the constraint equation.

---

[1] The block matrix composed of experimental data (x_i, y_i) is typically invertible, with more than 3 independent data points.

2.4 Experiments

2.4.1 Experimental Method

The air-puff tonometer CT-90A manufactured by TOPCON CORPORATION was used to measure IOP with and without contact lenses for each subject. For the contact lens, the ACUVUE 2 manufactured by Johnson & Johnson was used. Three types of contact lenses, -5 D, -0.5 D, and -5 D, were used in the experiment. The central thicknesses of the contact lenses are 84 μm, 124 μm, and 210 μm respectively. The subjects are 11 male adults and 16 female adults (the average age is 24 years old).

2.4.2 Experimental Results and Analysis

The LS best fit algorithm is implemented by MATLAB and experimental data are shown in Fig. 2.11, 2.12, and 2.13. Table 2.1 summarizes the results. Fig. 2.14 plots the data in Table 2.1 and finds the relationship between the power of lens D and ΔIOP. ΔIOP is defined as

$$\Delta IOP = IOP_{NCL} - IOP_{CL} \tag{2.16}$$

where IOP_{NCL} is the IOP readings without contact lenses and IOP_{CL} is the IOP readings with contact lenses.

Curvature of lens	$+5$ (hyperopia)	-0.5 (myopia)	-5 (myopia)
Δ_{IOP}	$-1.396\,mmHg$	$0.2889\,mmHg$	$1.1423\,mmHg$
R_1	$7.107\,mm$	$7.877\,mm$	$8.642\,mm$

Table 2.1: Summary of the results of LS best fit of IOP for non-contact tonometry (NCT). R_1 is calculated by equation (2.3) by assuming $R_2 = 7.8mm$ and $n = 1.4$

.

The results show that hyperopia lenses overestimate IOP and myopia lenses underestimate IOP. Furthermore, the magnitude of ΔIOP is inversely proportional to the power of lens D. In addition, the weak lenses, -0.5 D, similar to therapeutic contact lenses do not

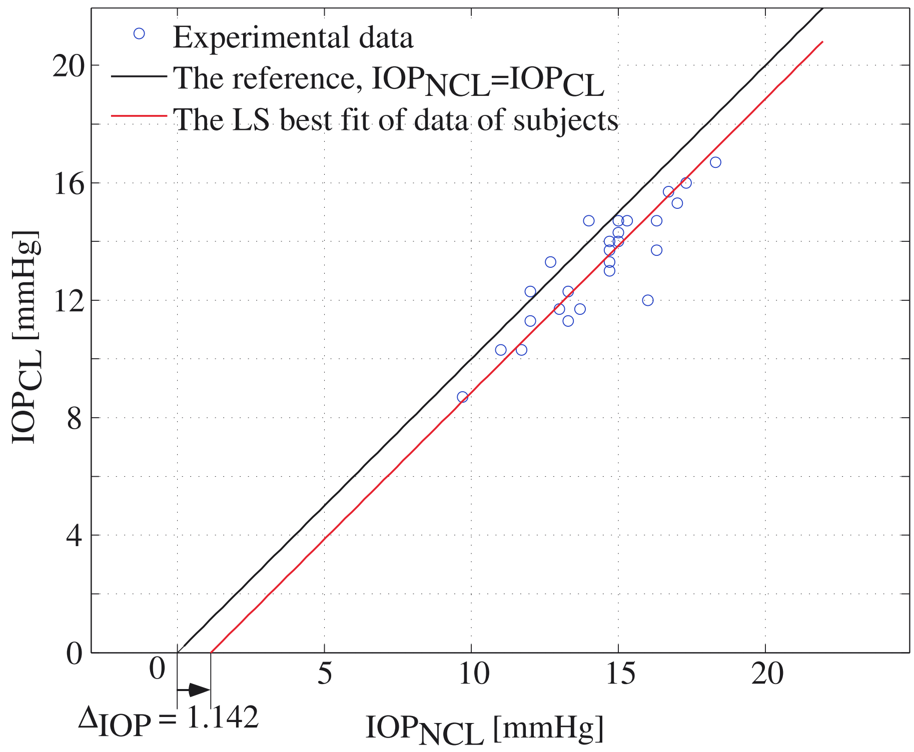

Figure 2.11: With −5 D contact lens

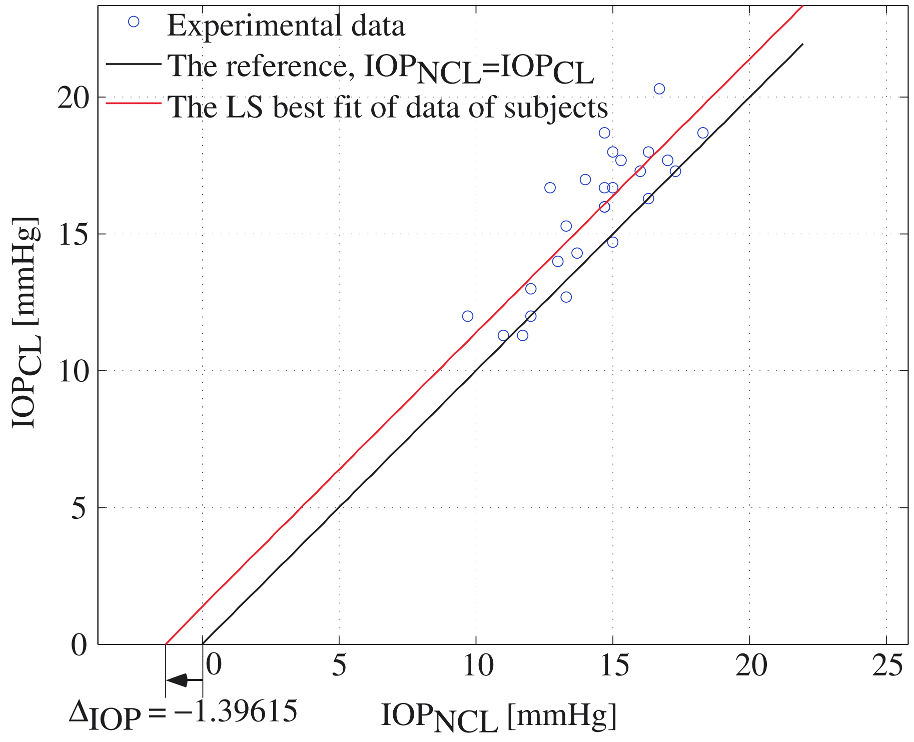

Figure 2.12: With +5 D contact lens

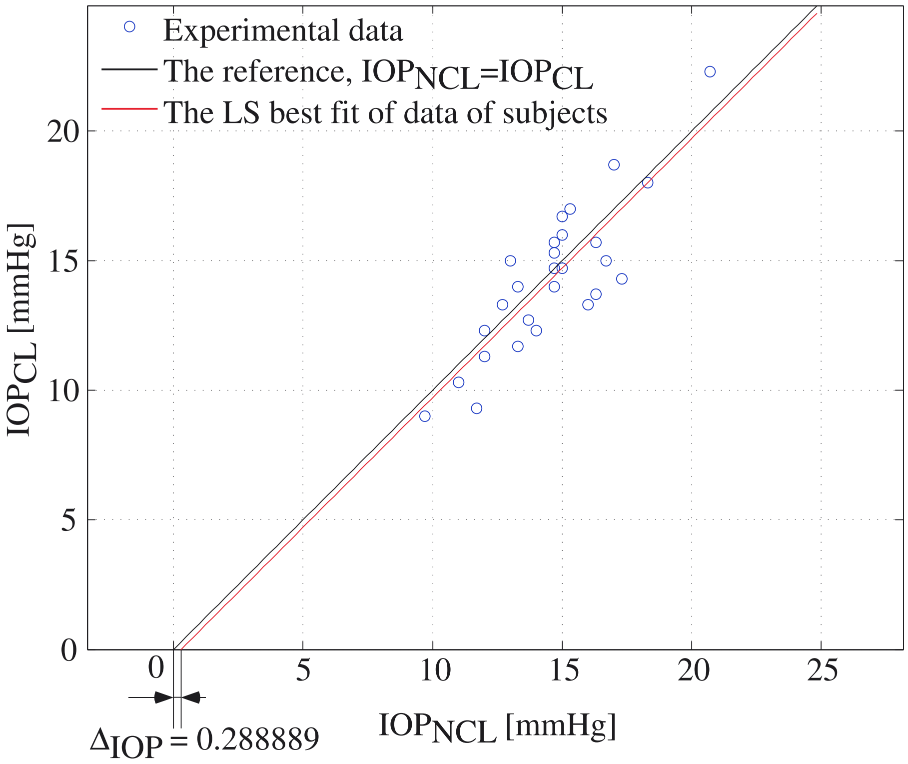

Figure 2.13: With −0.5 D contact lens

affect the IOP measurement significantly.

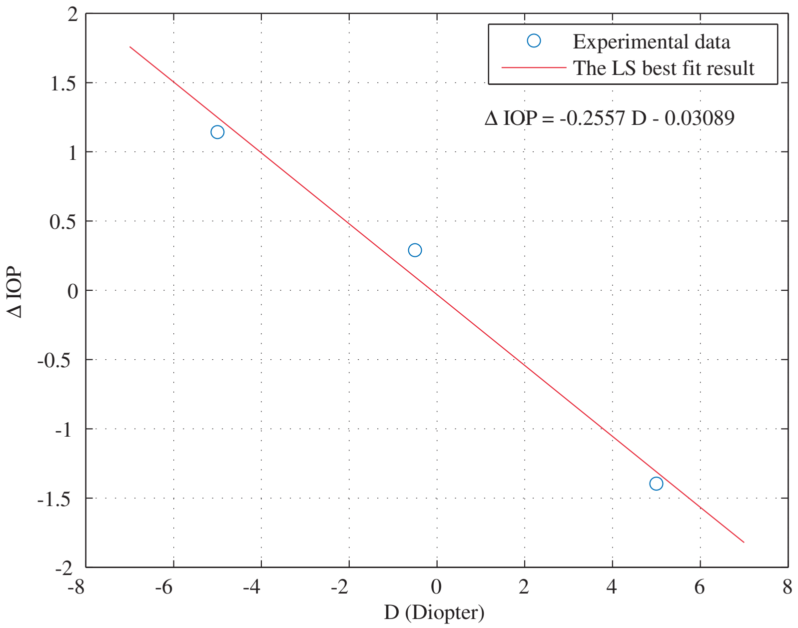

Figure 2.14: The relationship between the power of lens D and ΔIOP

2.5 Conclusion

- In air-puff tonometry, the IOP measured when wearing hyperopia contact lenses is overestimated and the IOP measured when wearing myopia contact lenses is underestimated.
- The measurement error of IOP, ΔIOP, is inversely proportional to the Diopter, D.
- The stiffness change due to wearing contact lens is negligible.
- The radius of corneal curvature will affect the IOP measured by air-puff tonometry. When the radius of corneal curvature is artificially changed from 7.107mm to 8.642mm by wearing contact lenses, the measurement error of IOP, ΔIOP, is within $\pm 1.5 mmHg$. The range of the radius of cornea is $7.07 \sim 8.32 mm$ [20], so the effect of the radius of cornea on the IOP measurement by air-puff tonometry is within $\pm 1.5 mmHg$.

2.6 Discussion

Intuitively and from literature, wearing contact lenses increases the central corneal thickness (CCT) and the stiffness of the cornea and overestimate the IOP measurement, but the results in Fig. 2.14 show that when CCT and the stiffness are increased while corneal curvature is kept in the same, $D = 0$, the IOP measurement is not affected, $\Delta IOP = 0$. These results are not intuitive. In the experiments, 2 week disposable soft contact lenses were used. Generally, a disposable lens is thinner and softer than a regular lens because thinner and softer lenses improve user experience. This can be the reason why only corneal curvature is affected by wearing contact lenses in this experiment. It is possible that different types of contact lenses have higher stiffnesses and affect the IOP measurement. Thus, more experiments with different type of contact lens will help further understanding.

Usually, IOP is measured to find excessive IOP which is a symptom of glaucoma. Thus, underestimating IOP is very dangerous but overestimating is not detrimental to glaucoma detection. Therefore, users of strong myopia lenses should be careful. In routine eye examinations for contact lens users, if the data for users' contact lens is available, the data can be used to calibrate ΔIOP without removing contact lenses. Although the data are not available, ΔIOP can be estimated by measuring IOP with and without contact lens in the first few examinations. Then, the same ΔIOP can be used as long as the user is wearing same contact lenses.

Chapter 3

IOP Measurement Using Air-Puff Tonometry: *Dynamic Modeling of Human Eyeball with Experimental Results*

3.1 INTRODUCTION

In Chapter 2, the effect of the corneal curvature on IOP measurement is studied with artificially changing the corneal curvature by wearing soft contact lenses. However, other parameters, which may affect the IOP measurement, cannot be artificially changed in a subject. For instance, the viscosity of the anterior chamber or the stiffness between the eyeball and the eye socket cannot be artificially changed. On the other hand, mechanical modeling can afford us to change any one of a specific parameter at a time while keeping other parameters the same. Thus, we can observe the effect of any interested parameter from the simulation results through the model. Therefore, in this Chapter, human eyeballs are modeled with discrete spring-mass-damper system and the effect of each parameter on the IOP measurement is studied.

The modeling of the eyeball based on experimental results is studied by Kaneko and Kurita *et al.*. Kurita *et al.* studied the contact stiffness of the eyes which is defined by an applied force versus the displacement along the direction of the applied force in GAT. The stiffness was constant while increasing the displacement in an examination and was linear with respect to IOP [27]. Kaneko *et al.* recorded the deformation of the cornea during the

IOP measurement by air-puff tonometry by a high speed camera [2, 3]. They proposed a dynamic model of the eye and experimentally estimated the stiffness and damping of the eye using the experimental results [24].

3.2 Modeling as a 1-DOF system

In this section, we model the human eyeball as a 1 degree of freedom, DOF, system with mass, damper, and spring, then obtain the responses to an external force by the linear system theory with different parameters. Fig. 3.1(a) illustrates the cross section of the eyeball and Fig. 3.1(b) shows the 1-DOF system model. In air-puff tonometry, the external force by an air puff $F(t)$ is applied along the direction of the axis of the eyeball such that the displacement of the cornea $y(t)$ is defined along the same direction. The mass represents the mass of the cornea; the damper and spring are determined by the applied force and the displacement of the cornea. In this section, we assume that only the cornea is deformed by the applied force. The deformation and displacement of other parts are discussed in the next section.

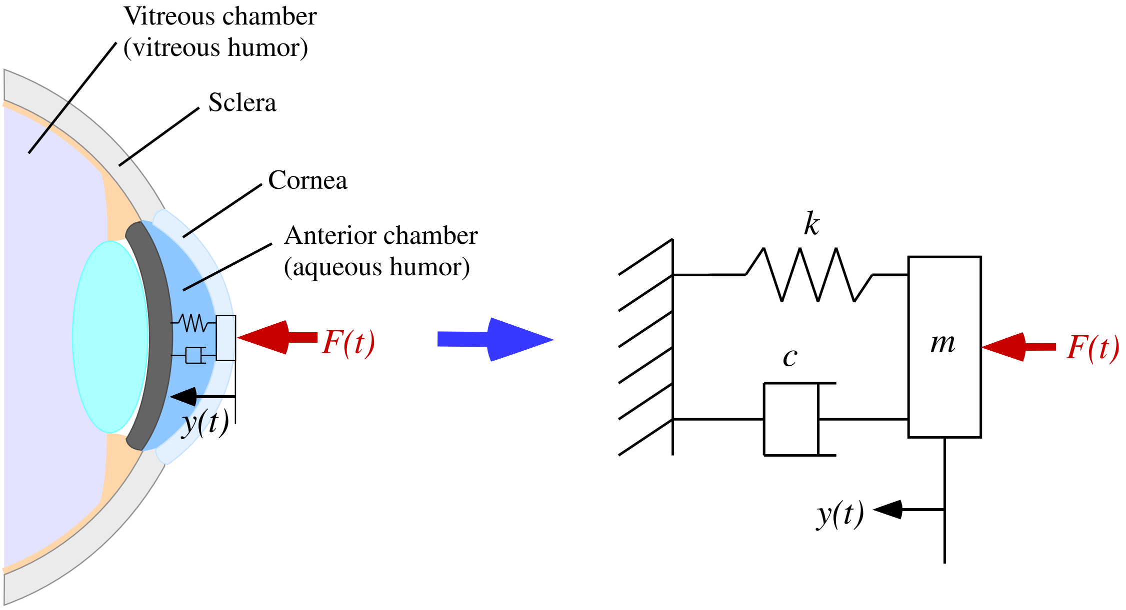

(a) Human eye ball (b) Mass, damper, and spring model

Figure 3.1: Dynamic modeling of a human eyeball

The equation of motion of the model is shown in the following equation

$$m\ddot{y}(t) + c\dot{y}(t) + ky(t) = F(t) \tag{3.1}$$

Eq. (3.1) can be normalized as follows

$$\ddot{y}(t) + 2\zeta\omega_n\dot{y}(t) + \omega_n^2 y(t) = f(t) \tag{3.2}$$

where ζ is damping ratio, ω_n is natural frequency, and $f(t) = F(t)/m$. The response to a general excitation can be obtained by the linear system theory [28]

$$\mathbf{x}(t) = \Phi(t)\mathbf{x}(0) + \int_0^t \Phi(\tau)\mathbf{B}F(t-\tau)d\tau \tag{3.3}$$

where $\mathbf{x}(t) = \begin{bmatrix} y(t) & \dot{y}(t) \end{bmatrix}^T$ is the state vector, $\mathbf{B} = \begin{bmatrix} 0 & 1/m \end{bmatrix}^T$, $\Phi(t)$ is the state transition matrix, and $\mathbf{x}(0) = \begin{bmatrix} y(0) & \dot{y}(0) \end{bmatrix}^T$ is the initial condition. The state transition matrix $\Phi(t)$ is expressed in equation (3.4)

$$\Phi(t) = \frac{1}{\omega_d}e^{-\zeta\omega_n t}\begin{bmatrix} \omega_d\cos\omega_d t + \zeta\omega_n\sin\omega_d t & \sin\omega_d t \\ -\omega_n^2\sin\omega_d t & \omega_d\cos\omega_d t - \zeta\omega_n\sin\omega_d t \end{bmatrix} \tag{3.4}$$

where $\omega_d = \omega_n\sqrt{1-\zeta^2}$. From Eq. (3.3), Eq. (3.4), and assuming $\mathbf{x}(0) = 0$, the displacement $y(t)$ is obtained in the following

$$y(t) = \frac{1}{m\omega_d}\int_0^t e^{-\zeta\omega_n\tau}\sin\omega_d\tau F(t-\tau)d\tau \tag{3.5}$$

The external force $F(t)$ is modeled based on the experimental results by Kaneko *et al.* [2] as shown in Fig. 3.2(a). The shape of the applied force resembles the bell-shaped curve so it can be modeled by the equation based on normal distribution

$$F(t) = Ae^{\frac{-(t-\mu)^2}{2\times\sigma^2}} \tag{3.6}$$

By adjusting the coefficients in Eq. (3.6), the external force $F(t)$ can be calibrated by the following parameters

$$F(t) = 0.08e^{\frac{-(t-0.018)^2}{2\times 0.003^2}} \tag{3.7}$$

as shown in Fig. 3.2(b). First, the magnitude and the peak time of $F(t)$ are set by the parameters A and μ, respectively. After that, the shape of $F(t)$ is fitted by adjusting the parameter σ.

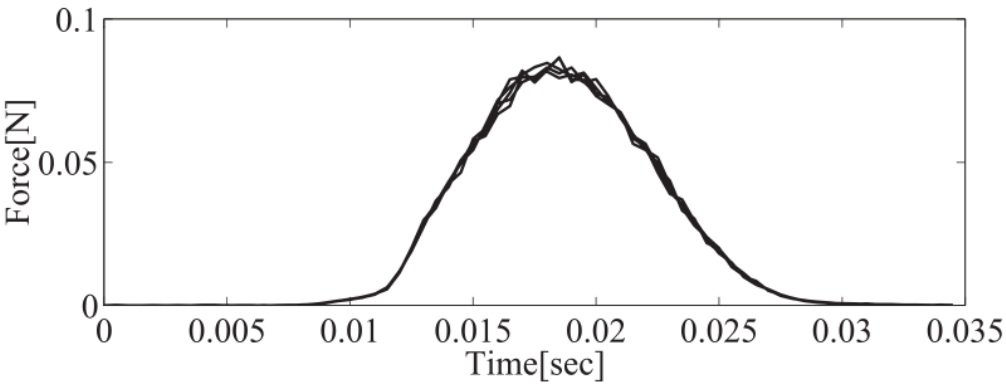

(a) Experimental results from Fig. 7 in [2]

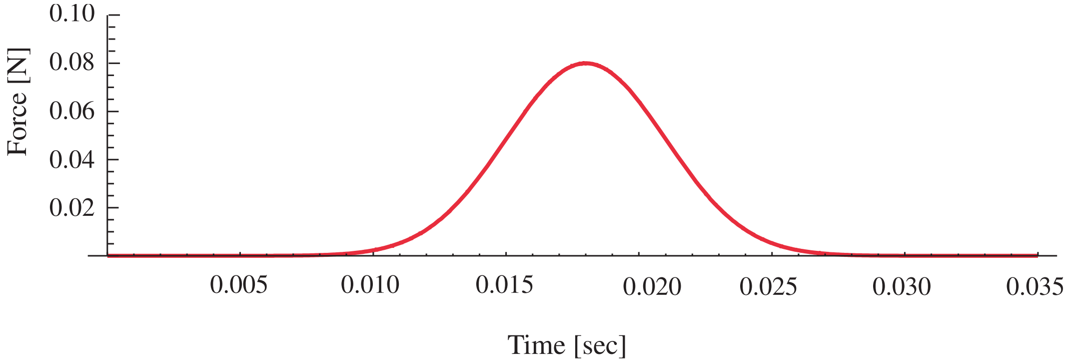

(b) $F(t) = 0.08e^{-\frac{(t-0.018)^2}{2\times 0.003^2}}$

Figure 3.2: External force applied by air-puff.

The parameters, m, c, and k, in the model are estimated by experimental results and human anatomy. The mass of the cornea, m, is estimated to be 15 mg based on the volume of the cornea and the typical density of human cell, the weight of a soft contact lens is also similar to this value. The viscous damping coefficient c is assumed to be 0.05 Ns/m based on [24]. The stiffness k is estimated by the Goldmann applanation tonometry (GAT) principle. Kaneko *et al.* measured the contact stiffness k_{nct} in the IOP measurement by GAT and found that the displacement was linear with respect to the applied force [27]. Thus, the stiffness is assumed to be constant. Fig. 3.3 shows the principle of GAT. In the IOP measurement by GAT, an ophthalmologist will apply a force along the direction of the eye axis by a probe which flattens the cornea. The applied force is gradually increased until the radius of the flattened area, α, reaches 1.53 mm. The probe has a pressure sensor which measures the IOP at $\alpha = 1.53$ mm. Typically, IOP is expressed in units of mmHg where 1 mmHg = 133 Pa. In general, normal IOP is between 10 to 20 mmHg. The displacement, D, in the direction of the applied force can be calculated by the Pythagorean theorem as shown in Fig. 3.3 where R is the radius of the cornea and α is the radius of the flattened area. From the displacement D and the applied force F, the stiffness k is obtained by Eq. (3.8) where

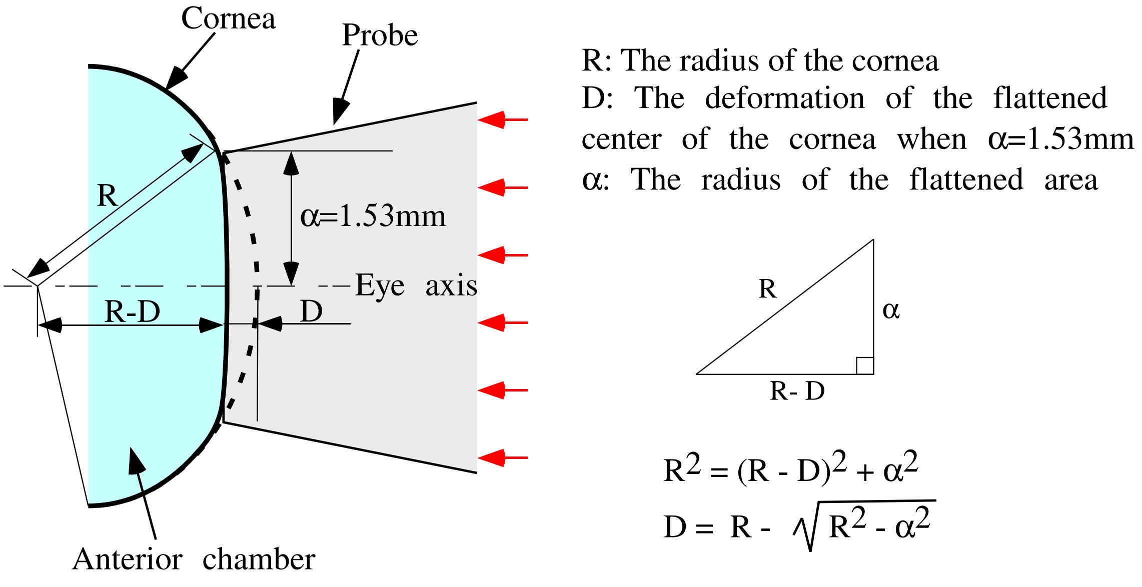

Figure 3.3: The operating principle of GAT

the unit of IOP is mmHg

$$k = \frac{F}{D} = \frac{\pi(1.53\times10^{-3})^2 \times 133\,IOP}{R-\sqrt{R^2-1.53^2}} \tag{3.8}$$

The typical value of the radius of the cornea R is 7.8mm. From Eq. (3.8) and setting $R = 7.8$ mm, the stiffness k corresponding to IOP =10, 13, and 17 mmHg are 65, 85, and 111 N/m, respectively.

The dynamic response $y(t)$ is obtained by calculating Eq. (3.5) numerically and shown in Fig. 3.4 with the quasi-static response $F(t)/k$ for comparison. The shape of the dynamic response $y(t)$ is almost similar to the quasi-static response with about 1 ms of delay. It is reported that there is a delay of $1 \sim 2$ ms between the rise time of the applied force and the displacement [2]. The proposed dynamic model and analysis represents well the dynamic properties of the eyeball. The IOP measured by air-puff tonometry is estimated from the time when the displacement $y(t)$ reaches a specific value for the first time. Therefore, the delay in the dynamic model is important.

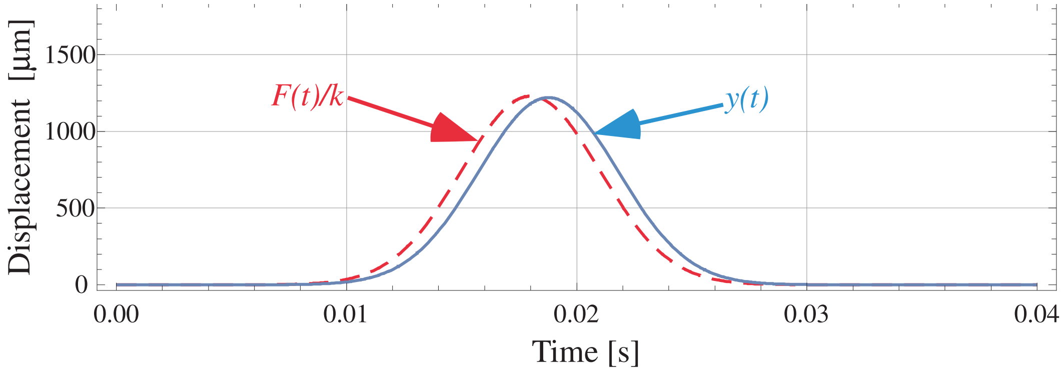

Figure 3.4: Static and dynamic responses

Fig. 3.5 shows the responses $y(t)$ with the different stiffness based on different IOP and Fig. 3.6 shows a part of the responses obtained from the experiments in [2]. Both results have the maximum displacement around time 18 ms. However, the magnitude of the maximum displacements $y(t)$ in Fig. 3.5 is $2 \sim 3$ times larger than those of the experimental results [2]. It is about 3 times larger at IOP=10 mmHg and 2 times larger at IOP=17 mmHg.

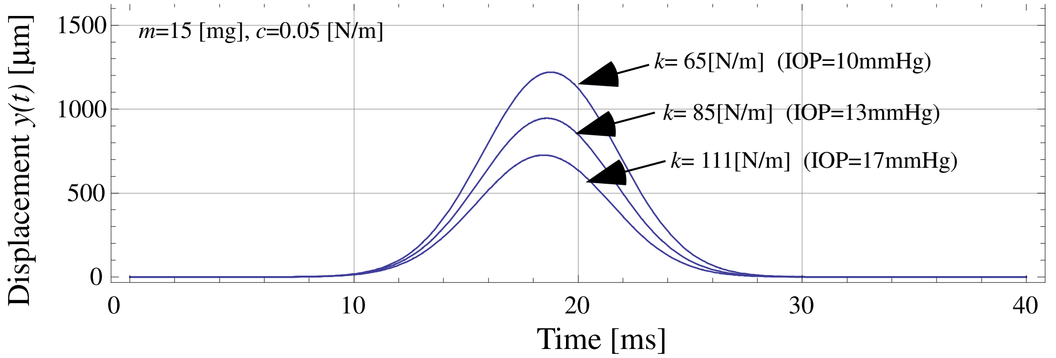

Figure 3.5: The responses $y(t)$ with different values of k

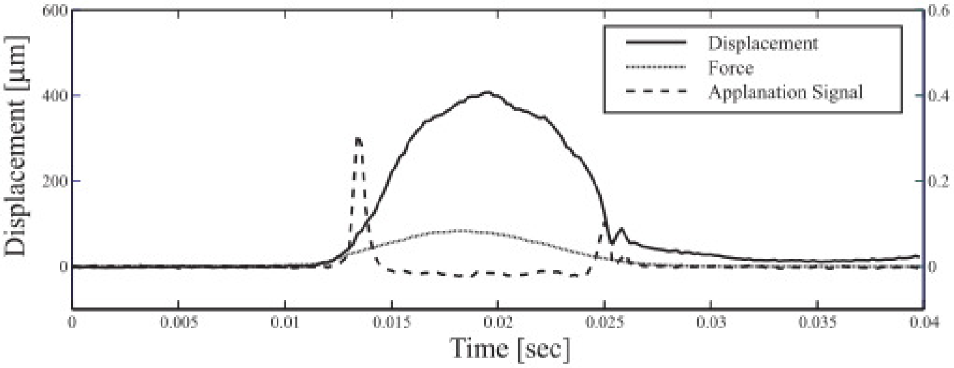

(a) Subject A (IOP = 10 [mmHg]).

Figure 3.6: Force, displacement, and applanation signal for a subject from Fig. 12 in [2].

The displacements in the experiments are calculated from a video captured by a high speed camera placed perpendicular to the eye axis. Therefore, the displacements are less than actual displacements when the cornea is concave. However, the difference of $2 \sim 3$ times is much larger than this effect. In addition, the difference of the peak value depends on IOP, and the linear adjustment of the stiffness cannot account for such difference. This will be further addressed and discussed in section 3.4.

Figs. 3.7 and 3.8 plot the responses $y(t)$ with the different viscous damping coefficients, c. The results show that the delay time Δt between the applied force $F(t)$ and the response $y(t)$ depends on the viscous damping coefficient, c. In the IOP measurement by air-puff tonometry, the IOP is usually estimated at the time between 15$\sim$16 ms. Fig. 3.8 enlarges the boxed region, 15$\sim$16 ms, of Fig. 3.7. The delay times Δt are 0 ms at $c = 0$ (without damping), 0.345 ms at $c = 0.03$, and 0.694 ms at $c = 0.06$, as shown in Fig. 3.8. In an IOP measurement by air-puff tonometry, 0.1 ms delay increases the IOP value by 0.8 mmHg. Therefore, in the IOP measurement by air-puff tonometry, the dynamic effect of the viscous damping coefficient is not negligible. In fact, such deviation will affect the accuracy of the IOP values, and should not be overlooked. On the other hand, the loading rate of GAT is very slow and $\dot{y}(t)$ in Eq. (3.1) is negligible. Thus, the effect of the viscous damping coefficient should be negligible in GAT. This means that if subjects have the same stiffness and different viscous damping property, their IOP will be the same by GAT but different by air-puff tonometry. This factor may cause an inconsistency of IOP values measured by GAT versus air-puff tonometry.

Fig. 3.9 shows the responses $y(t)$ with different masses of the cornea. The responses are practically the same even though the mass is changed by $\pm 33[\%]$. Therefore, in the IOP measurement by air-puff tonometry, the effect of the mass of the cornea is negligible.

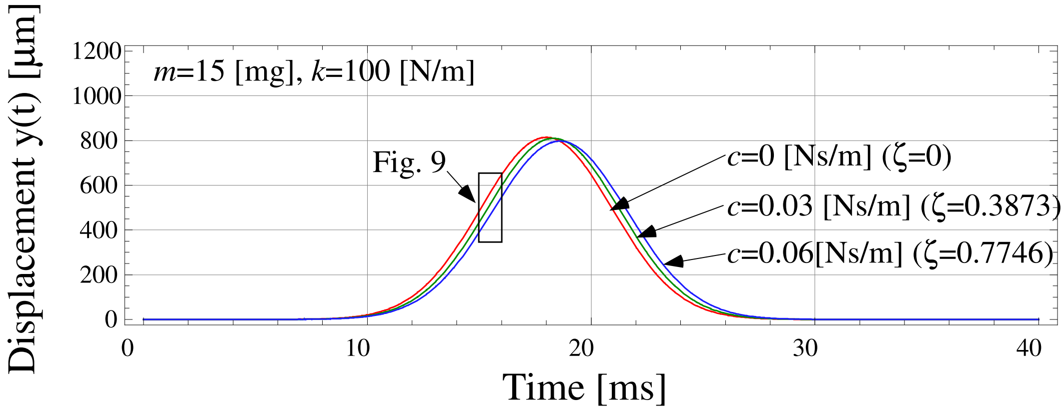

Figure 3.7: The responses $y(t)$ with different c.

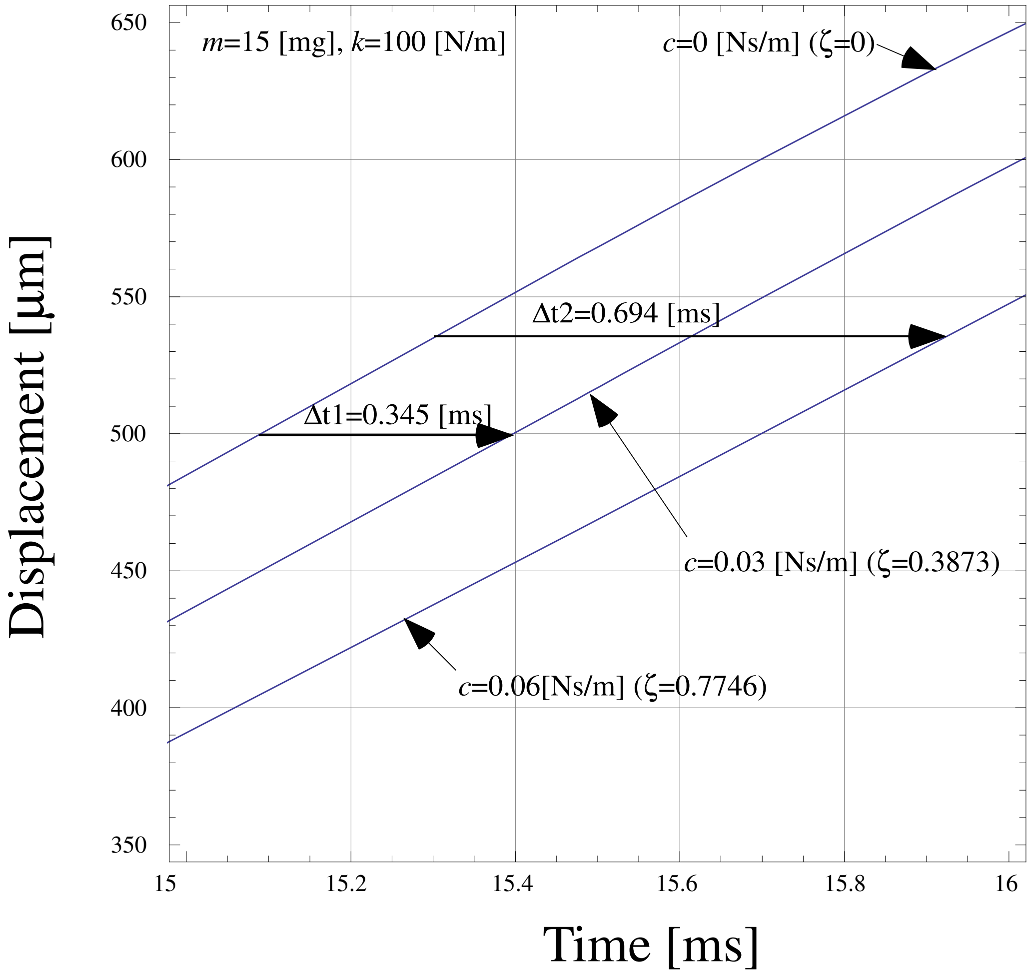

Figure 3.8: The responses $y(t)$ with different damping from time $= 15 \sim 16$ ms.

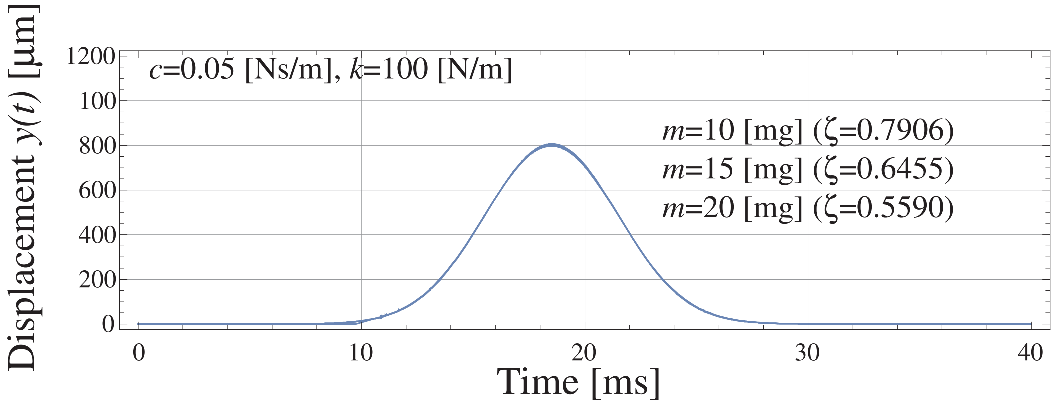

Figure 3.9: The responses $y(t)$ with different m

3.3 Modeling as a 2-DOF system

It is reported in [3] that some senior subjects have different types of displacement as shown in Fig. 3.10(b). The response appears to have two distinct regions. Therefore, a 2-DOF model is proposed in Fig. 3.11, in order to study the response of the senior subject.

In this model, m_1, c_1, and k_1 represent the anterior chamber, the same as the previous model in Fig. 3.1. The snapshot of the senior subject taken in [3] showed that the eyeball itself moved linearly. Therefore, m_2 represents the total mass of the eyeball and c_2 and k_2 represent the damping and stiffness between the eyeball and the eye socket, respectively. The equation of motion can be arranged in the form of the linear system equation

$$\dot{\mathbf{x}}(t) = \mathbf{A}\mathbf{x}(t) + \mathbf{B}\mathbf{Q}(t) \tag{3.9}$$

where

$$\begin{aligned}
\mathbf{x}(t) &= \begin{bmatrix} q_1(t) & q_2(t) & \dot{q_1}(t) & \dot{q_2}(t) \end{bmatrix}^T \\
\mathbf{M} &= \begin{bmatrix} m_1 & 0 \\ 0 & m_2 \end{bmatrix}, \mathbf{C} = \begin{bmatrix} c_1 & -c_1 \\ -c_1 & c_1+c_2 \end{bmatrix} \\
\mathbf{K} &= \begin{bmatrix} k_1 & -k_1 \\ -k_1 & k_1+k_2 \end{bmatrix} \\
\mathbf{A} &= \begin{bmatrix} \mathbf{0} & \mathbf{I} \\ -\mathbf{M}^{-1}\mathbf{K} & -\mathbf{M}^{-1}\mathbf{C} \end{bmatrix}, \mathbf{B} = \begin{bmatrix} \mathbf{0} \\ \mathbf{M}^{-1} \end{bmatrix} \\
\mathbf{Q}(t) &= \begin{bmatrix} \mathbf{F}(t) & 0 \end{bmatrix}
\end{aligned} \tag{3.10}$$

By arranging the equation of motion in the linear system equation, the responses $q_1(t)$ and $q_2(t)$ can be obtained by solving the dual eigenvalue problem [28]. In the case of multi-DOF, $\Phi(t) = e^{\mathbf{A}t} = \mathbf{X}e^{\Lambda t}\mathbf{Y}^T$ where $\mathbf{X}$ contains the right eigenvectors of matrix $\mathbf{A}$, $\mathbf{Y}$ contains the left eigenvectors of matrix $\mathbf{A}$, and Λ is a diagonal matrix consisting of the eigenvalues of matrix $\mathbf{A}$. The eigenvector matrices have the relationship $\mathbf{Y}^T\mathbf{X} = \mathbf{I}$ and

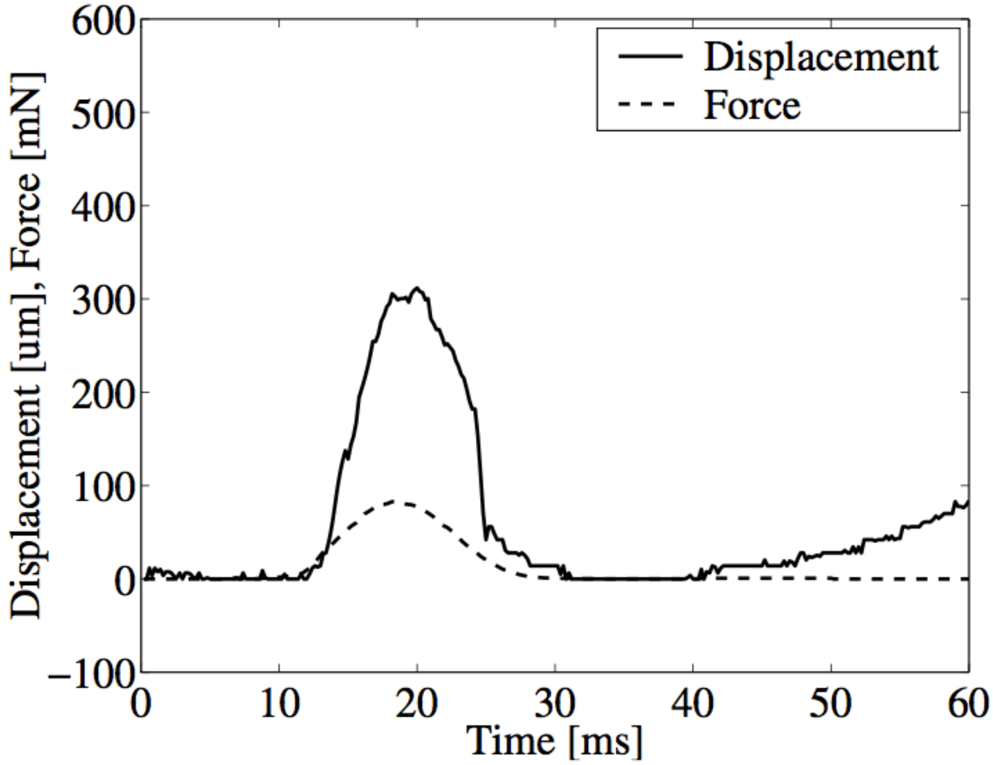

(a) Young subject

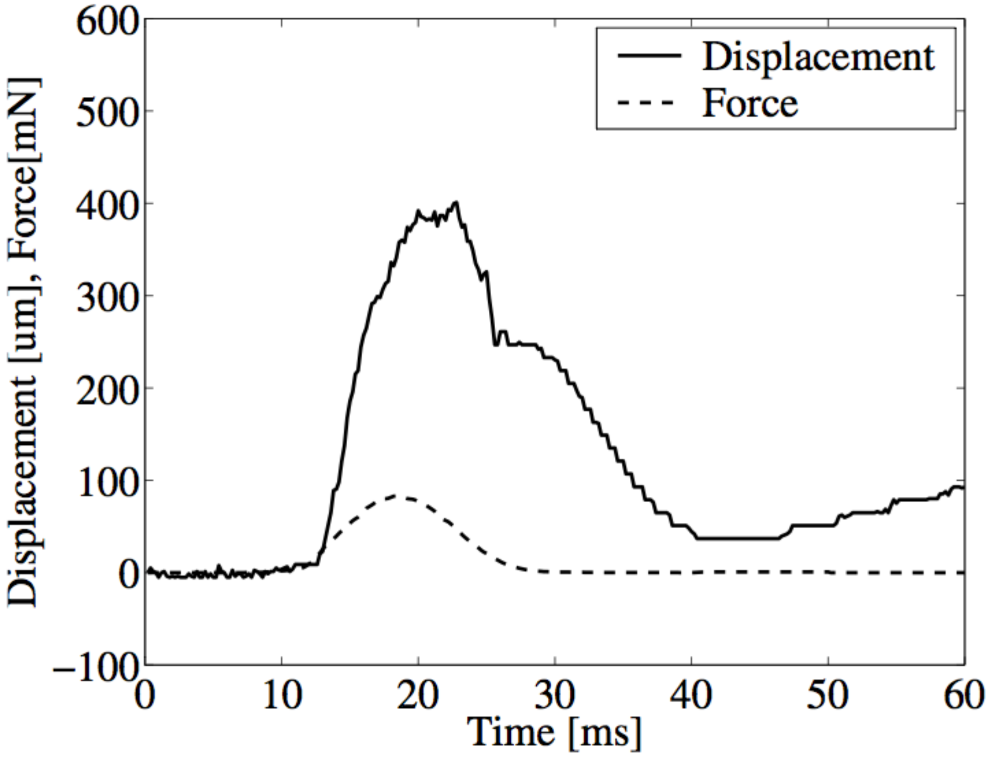

(b) Senior subject

Figure 3.10: Plots of the dynamic responses of the tip of the cornea for (a) young and (b) senior subjects from [3]

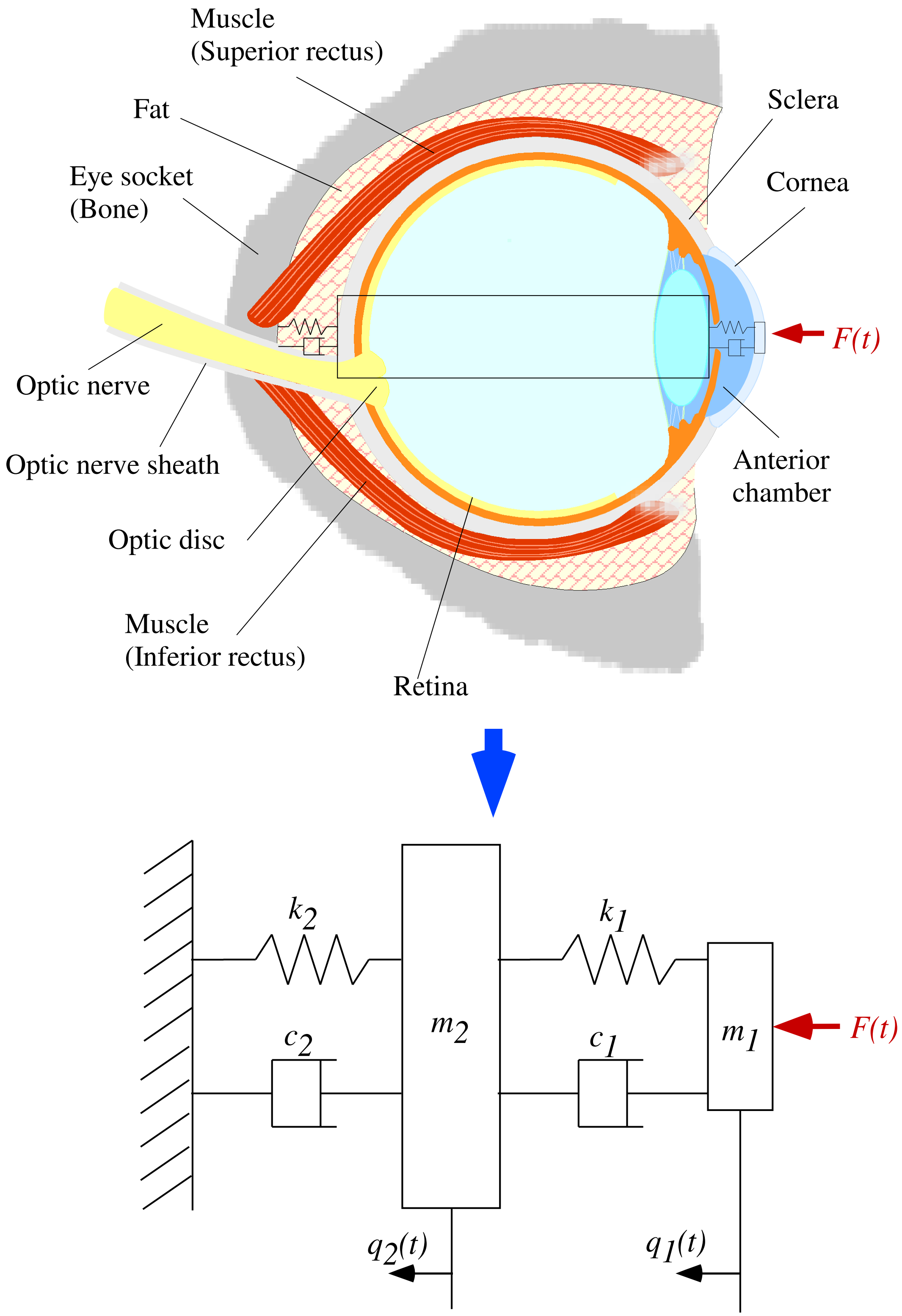

Figure 3.11: Dynamic modeling of a human eyeball with 2-DOF system

$\mathbf{Y}^T\mathbf{A}\mathbf{X} = \Lambda$. Then, the response can be obtained by the following equation

$$\mathbf{x}(t) = \mathbf{X}e^{\Lambda t}\mathbf{Y}^T\mathbf{x}(0) + \int_0^t \mathbf{X}e^{\Lambda\tau}\mathbf{Y}^T\mathbf{B}\mathbf{Q}(t-\tau)d\tau \tag{3.11}$$

Fig. 3.12 shows the responses $q_1(t)$ and $q_2(t)$ calculated by Eq. (3.11) with the parameters $m_1 = 15$ mg, $c_1 = 0.05$ Ns/m, $k_1 = 100$ N/m, $m_2 = 7.6$ g, $c_2 = 0.05$ Ns/m, and $k_2 = 200$ N/m. The values of m_1 and c_1 are the same as those in the previous section. The value of k_1 is chosen based on the range of normal IOP and the related stiffnesses calculated by Eq. (3.8). The value of m_2 is set by the typical weight of a human eyeball. The value of c_2 is assumed to be the same as c_1. The value of k_2 is adjusted by trial-and-error with comparison to the simulated $q_1(t)$ and the experimental results in Fig. 3.10(b). The response $q_1(t)$ in Fig. 3.12 reproduces the shape of the experimental result in Fig. 3.10(b). The displacement $q_1(t)$ rises at 10 ms and the displacement $q_2(t)$ rises at 15 ms. There is a 5 ms delay between $q_1(t)$ and $q_2(t)$. In the early phase of the response, only the cornea, m_1, deformed and the whole eyeball, m_2, did not move. The movement of the whole eyeball is delayed because the inertia of the whole eyeball is much larger than the inertia of the cornea.

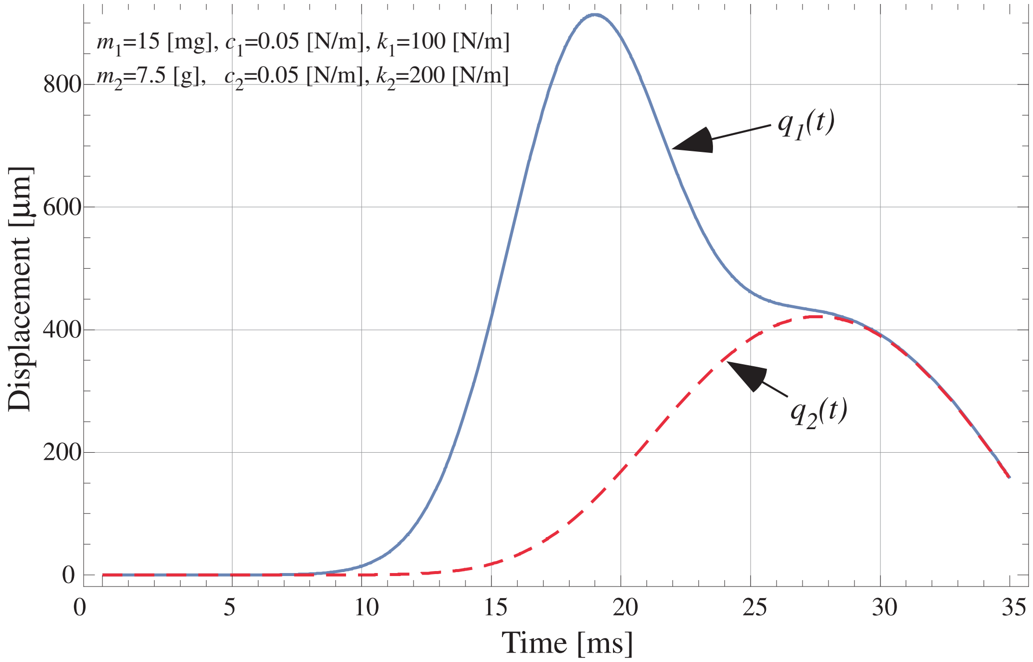

Figure 3.12: The responses $q_1(t)$ and $q_2(t)$.

Fig. 3.13 illustrates the responses of $q_1(t)$ when k_2 is changed from 200 N/m to 2000 N/m, corresponding to a senior (aging) and a young subject, respectively. The peak value of the displacement for the senior subject is slightly larger. In general, the shapes of the responses are very similar before 16 ms, but quite different thereafter. The IOP measured by air-puff tonometry is usually determined before 16 ms. Therefore, the difference between young and senior subjects generally will not affect the IOP measurement by air-puff tonometry.

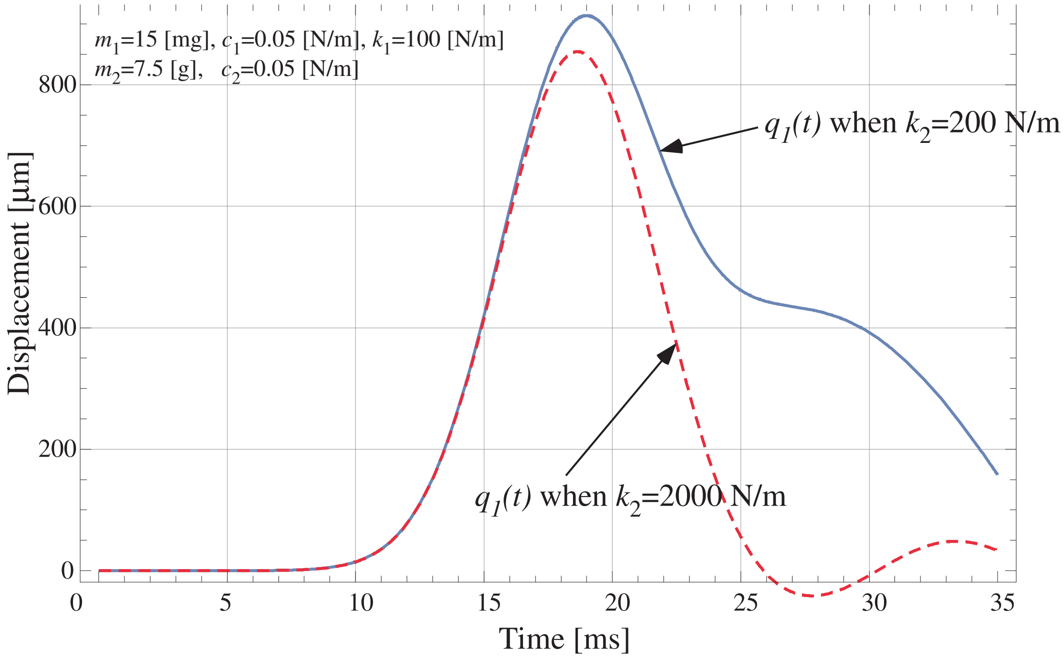

Figure 3.13: The responses $q_1(t)$ with different k_2 corresponding to young and senior subjects

3.4 DISCUSSIONS

In general, a hemispherical soft material exhibits non-linear stiffness in contact [29]. However, the stiffness k_{nct} was constant based on the experimental data [27]. This is probably because of the structure of the anterior chamber which is composed of the elastic shell, consisting of the cornea and the iris, filled with the liquid, aqueous humour. This linear elasticity of the hemisphere will be an interesting topic.

The difference in the magnitude of the displacement between simulation and experiments cannot be calibrated by the linear transformation of the stiffness, k, since the difference is larger when IOP is higher. We assumed that the stiffness, k, is constant based on GAT. A big difference between GAT and air-puff tonometry is the loading rate. The loading rate by a probe and an air puff are different, and it is known that the stiffness depends on the loading rate in viscoelastic materials, such as human tissues or eyeball. The difference of the loading rate can be considered as the source of the difference in the displacements.

3.5 CONCLUSIONS

In this Chapter, we presented the modeling of the eyeball on the IOP measurement by air-puff tonometry with parameter study and experimental results. The main contributions of this Chapter include:

- Dynamics of air puff causes the damping effect of the eyeball which results in a time delay in the response and affects the IOP measurement, as opposed to the quasi-static measurement of GAT. Therefore, different damping characteristics of the eyeballs will affect the accuracy of the IOP measurement by air-puff tonometry. This is one of the most significant findings regarding the air-puff tonometry when comparing the IOP measurements between GAT and air-puff.
- It is also found that the mass property of the eyeballs is negligible; that is, IOP measurement does not depend on having larger or smaller eyeballs.
- The stiffness between the eyeball and the eye socket can change the shape of displacement when an air puff is applied but does not affect the IOP measurement by air-puff tonometry.

Chapter 4

An Experimental Study of Biologically Inspired Artificial Skin Sensors Under Static Loading and Dynamic Stimuli

This Chapter presents an experimental study of the bio-inspired artificial skin consisting of silicone and embedded strain gages, in which silicone imitates the epidermis and dermis, and strain gages mimic mechanoreceptors. The strain gages are embedded in silicone under different configurations as mechanoreceptors in humans skin. Both static displacement and dynamic excitations are applied in arbitrary positions, with different magnitudes and frequencies. The responses are observed by measuring the output signals from strain gages. Comparison with FEM simulation of static displacement shows intuitive agreement. The responses to dynamic excitation in typical frequency range of human mechanoreceptors are obtained both experimentally and with simulation of dynamic modeling. We found that each configuration has advantages and disadvantages. This Chapter shows how strain gages embedded in silicone will behave in response to both static and dynamic excitations, and suggests modeling and fundamental concepts to design a bio-inspired artificial skin sensor.

4.1 Introduction

Human skin is very sensitive and capable of detecting different types of stimuli quite accurately. Specifically, human skin on fingers serves as tactile sensors that detect both static and dynamic stimuli in a wide range of frequencies. When humans grasp an object, fingertips and associated mechanoreceptors can estimate various attributes of the contact interface between fingertips and the grasped object, such as vibration, normal force, friction force, slip or stick, and deformation of the object. Many attributes of the contact interface are detected qualitatively, while others may be detected somewhat quantitatively. The sensing ability of such somatosensors facilitates control of grasping and manipulation, and is indispensable in dexterous manipulation.

Inspired by such human skin sensors, artificial skins were designed and fabricated with embedded strain gages, in which silicone imitates epidermis and dermis, and strain gages mimic mechanoreceptors. Experimental and theoretical studies are conducted using both static loading and dynamic stimuli. This Chapter explores how strain gages embedded in silicone behave in response to both static and dynamic excitations, and suggests mechanisms and fundamental concepts to design bio-inspired artificial skin sensors. Such an artificial skin sensor can be an excellent sensor for robots that are employed to manipulate soft or fragile material that requires delicate sensing and control.

4.1.1 Literature review

4.1.1.1 Mechanoreceptors

Human skin has four types of mechanoreceptors which are located in different places as shown in Fig. 4.1 and sense different types of mechanical stimuli. The mechanoreceptors are connected to nerves and discharge impulse signals at a certain frequency under the specific conditions. The mechanoreceptors can be categorized by the adaptation, fast or slow, and the receptive fields, small or large, as shown in Fig. 4.2.

Fast-Adapting (FA) mechanoreceptors detect velocity or acceleration and Slow-Adapting (SA) mechanoreceptors detect displacement. FA mechanoreceptors discharge impulse signals only if applied strain is changing, such as during loading and unloading, and do not discharge impulse signals if applied strain is constant. SA mechanoreceptors always discharge impulse signals if strain is applied as shown in Fig. 4.2.

A Type I mechanoreceptor has small receptive area and a Type II mechanoreceptor has large receptive area. Type I mechanoreceptors, Meissner corpuscle and Merkel's disk, are located in near the epidermis and Type II mechanoreceptors, Ruffini's corpuscle and Pacinian corpuscle, are located in the deeper skin, such as in the dermis or the subcutis. The mechanoreceptors near the stimulus can detect the exact location of the applied stimulus and the mechanoreceptors far from the stimulus can detect the stimulus from large area because the applied stimulus will easily propagate through soft tissues such as dermis and subcutis.

Fingertips are most sensitive for tactile sensing in human skin and the density of Type I mechanoreceptors, especially FA I, is much higher than other locations as shown

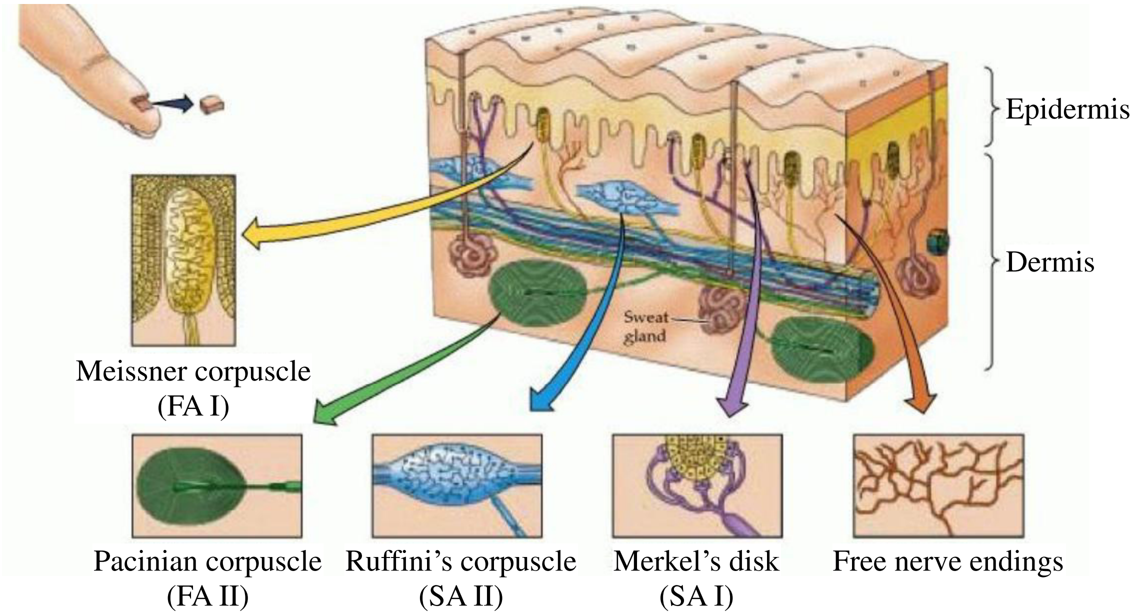

Figure 4.1: The cross section of human finger [1]

in Fig. 4.3. Intuitively, humans will trace surfaces when they want to detect the surface roughness or find scratches by using a fingertip. It is reasonable to consider that the FA I (Meissner) detects the vibration generated by the tracing motion and surface roughness is estimated by the frequency of the vibration. It is reported in [5] that the sensitivity of each mechanoreceptor, the minimum amplitude to detect vibration, is almost independent

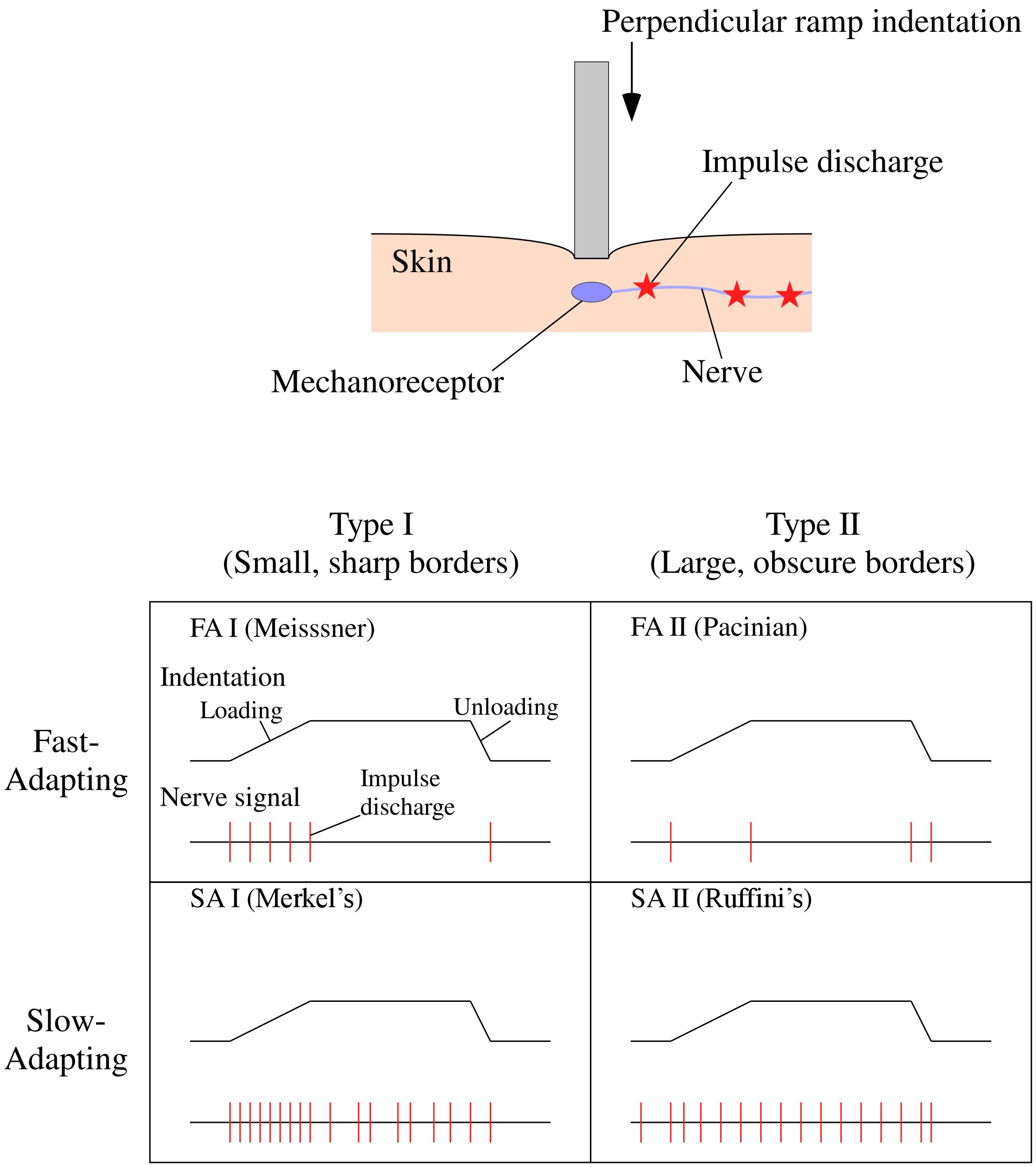

Figure 4.2: Types of mechanoreceptors [4]

of the frequency of the vibration in SA I (Merkel's) and depends on the frequency of the vibration in FA I (Meissner) and FA II (Pacinian). For instance, FA I (Meissner) is most

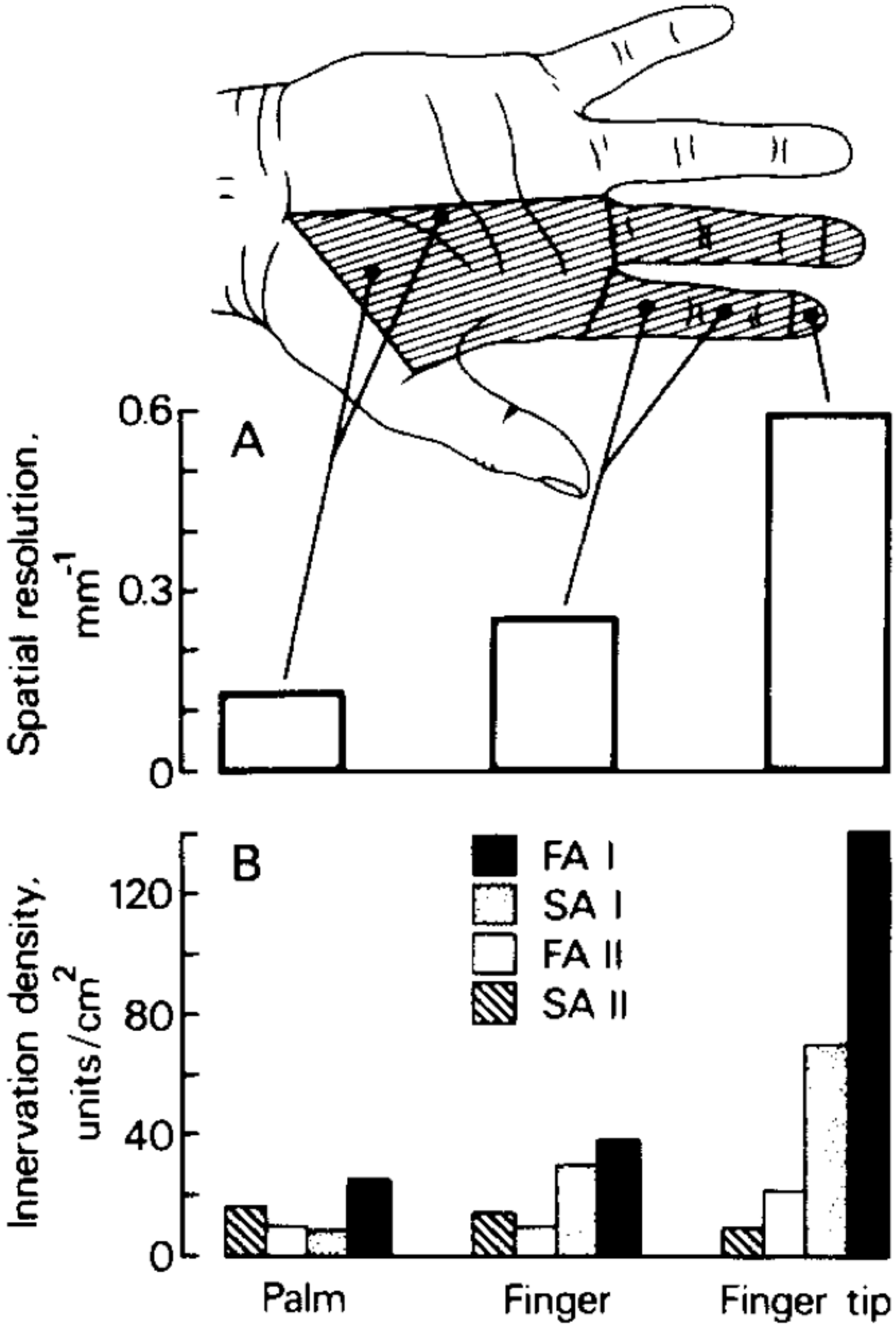

Figure 4.3: The density of mechanoreceptors [4]

sensitive at around 30Hz and FA II (Pacinian) is most sensitive around 200Hz. Intuitively, the sensitivity of human fingertip to detect the surface roughness depends on the tracing speed. The tracing speed changes the frequency of the vibration on the fingertip and the frequency of the vibration affects the sensitivity of the mechanoreceptors, so the sensitivity changes to detect the surface roughness can be explained by the frequency changes. It is well known that each mechanoreceptor has different properties and for tactile sensing.

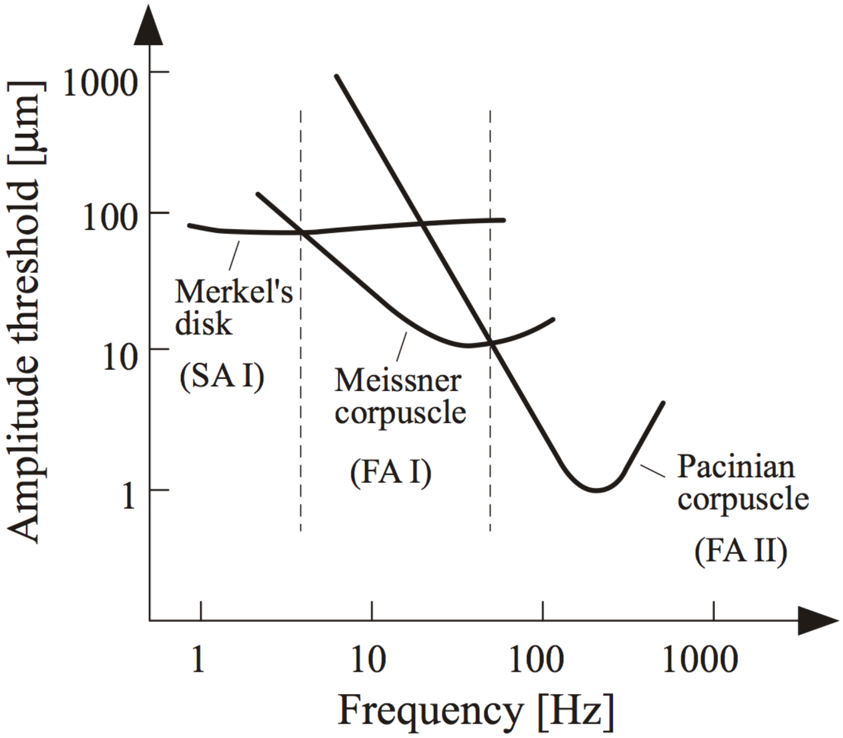

Figure 4.4: Thresholds of tactile receptors for vibratory stimulus. [5]

4.1.1.2 Tactile sensing

Tactile sensing is a process of determining properties of a surface, such as roughness, texture, and friction. Lee and Nicholls summarized the progress in tactile sensing up to 1998 in [30], which includes cutaneous sensors, sensing fingers, soft materials, industrial robot grippers, multi-fingered hands, probes and whiskers, analysis of sensing devices, haptic perception, and processing sensory data. Zhang *et al.* developed a tactile sensor which can detect the hard lump in a soft background by tracking the contact surface [31]. Puangmali *et al.* applied the tactile sensing techniques in minimally invasive surgery [32]. Lumelsky *et al.* summarized a sensitive skin consisting of a sensing element array which is a thin/flexible sheet and covers a robot or human surface. It is mentioned that wiring and data processing is an issue because of the number of sensing elements required to cover a large area [33]. Hidaka *et al.* designed a sensor which is size-equivalent to a human finger so that it can emulate the epidermal ridge and equip a robot hand with the ability to detect vibration patterns in a manner similar or equal to that of a human finger [34]. Takamoku *et al.* developed an artificial skin by PVDF films and strain gages, and the skin can discriminate haptically between different objects by tapping and squeezing the objects [35]. Mukai *et al.* designed a tactile sensor covered with an elastic sheet, and showed that the elastic sheet affects the frequency response [36]. Mukai *et. al* and Shimojo *et. al* showed that hysteresis and creep characteristics, common phenomena in soft materials, exist in their tactile sensor [37, 36].

4.2 Experimental Study

4.2.1 Experimental Setup

The layout of the design of the artificial skin with the location and orientation of the strain gages is shown in Fig. 4.5. Three strain gages are embedded in the artificial skin. Two of them are embedded in the horizontal direction, parallel to the largest surface, and one of them is embedded in the vertical direction, as shown. The vertical strain gage can be considered as the Meissner and the horizontal strain gage can be considered as the Raffini's illustrated in Fig. 4.1.

The artificial skin is fabricated by molding. Fig. 4.6 illustrates the process of fabrication. The strain gages are positioned and placed in the mold into which the mixture of silicone powder and thinner fluid is poured. It takes about one week for the silicone materials to cure. After that, the mold is removed to obtain the artificial skin. Fig. 4.7 shows a final product of molded skin.

The strain gages are KYOWA KFG-120. An illustration of the strain gage is in Fig. 4.8(a). The strain gage consists of a base made of plastic film and resistive foil made of metal. When the base is deformed by applied forces, the metallic piezoresistive foil is also deformed. The resistance of the metal foil is shown in equation (4.1), where ρ is the static resistivity, ℓ is the length of the resistive foil and A is the cross-sectional area of the resistive foil. When the metallic resistive foil is subject to tension, as shown in Fig. 4.8(b) and (d), the length ℓ will increase and the area A will decrease, resulting in a net increase of the resistance of strain gage. On the other hand, when the metallic resistive foil is compressed, as shown in Fig. 4.8(c) and (e), the resistance of the strain gage will decrease. All four types of deformation in Fig. 4.8(b-e), or combination of them, can happen in the artificial skin sensor. Thus, the net resistance of the strain gage will depend on the applied load with a combination of effects discussed above.

$$R = \rho \frac{\ell}{A} \tag{4.1}$$

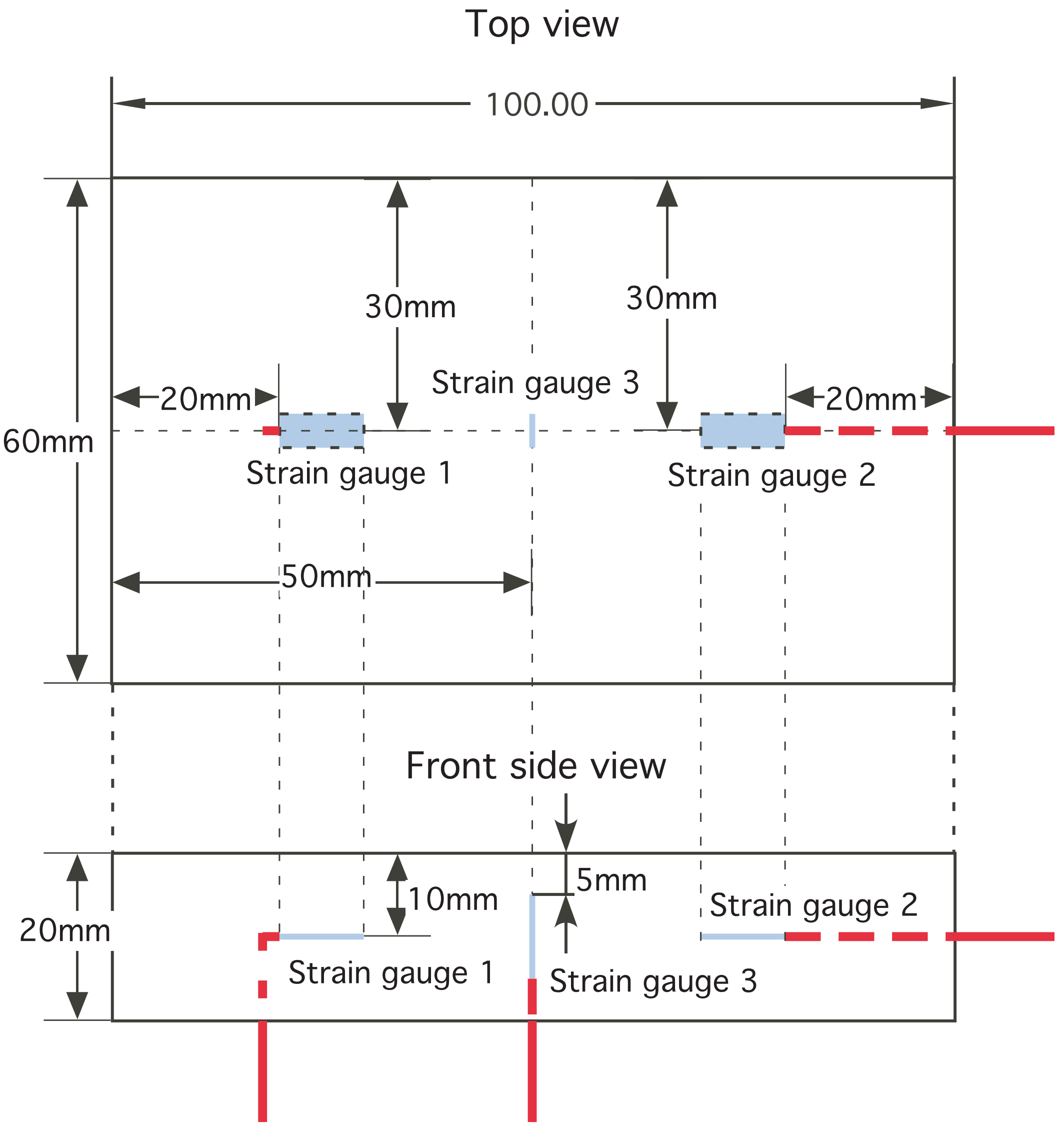

Figure 4.5: The design specification of the artificial skin

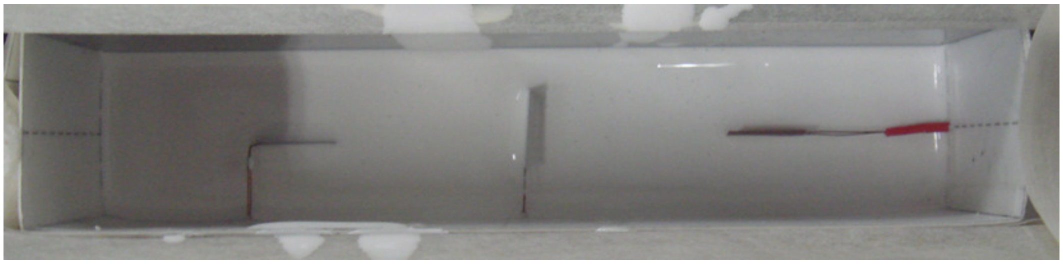

Figure 4.6: The fabrication of the artificial skin

Fig. 4.9 shows the integrated system for conducting experiments. The output signal of the

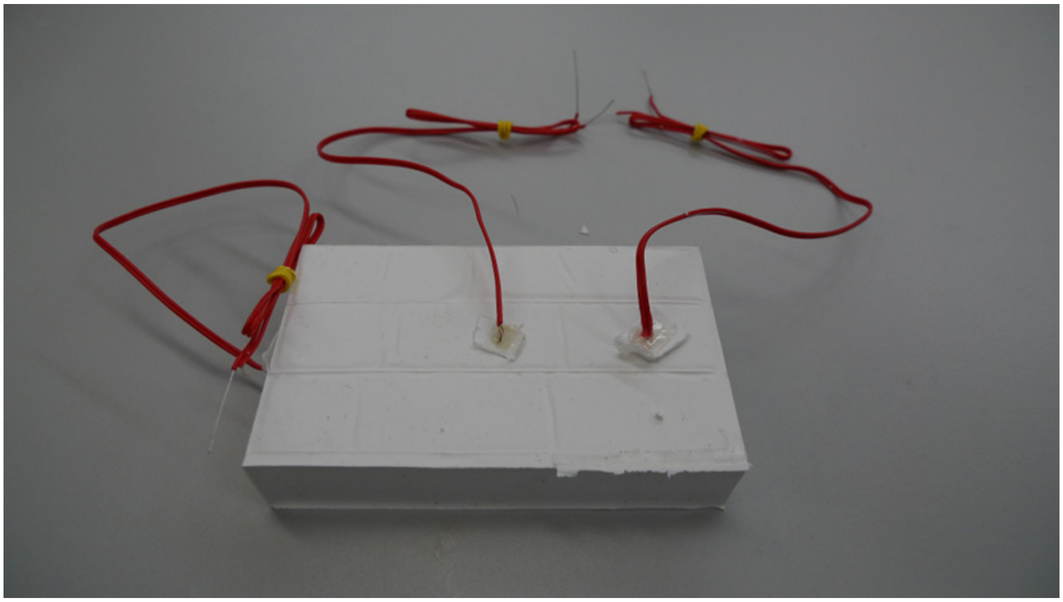

Figure 4.7: A final product of the artificial skin

strain gage is small; therefore, a Wheatstone bridge is used to detect the small change in resistance [38]. The output signals are conditioned by an amplifier circuit, connected to a PC-based data acquisition system to record the signal for analysis.

Fig. 4.10(a) shows the Wheatstone bridge where $R3$ is the subject strain gage which is embedded in the artificial skin sensor. The $R4$ is a strain gage for temperature compensation. For the purpose of temperature compensation, we require

$$\frac{R_1}{R_3} = \frac{R_2}{R_4}$$

The resistance $R1, R2$ are 120Ω resistors and R_p is a 100 KΩ potentiometer.

Generally, the Wheatstone bridge is calibrated by setting the initial value, without stress, V_{o1_ini} to zero by adjusting the potentiometer. In the experiments, we measure both positive and negative changes in strain gages. Equation (4.2) shows that the circuit is able to obtain bi-directional measurements of the strain gage when $\Delta R3$ is either positive or negative. Equation (4.2) is obtained by assuming $R1' \simeq R2' \simeq R3 \simeq R4$ and $\Delta R3 \ll R3$

$$V_{o1} = \frac{(1 - \frac{R1'R4}{R2'R3}) + \frac{\Delta R3}{R3}}{4} E = V_{o1\_ini} + \frac{\Delta R3}{4R3} E \tag{4.2}$$

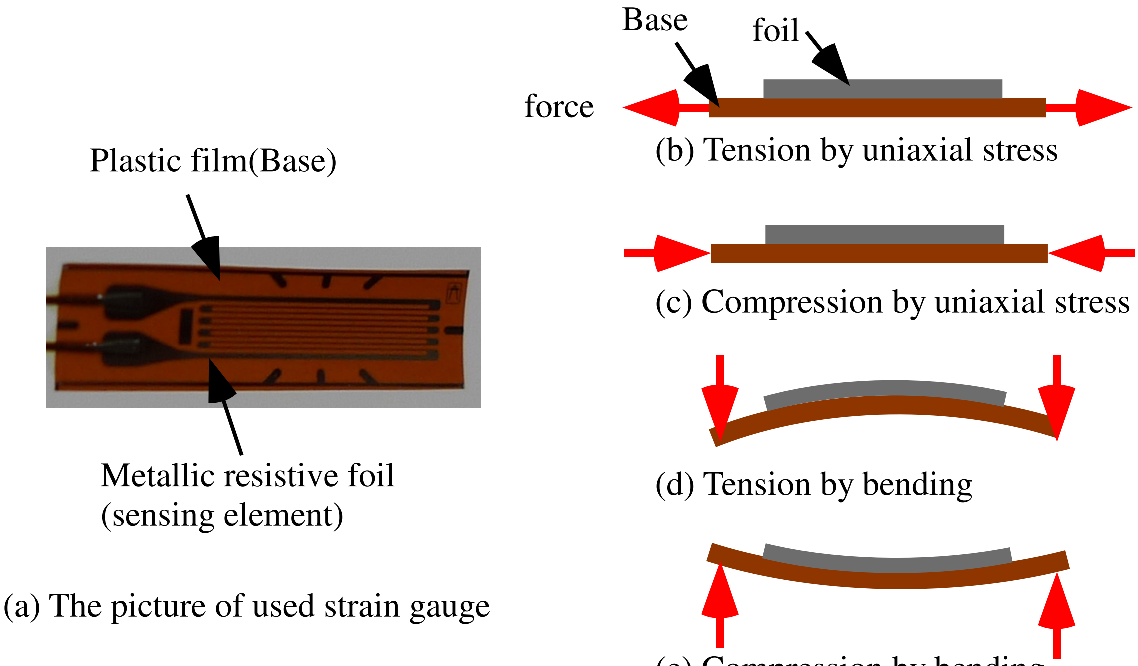

(a) The picture of used strain gauge

(b) Tension by uniaxial stress

(c) Compression by uniaxial stress

(d) Tension by bending

(e) Compression by bending

Figure 4.8: The structure and mechanism of strain gage

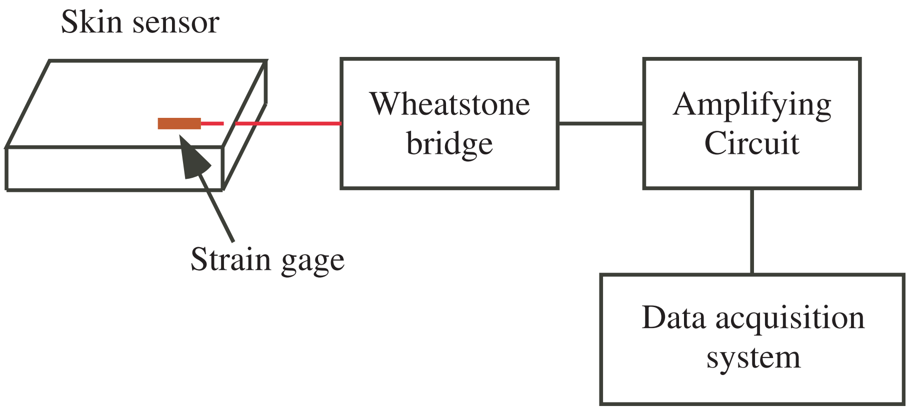

Figure 4.9: The overview of the experimental system

where E is the supply voltage, $\Delta R3$ is the change of $R3$ under loading, V_{o1_ini} is the output signal without any load or strain when $\Delta R3 = 0$, and $R1'$, $R2'$ are

$$R1' = \frac{R1R_p\alpha}{R1+R_p\alpha},\ R2' = \frac{R2R_p(1-\alpha)}{R2+R_p(1-\alpha)},\ 0 \le \alpha \le 1 \tag{4.3}$$

where α is the angle of the potentiometer.

Fig. 4.10(b) shows the instrumentation amplifier. The amplifier is suitable to amplify the tiny differential signal. The gain of the amplifying circuit is set to 2355.

Equation (4.4) shows the relationship between the output signal V_o and the strain of the subject strain gage. Based on equation (4.4), the strain of the subject strain gage is $\varepsilon = 1.7 \times 10^{-4}$ when the output signal V_o is increased by 1V.

$$\varepsilon = \frac{4}{K \cdot E}\frac{\Delta V_o}{Gain} = 1.70 \times 10^{-4}\Delta V_o \tag{4.4}$$

where $K = 2$ is the gage factor.

4.2.2 Experimental Procedure

The specimen of artificial skin was placed onto a hard wood surface. The output of the strain gage with conditioning circuit was connected to an oscilloscope and the PC-based data acquisition system.

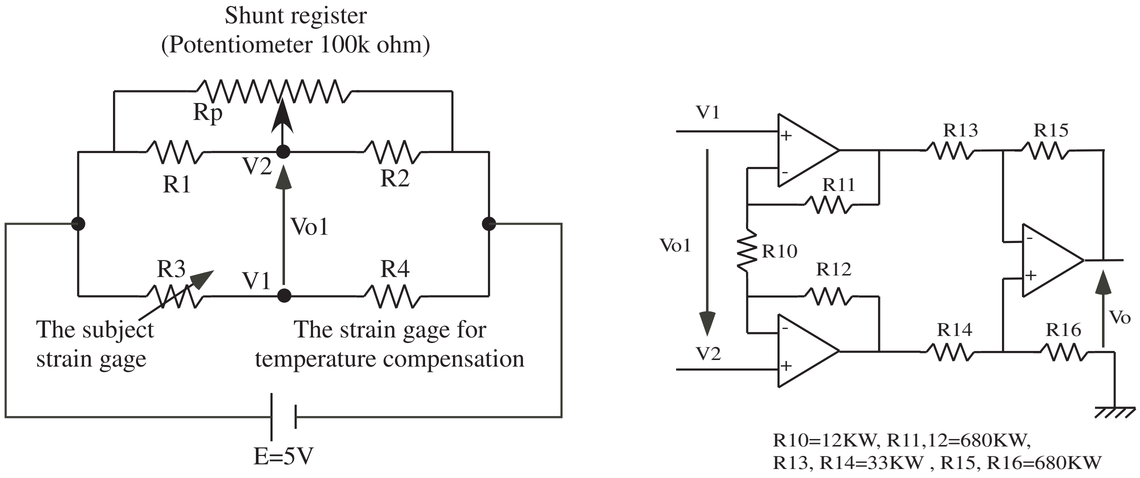

(a) (b)

Figure 4.10: The Wheatstone bridge and amplifying circuit

The tip of the indenter, having a diameter of 4 mm, was used for indentation. The oscilloscope was used to determine an increase or decrease in voltage. A data acquisition system was used to record the voltages as the specimen was compressed. The force was applied for 35 seconds and then removed for 25 seconds. This was repeated 3 times for each point of interest. Various points were tested in experiments. The movement of the indenter is indexed based on the grid papers on which the specimen rests.

4.2.3 The experiment with a constant force/displacement

Fig. 4.11 shows the experimental setup to apply a constant force/displacement by a static weight. The diameter of the indenter is 4*mm* and it passes through two holes in two plates which are parallel to the top surface of the artificial skin sensor. It applies force normal to the surface of the skin sensor. A disk is fixed in the top side of the indenter by a screw so we can adjust the height of the disk and vary the static weight. Since the disk does not touch the upper plate, we consider that all force caused by the static weight is applied onto the skin sensor, assuming the friction force between the plates and indenter is negligible. The skin sensor rests on an acrylic plate with two holes. The cables of strain gages 2 and 3, shown in Fig. 4.5, go through the holes.

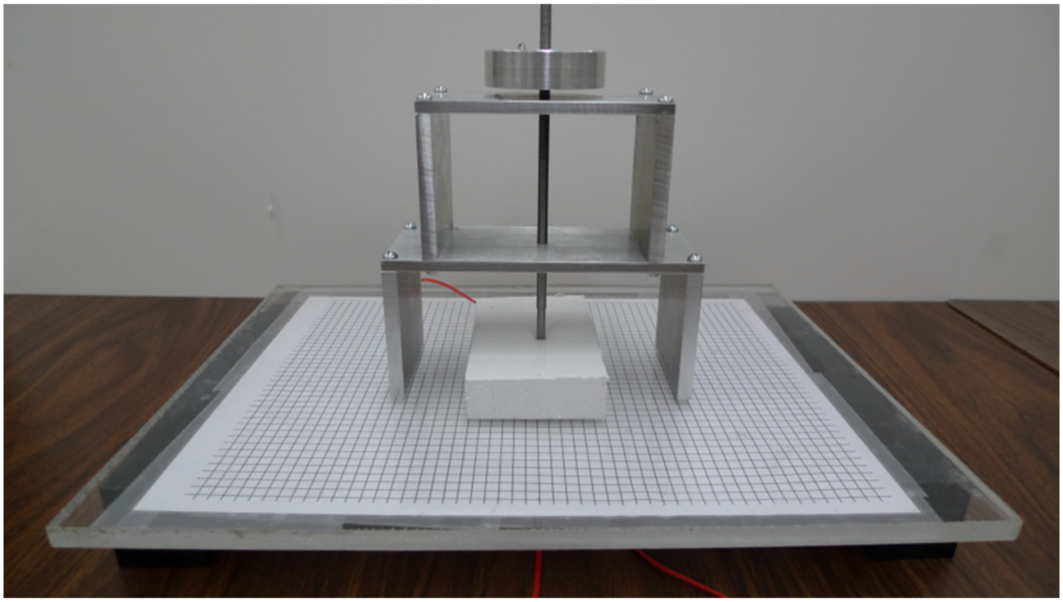

Figure 4.11: The equipment to apply static displacement by a static weight

4.2.3.1 With the vertical strain gage

Fig. 4.12 shows the points where static loading is applied by a static weight, as shown in Fig. 4.11. The strain gage 3, shown in Fig. 4.5, is used as the subject strain gage. Each point is poked three times by the indenter with the 215g static weight. Before starting experimentation, the initial value of the output signal of the amplifying circuit, V_o, is set to approximately 2.5V by adjusting the potentiometer shown in Fig. 4.10. The starting value of each experiment represents the signal level without loading.

Fig. 4.13 shows the output signal V_o recorded by the data acquisition system. The sampling rate of the data acquisition system is 1kHz. The results show that the output signal increased when the right side of the strain gage is poked, and decreased when the left side of the strain gage is poked. This indicates that when the right side of the strain gage is poked the strain gage is stretched, and when the left side of the strain gage is poked the strain gage is compressed. In addition, the magnitude of the output signal is reduced when the distance between the strain gage and the point of the indentation is increased. It

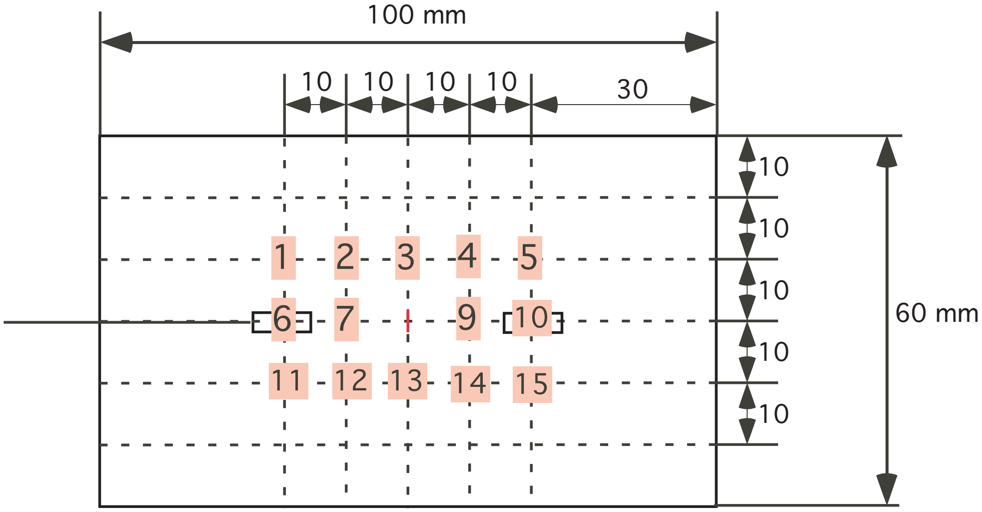

Figure 4.12: The points pressed by the indenter.

is inferred that the strain gage whose configuration is vertical to the contact surface is bent in different directions, depending on which side of the strain gage is poked.

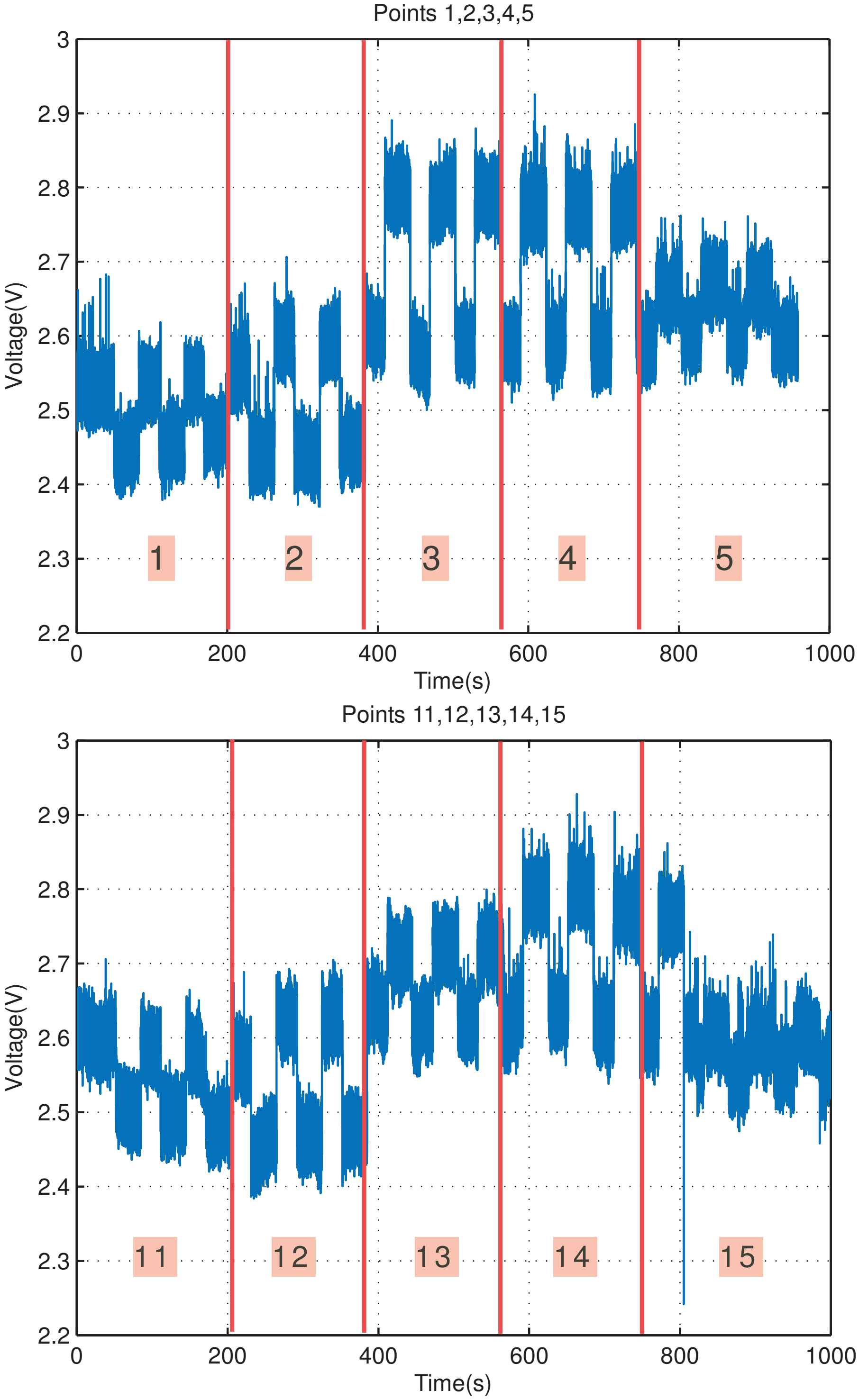

Figure 4.13: The experimental results with static weight and vertical strain gage

To confirm this hypothesis, we performed a finite element method (FEM) analysis by ANSYS. Fig. 4.14 shows the setup of the FEM analysis. We did a 2D analysis to simplify the problem. The applied displacement is based on the indenter's diameter and the observed magnitude of the indentation during the experiment. The width is 4 mm, and the depth is 9 mm. Regarding the boundary conditions, we assumed that the surface between the skin sensor and the supporting acrylic plate does not deform in either X or Y directions.

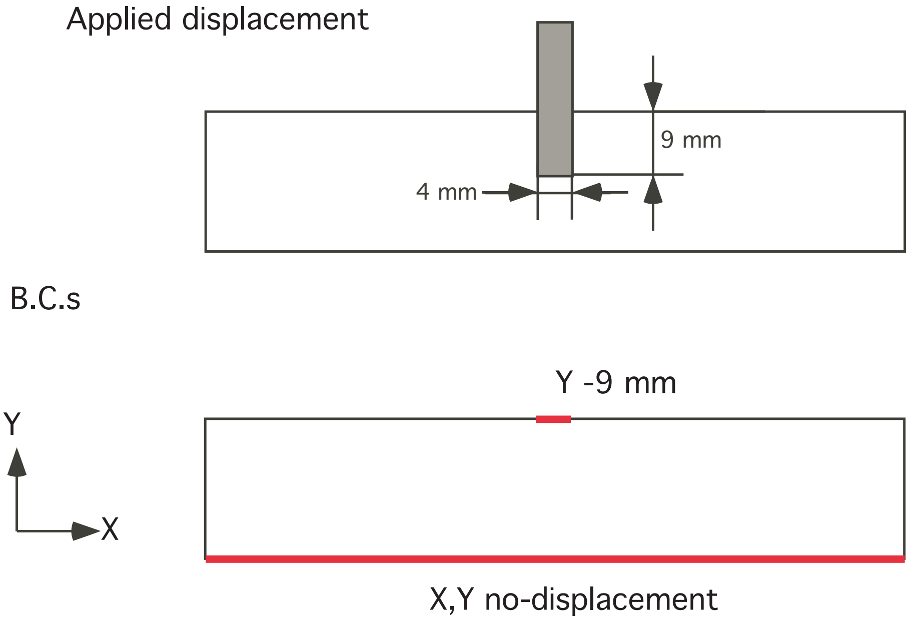

Figure 4.14: The FEM simulation and setup

Fig. 4.15 shows a result of the FEM analysis. The mesh size of the FEM analysis is 1mm. The result shows the original shape and deformed shape. The red lines show the deformation of the vertical line 10 mm away from the center of the indentation. The enlarged side views show shapes of the vertical strain gages when points 9 and 7 (in Fig. 4.12) are pressed. This result shows that the top surface is stretched to the center of the indentation, the bottom surface is fixed, and the middle section is pushed away from the center of the indentation by the Poisson effect. The vertical strain gage will bend as a result. Based on the structure and mechanism of strain gage shown in Fig. 4.8, the left side strain gage is under tension and the right side strain gage is under compression and these results are consistent with the experimental results.

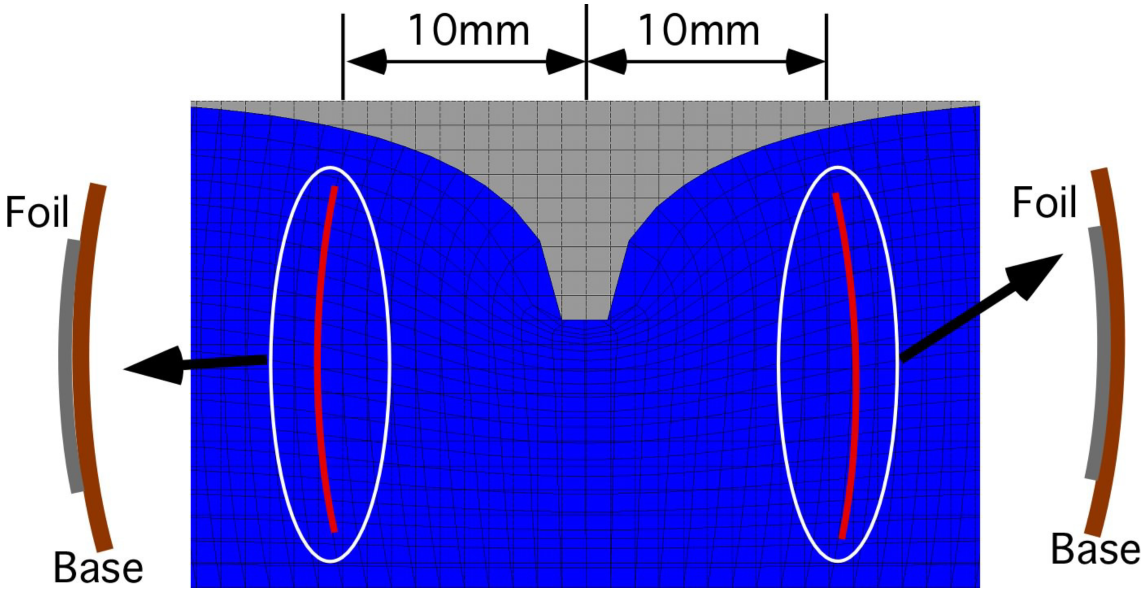

Figure 4.15: The FEM result

4.2.4 Experiments with dynamic stimuli

Fig. 4.16 shows the experimental setup for the application of dynamic stimuli to the artificial skin. The shaker, a device used in vibration testing to excite the structure, attached to the frame is used to apply vibrating excitation and dynamic stimuli to the skin sensor. The frequency of the vibration is regulated by the function generator, and the magnitude of the vibration is controlled by the input voltage to the shaker.

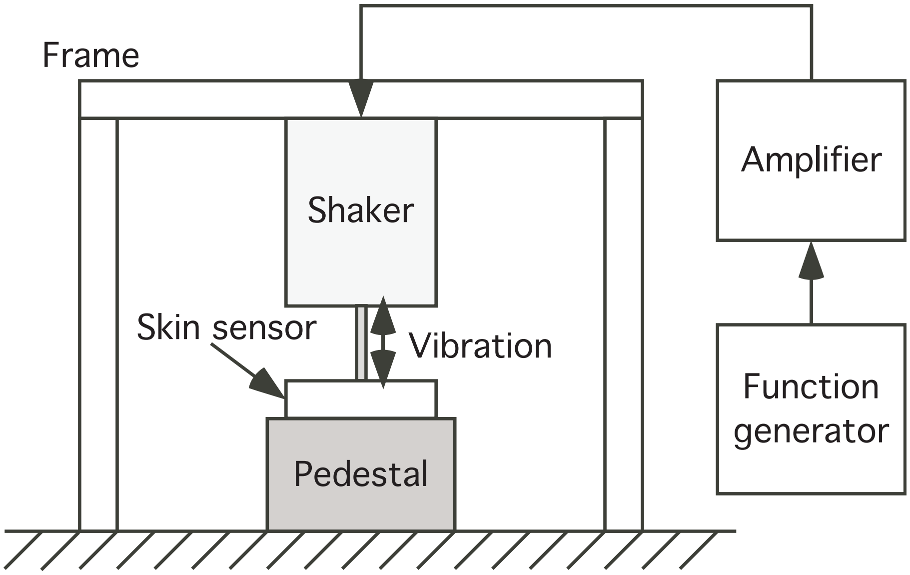

Figure 4.16: The experimental setup for the study of frequency response

At the beginning of each test, the tip of the shaker is moved to barely touch the surface of the specimen (< 1 mm). Different frequencies, from 5 Hz to 100 Hz, were applied in the experiments. Between each test, the specimen rests for one minute in order to restore it to its original equilibrium state. A data acquisition system recorded the signals generated by the embedded strain gage with a sampling rate of 10kHz.

Experimental results under different frequencies of excitation are plotted in Figs. 4.17, 4.18 and 4.19. From the experimental results, we observed two interesting phenomena. First, with the increase of input frequency, the magnitude of the signal measured by the embedded strain gage decreases. Second, when contact between the indenter and the surface was broken, the vibration from the rebound of silicone where the strain gage was located

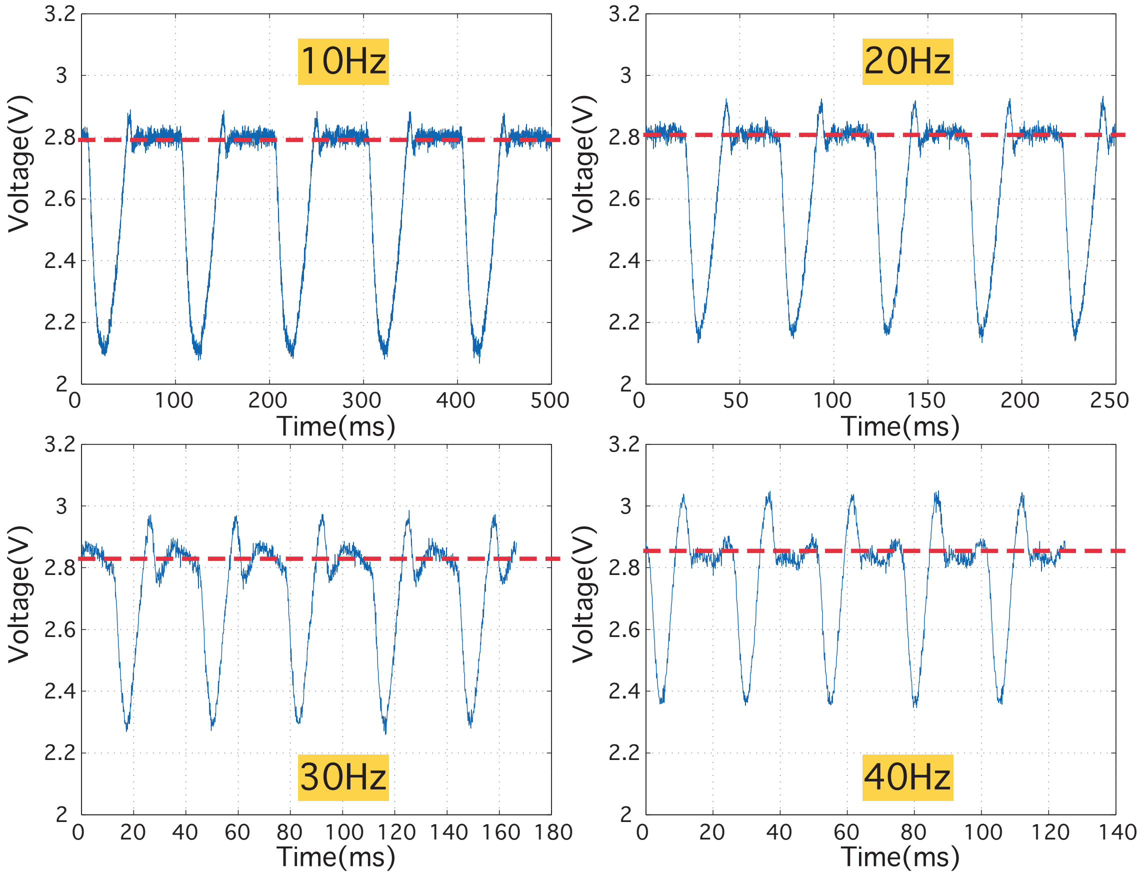

Figure 4.17: Measured signals from the strain gage at the frequencies of dynamic stimuli at 10 Hz, 20 Hz, 30 Hz and 40 Hz

showed frequencies that were consistent in pattern but different in magnitude.

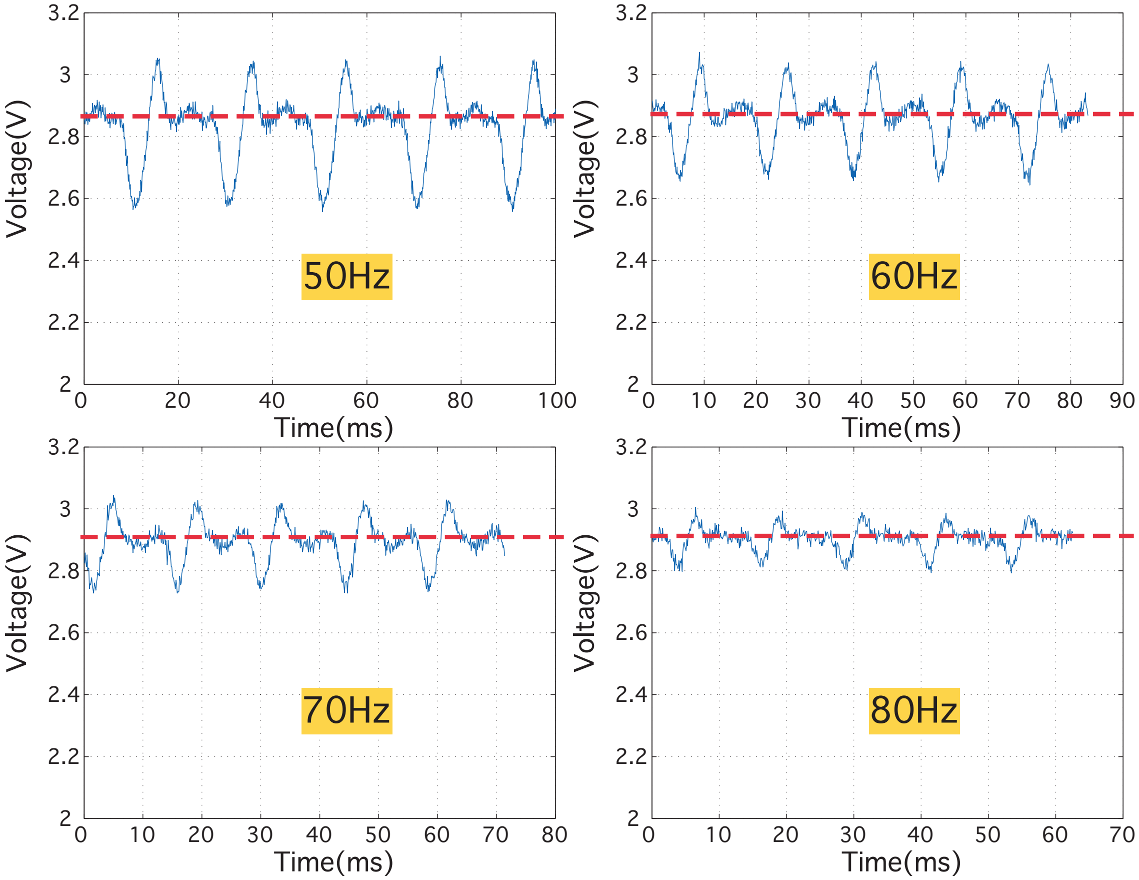

Figure 4.18: Measured signals from the strain gage at the frequencies of dynamic stimuli at 50 Hz, 60 Hz, 70 Hz and 80 Hz

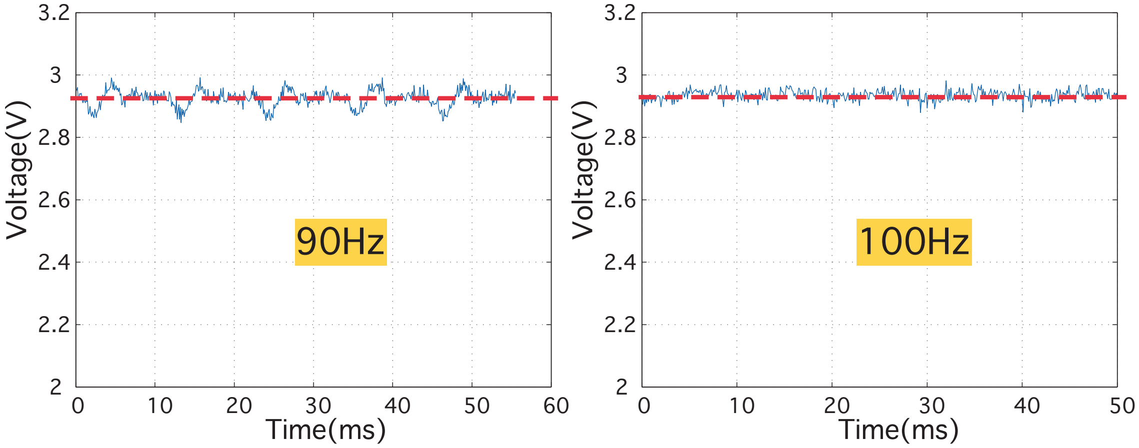

Figure 4.19: Measured signals from the strain gage at the frequencies of dynamic stimuli at 90 Hz and 100 Hz

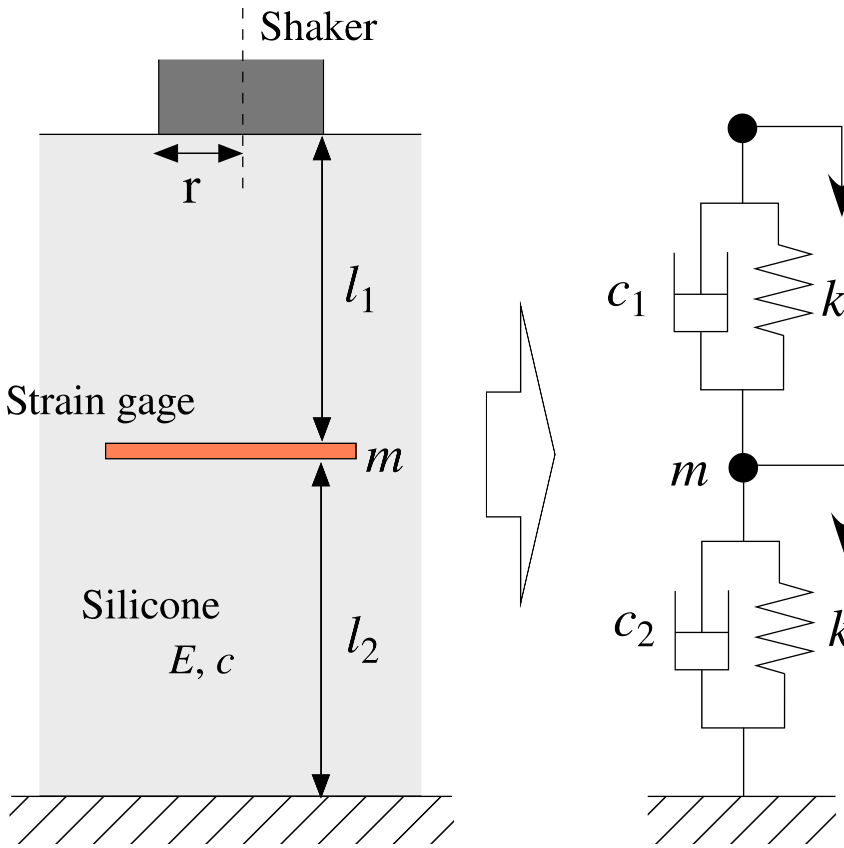

Figure 4.20: A proposed model of the silicone skin and strain gage

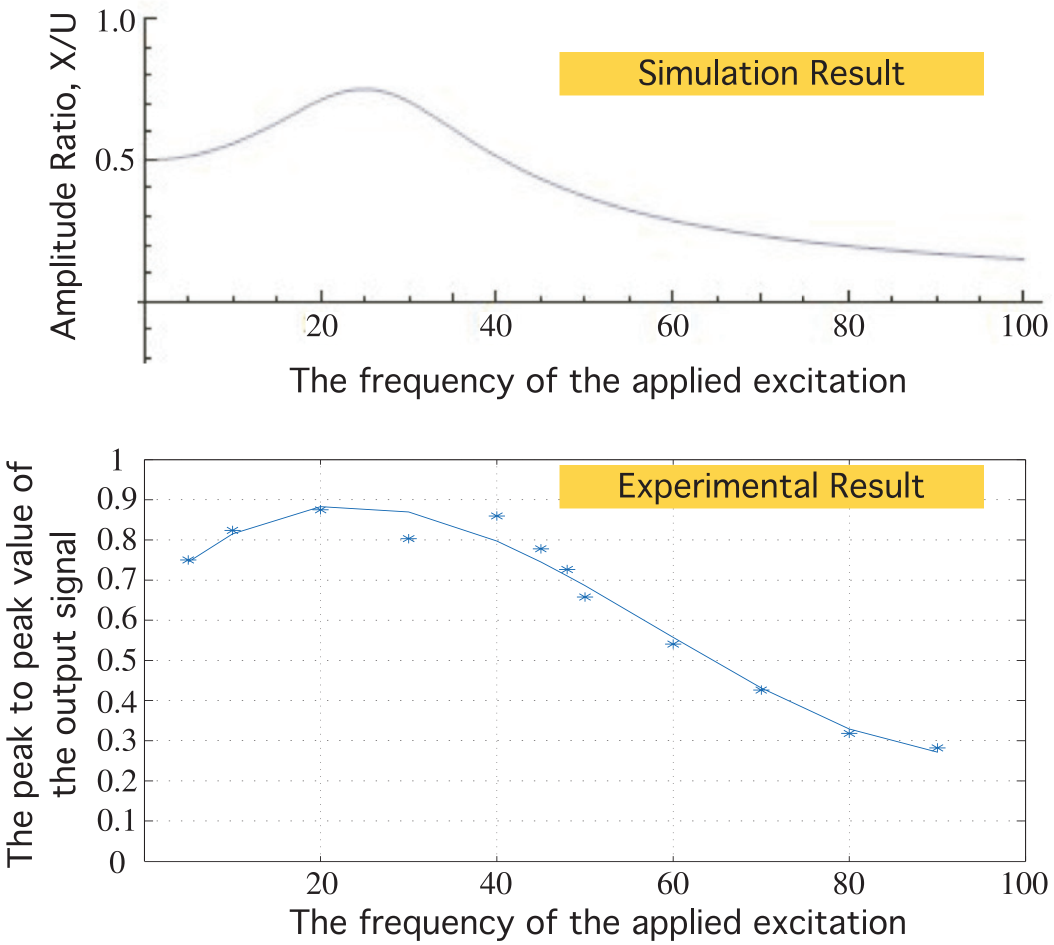

Figure 4.21: Frequency response plots: (a, *top plot*) simulation result of frequency response based on the proposed theoretical modeling in Fig. 4.20; and (b, *bottom plot*) experimental results of frequency response with a shaker applying dynamic stimuli of frequencies ranging from 5 Hz to 90 Hz.

4.3 Simulation

Fig. 4.20 illustrates a dynamic model of the artificial skin where E is the Young's modulus, c is the damping coefficient of the silicone, m is the mass of the strain gage, l_1 is the distance from the strain gage to the surface of the silicone, l_2 is the distance from the strain gage to the bottom of the silicone, and r is the radius of the shaker's surface, respectively. This configuration is converted to the mass-damper-spring system. The equation of motion of the mass-damper-spring system, as shown in Fig. 4.20, is given by

$$X(s) \quad = \quad G(s)\,U(s) \tag{4.5}$$

where $G(s) = (k_1 + c_1 s)/k_1 + k_2 + (c_1 + c_2)s + ms^2$, k_1 and k_2 are spring constants, c_1 and c_2 are damping coefficients of dampers, and m is the mass, $U(s)$ and $X(s)$ are the displacements of the input and the output in the frequency domain. We note that the parameters of the mass-damper-spring system can be obtained by

$$k_1 = \frac{\pi r^2}{l_1}E,\ c_1 = \frac{\pi r^2}{l_1}c,\ k_2 = \frac{\pi r^2}{l_2}E,\ c_2 = \frac{\pi r^2}{l_2}c$$

based on the experimental configuration and parameters shown in Figure 4.20. By assuming the input $u(t)$ of the vibration excitation and the output $x(t)$ in the steady state are as follows

$$u(t) \quad = \quad U_0 \sin(2\pi f t) \tag{4.6}$$

$$x(t) \quad = \quad X_0 \sin(2\pi f t + \phi) \tag{4.7}$$

we can calculate the ratio of magnitudes as

$$\frac{X_0}{U_0} = |G(i\omega)| \tag{4.8}$$

Fig. 4.21 shows the relationship between the frequency of the input $f = \omega/2\pi$ and the magnitude ratio X_0/U_0, where we use $E = 20.9 \times 10^3$ N/m^2, $c = 1.10 \times 10^2$ Ns/m^2, $l_1 = l_2 = 10$ mm, $m = 10$ g and $r = 5$ mm.

4.4 Discussions

4.4.1 Static loading

It was found that the vertically oriented strain gage produces more consistent results when subject to static loading, as presented in Section 4.2.3, which is consistent with the FEM results well. There is a small amount of drift in sensor signals due to the increase in temperature of the resistive foil gage. However, with careful arrangement, such drift can be minimized so as not to affect the experimental measurements. The repeated loading/unloading show consistent values measured by the gages, as illustrated in Fig. 4.13. The relative order of magnitude also matches with the expected values.

When the experiments were conducted repeatedly for many cycles, the strain gages may start to delaminate. Such delamination and detachment will cause inconsistency in the signals measured by strain gages. Due to the stiffness mismatch of the strain gages and the silicone material (usually the silicone is more compliant), relative motion can occur with such delamination.

4.4.2 Dynamic stimuli

When dynamic stimuli with a range of frequencies from 5 to 100 Hz were applied, the resulting amplitudes of penetration to the silicone skin were detected by the embedded sensors. Fig. 4.21 plots the experimental results of frequency response. The results follow the frequency response of a typical second-order system with a rising peak near the natural frequency at approximately $\omega_n = 20 \sim 40$ Hz. Based on the response, the apparent damping ratio is about 0.3. The cut-off frequency is approximately 60 Hz.

The dynamic model and simulation show that the results are similar to those of experiments, with the parameters used for simulation. Such simulation suggests a working dynamic model for predicting the frequency response subject to dynamic loading, and can be used as a reference for the design and fabrication of artificial skin sensors.

It is intriguing to note that the peaks above the red centerline in Fig. 4.18 are larger at 40Hz to 60 Hz. This suggests that the resonance of the artificial skin may lie within this range because when contact was broken the material bounced back with higher level of amplitudes. Comparing this with the plot of the frequency response, we postulate that the resonance of the artificial skin may be in the neighborhood of 40 Hz. Such resonance can be exploited for the purpose of increased sensitivity in the design of bio-inspired sensors and in the experiments with data acquisition for analysis. Further investigation will be conducted in this area.

4.5 CONCLUSIONS

This Chapter presented experimental studies of silicone artificial skin sensors under both static loading and dynamic stimuli with a frequency range from 5 to 100 Hz. Theoretical modeling and simulation using FEM were also conducted to compare with the experimental results. We found that the vertical configuration of the strain gage produces more consistent strain measurement, and is more intuitive when compared with FEM simulation. The frequency responses of dynamic loadings were measured experimentally. The results of dynamic frequency response match well with a proposed dynamic model with simulation. Based on the estimate of natural frequencies of the skin, we can exploit the increased amplitude of vibration response to increase the sensitivity of the sensor design. Based on the postulated mechanism of static and dynamic excitations, skin sensors can be designed and fabricated for effective and efficient detection and measurement of various external stimuli.

Chapter 5

An Experimental Study of the Strain Creep Responses of an Artificial Skin with Tactile Sensor

In this chapter, experiments were conducted to observe and study the strain creep responses using a bio-inspired artificial skin sensor consisting of silicone and embedded strain gages. It was found that the skin sensor showed strain creep when the embedded strain gage was subject to force control; that is, by regulating the force applied at the contact surface. Type I and Type II creep responses were observed when external stimuli were applied under force control; just as the Type I and II stress relaxations were observed when external stimuli were applied under position control. The characteristics of strain creep is consistent with the energy principle. This experimental study provides us with more insights into viscoelastic contact interface and tactile sensing, such as that in human and/or artificial skin, regarding the temporal responses, strain creep and stress relaxation. It was also found in this study that the latency model can indeed be employed to explain the creep responses under force control in viscoelastic interface, just as it can explain the physical behavior of stress relaxation under position control. Although stress relaxation and strain creep are two sides of the same coin, capturing the same physics of materials behavior, there are, however, apparent differences in the fingerprints of signals based on their frequency ranges. This observation may pave a road to the intelligent detection and diagnosis of tactile sensing and sensor design by exploiting the nature of viscoelastic responses in biomedical materials and contact interface.

5.1 INTRODUCTION

Tactile sensing is indispensable to safe human-machine interface and dextrous manipulation. Generally, a tactile sensor consists of sensing elements, such as piezoresistive or piezoelectric material, and soft material, such as silicone rubber, which encloses the sensing elements for protection from mechanical and chemical damage. Most soft materials are viscoelastic materials which have two important phenomena: (1) *stress relaxation*, and (2) *strain creep*. The stress relaxation describes a change in force, as a function of time, while displacement is kept constant under position control; whereas, the strain creep elucidates a temporal change in displacement while force is kept constant under force control. As a result, the reading from the sensing elements is affected by the viscoelastic phenomena. Therefore, understanding the phenomena is necessary to accurately estimate the external stimuli and temporal change applied to the tactile sensor. In this Chapter, external stimuli, through the application of constant force (akin to force control) via dead weights, are applied to an artificial skin sensor consisting of silicone and embedded strain gages. Strain creep responses were observed based on the reading of the strain gages. In addition, the simulation by using the latency model is conducted to explain the behavior of strain creep.

5.1.1 Literature review

Research studies have been conducted on the dynamic behavior of viscoelastic materials, especially the stress wave propagation. Theocaris and Papadopoulou studied the propagation of stress waves in viscoelastic media based on the Kelvin-Voigt model [39]. Turhan and Mengi proposed three types of inhomogeneities of the stress wave within the viscoelastic media [40]. Stucky and Lord utilized the finite element modeling method (FEM) to analyze the properties of ultrasonic waves in linear viscoelastic media [41]. Pereira, Mansour and Davis employed a wave propagation technique to measure the dynamic viscoelastic properties of excised skin when subjected to a low incremental strain [42]. Fowles and Williams derived two different phase velocities from conservation relations, mass and energy [43]. The study of viscoelasticity has benefited from different perspectives over the decades. The Maxwell model and the Kelvin-Voigt model are the first models used to describe the behavior of viscoelasticity [44]. After that, the generalized Maxwell model was proposed and has been widely used in the modeling of linear viscoelasticity. Sakamoto *et. al* applied the modified spring-damper model to the grasping analysis of viscoelastic materials [45]. Many other studies of viscoelastic behaviors were presented in [46, 47, 48, 49, 50, 51, 52, 53]. Research of viscoelasticity also has been done from the rheology viewpoint [54, 55, 56]. Golik proposed a model based on the diffusion of holes inside rubber under an external force [57]. Contrary to the Maxwell model which uses linear springs and dampers, Fung proposed an empirical model that separates elastic and temporal responses [6]. Tiezzi and Kao adopted Fung's approach to model the soft contact interface [58, 59, 60, 61, 29, 62, 63]. The consistency of the parameters in Fung's model has been illustrated [64]. Tsai and Kao proposed the *latency model* which postulates that the stress relaxation can be considered as a result of uneven strain distribution, as well as dynamic re-distribution, before the material reaches a new equilibrium state [65]. Furthermore, Tsai and Kao utilized the latency model to explain the responses under different loading rates of external force [66], in which different responses are shown to be a result of different loading rates due to the temporal effect of viscoelasticity.

5.1.2 Stress Relaxation and Strain Creep

Two types of stress relaxations are defined in [65] as shown in Fig. 5.1(a). One is the Type I stress relaxation, exhibiting decreasing stress under a constant displacement, at the end of loading. The other is the Type II stress relaxation with increasing stress under a constant displacement, at the end of unloading.

Similarly, two types of strain creeps are defined in [67] as shown in Fig. 5.1(b). One is the Type I strain creep, exhibiting increasing displacement under a constant force, at the end of loading. The other is the Type II strain creep with decreasing displacement under a constant force, at the end of unloading.

5.2 Theoretical Background

Based on the experimental observation and the fundamental concept in physics, we postulate the following two aspects of viscoelastic contact behaviors.

(1) The two viscoelastic phenomena, stress relaxation and strain creep, are caused by unbalanced strain states within the material subject to transition of external stimuli. Such response in some literature was referred to as hole displacement, especially in polymeric materials [57]. The velocity of strain propagation inside the material determines the time constants of exponential decay or growth for stress relaxation or strain creep.

(2) The material, given enough time for dynamic re-distribution of strain, will always approach the equilibrium state at which internal strain is uniform, internal stress is balanced, and stress propagation ceases. This state is called the equilibrium state.

The rate of strain propagation is determined by the nonlinear latency model [68] proposed by Tsai and Kao, shown in Fig. 5.2 and the following differential equation in Eq. (5.1)

$$\dot{\varepsilon} = \begin{cases} -\nu(\varepsilon - \varepsilon_e)^n & \text{if } n \text{ is odd} \\ -[\operatorname{sgn}(\varepsilon - \varepsilon_e)]\nu(\varepsilon - \varepsilon_e)^n & \text{if } n \text{ is even} \end{cases} \tag{5.1}$$

where ε_e is the equilibrium strain, ν and n are constants of the empirical polynomial function, and ε is the instantaneous strain at any point within the material at any time. Eq. (5.1) shows that the magnitude of strain rate can be determined by the current strain, ε, and the equilibrium strain, ε_e. In other words, if the current strain is further away from the equilibrium strain, a larger magnitude of strain rate should be expected. In this Chapter, we adopt odd exponents in equation (5.1) for the convenience in analysis. With n being odd, we can

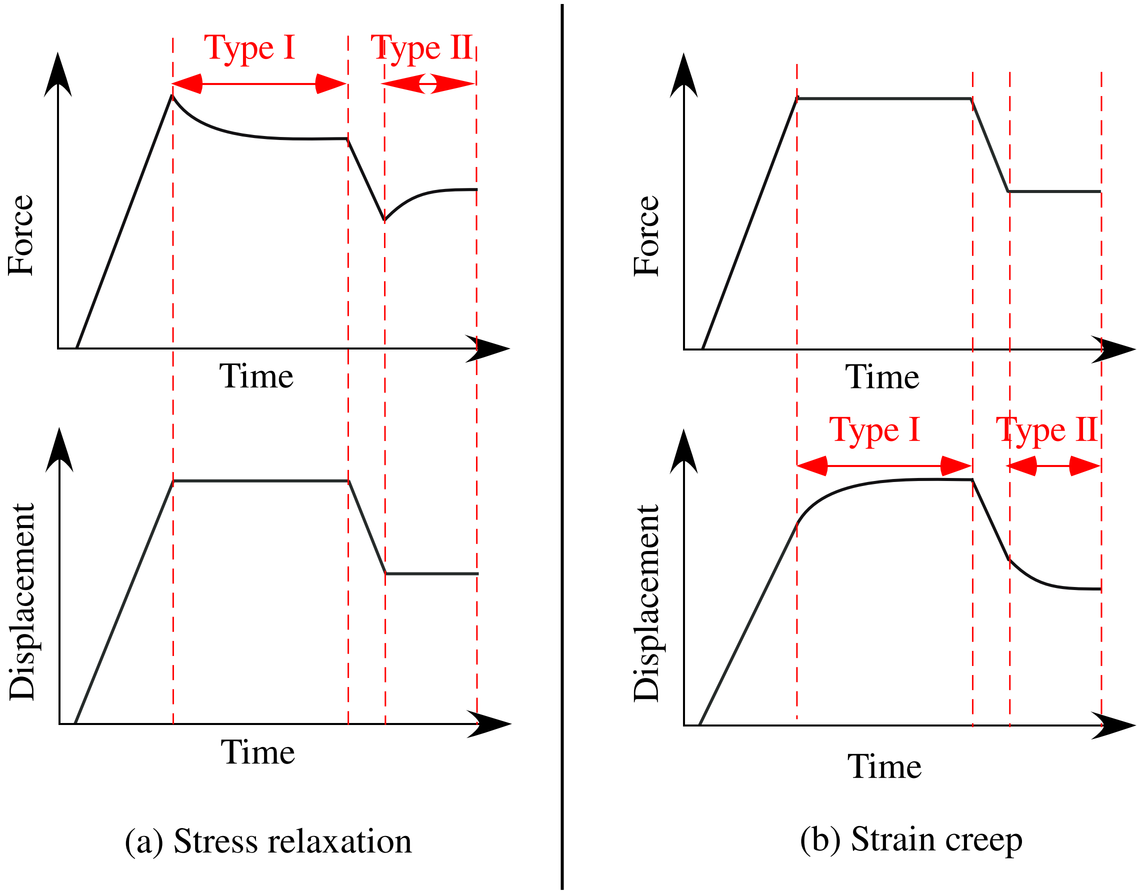

(a) Stress relaxation

(b) Strain creep

Figure 5.1: The overview of strain relaxation and stress creep

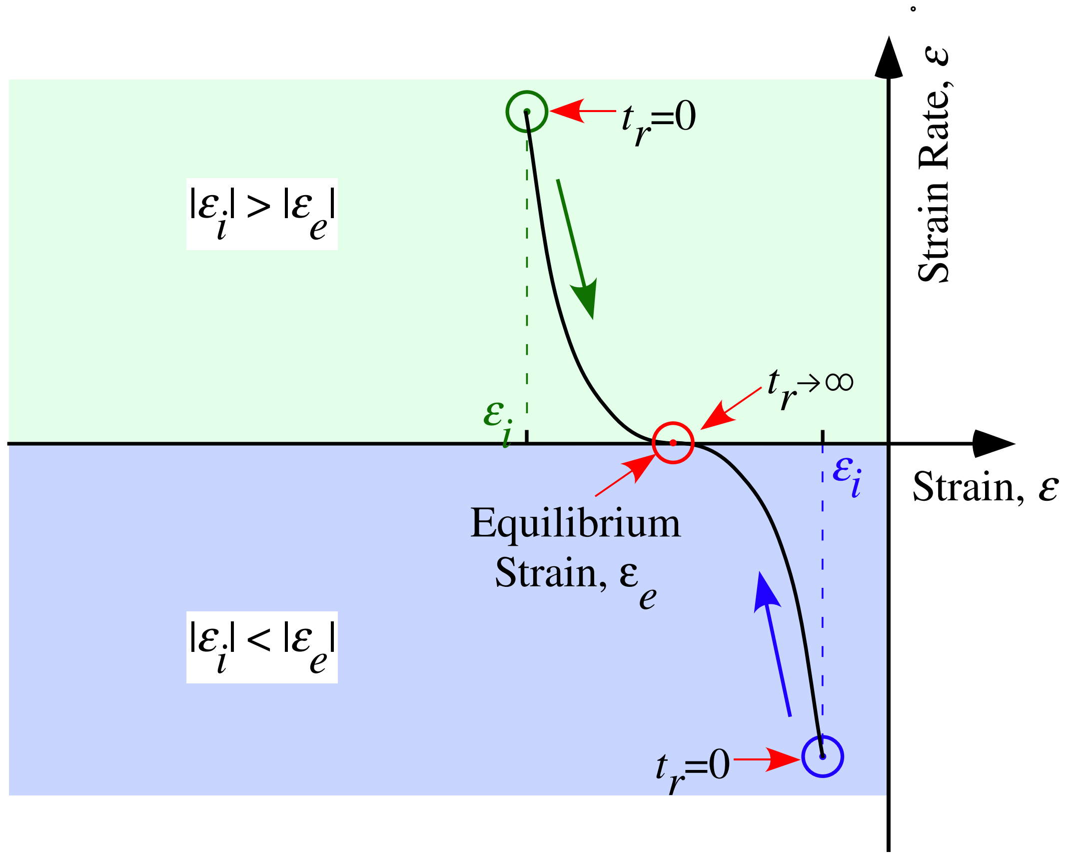

Figure 5.2: The nonlinear latency model

re-write Eq. (5.1) as follows

$$\dot{\varepsilon} = -\nu(\varepsilon - \varepsilon_e)^n \tag{5.2}$$

The strain creep is also explained by this latency model shown in Figs. 5.3 and 5.4. After the end of loading, the exterior parts of the material is closer to the new equilibrium strain, ε_e, than the inner parts of the material. The inner parts of material can approach the new equilibrium strain, ε_e, via dynamic strain redistribution, resulting in the temporal responses of strain creep.

The total strain at the end of loading stage gradually increases because the new equilibrium strain, ε_e, is greater than the previous equilibrium strain. On the other hand, at the end of unloading, the strain propagation causes the total strain to gradually decrease. This is because the new equilibrium strain, ε_e, is smaller than the previous equilibrium strain.

5.3 EXPERIMENTAL STUDY

Static weights are employed to apply constant forces (akin to a force control system). The displacement/strain is measured by the strain gage embedded in the sensor. The experimental setup and procedures are explained in the following sections.

5.3.1 Experimental Setup

An artificial skin sensor fabricated in Chapter 4 and the same data acquisition system is used. Fig. 5.5(a) shows the jig, a custom made tool used to control the location and motion, which applies constant forces. The indenter is set directly above the artificial skin, in which the strain gages are embedded, to apply the constant force via dead weights. The static weight I is fixed to the indenter by the screw shown in Fig. 5.5(c). The entire weight is applied to the skin sensor when the static weight I is positioned directly above the top plate surface with a gap. A plastic plate and the static weight II are placed on top of the static weight I, as shown in Fig. 5.5(b), to change the total force applied on the skin. The

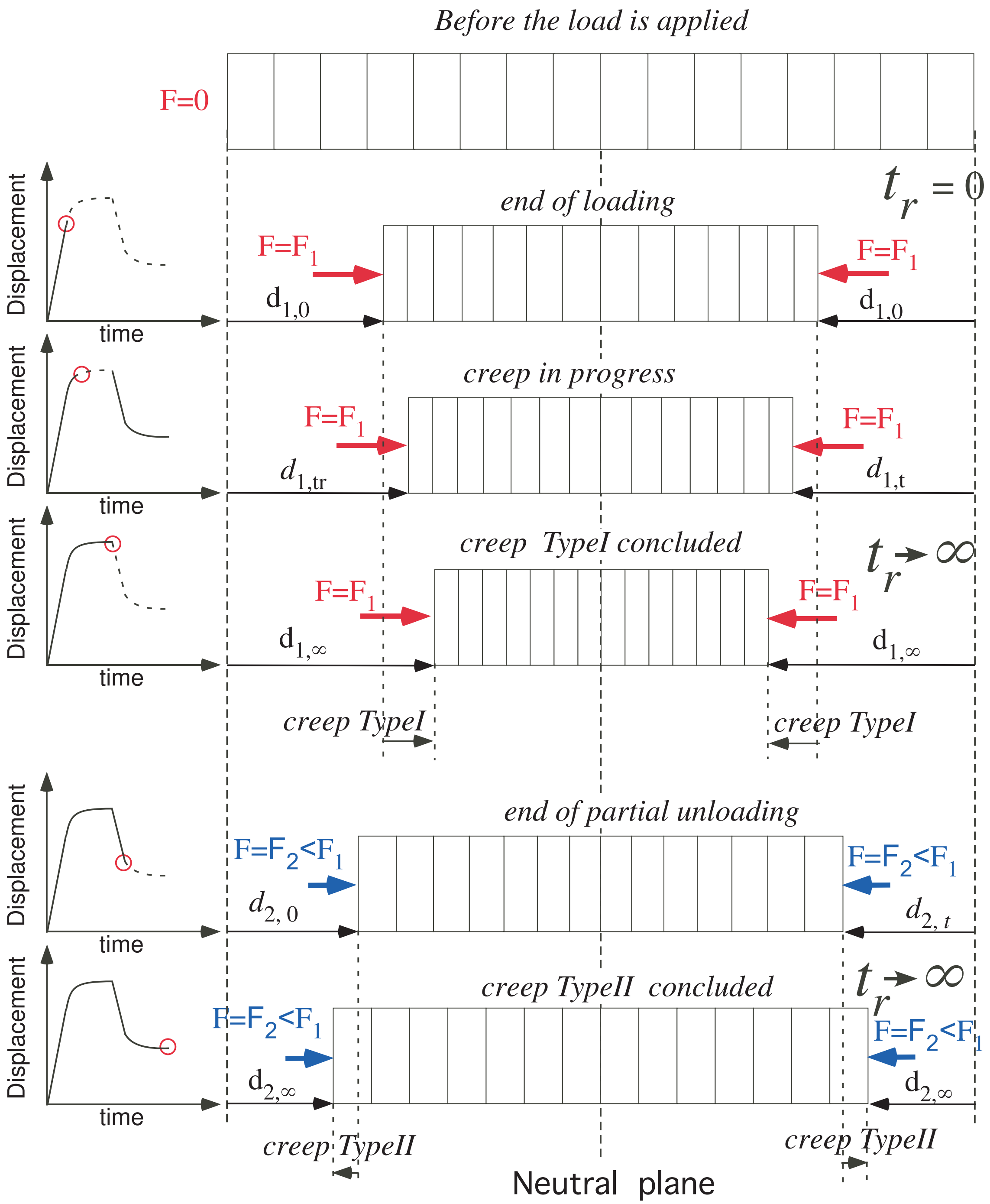

Figure 5.3: The latency model for creep responses: **Loading:** The first subplot represents the even density distribution before the external load is applied. The second subplot is the transient state when the external force is applied, with force held at constant ($t_r = 0$). The strain creep phase after that is shown in subplots 3 and 4 when equilibrium is established ($t_r \rightarrow \infty$). The total *Type I* strain creep is indicated. **Unloading:** The force is *partially* decreased which causes Type II strain creep, as shown in subplots 5 and 6. **All:** The forces and their magnitudes are indicated with arrows of different lengths corresponding to their magnitudes. The force-time plots to the left of the figure indicate the state of the latency model with a circle.

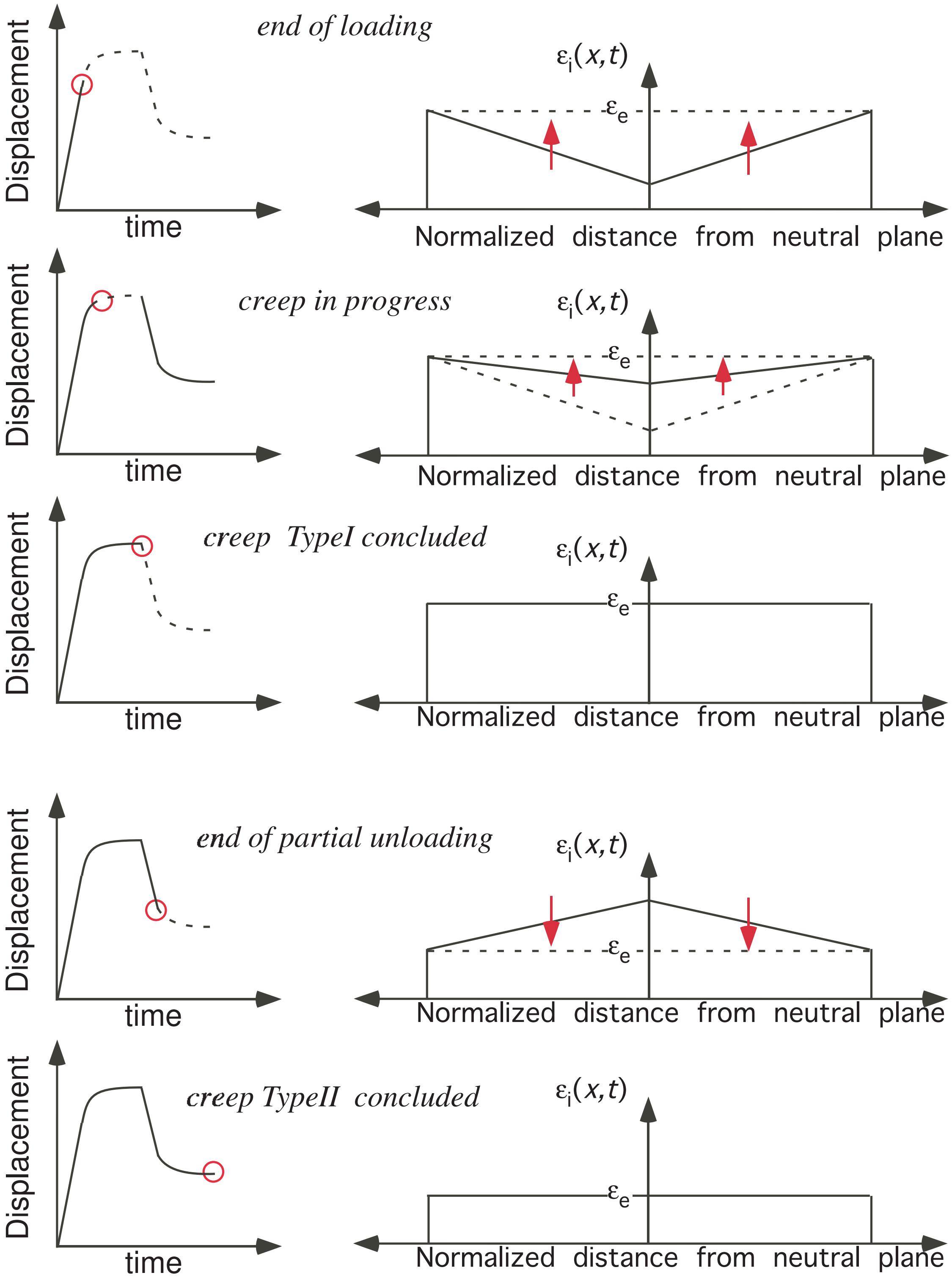

Figure 5.4: Illustration of strain re-distribution during strain creep

plastic plate is used to quickly remove the static weight II without touching the remaining parts of the jig.

5.3.2 Procedures of Experiments

(1) Fix the static weight I to the indenter and maintain a gap between the top plate surface when the entire weight is rested and applied on the skin specimen.

(2) Position the jig such that the indenter will press upon the predetermined location on the skin.

(3) Set the initial output signal from the amplifying circuit, V_{o}_ini, such that the output signal V_o does not saturate when the entire weight is added by adjusting the potentiometer shown in Fig. 4.10.

(4) Lower the indenter to barely touch the surface of the skin sensor.

(5) Release the indenter to press upon the surface of the skin senor, as shown in Fig. 5.5(a). This is the loading phase of the experiment.

(6) Remove the plastic plate and the static weight II, as shown in Fig. 5.5(c). This corresponds to the phase of partial unloading.

(7) Return the plastic plate and the static weight II. This is the re-loading phase.

(8) Repeat steps 6 $\sim$ 7 several times.

(9) Remove the plastic plate and the static weight II.

(10) Lift the static weight I and the indenter.

5.3.3 Experimental Results and Analysis

Fig. 5.6 shows the result when the strain gage is subject to tension. The strain ε shown in vertical axis is calculated by Eq. (4.4). The indenter is not touching the skin

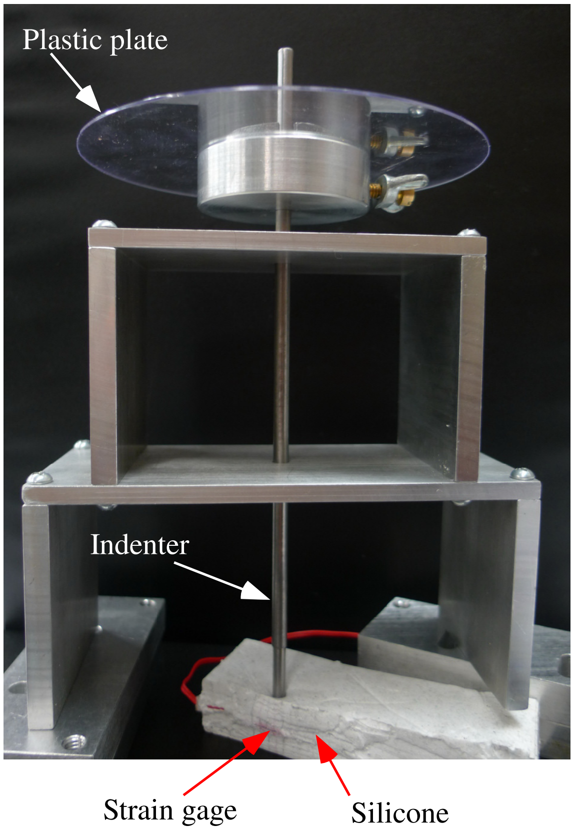

(a) The overview of the jig which apply the constant force by dead weights

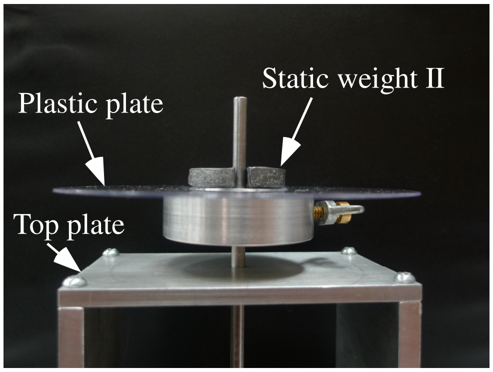

(b) The total weight (180g)

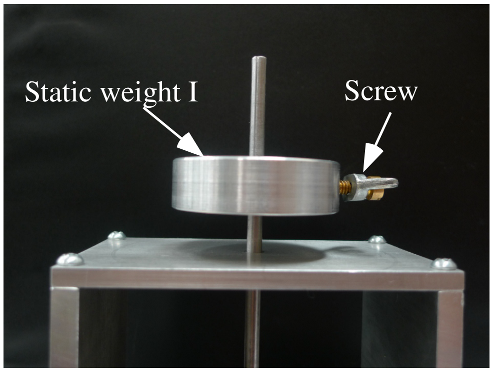

(c) The partial weight (115g)

Figure 5.5: The jig which applies adjustable constant forces

sensor at t=0s and the strain of the skin senor is zero so the output signal from the amplifier, V_o, at this moment is set to the V_{o_ini} in Eq. (4.4). At t= 3s, the entire weight is released to press upon the skin sensor (Step 5 in the procedures). This step is the loading phase and the strain is increased which means the strain gage is subject to tension. After the strain reaches the new equilibrium at t=8s, the partial weight II is removed (Step 6 in the procedures). Again, after the strain reaches the new equilibrium at t=13s, the partial weight II is put back (Step 7 in the procedures). The removing and returning of the partial weight in steps 6 $\sim$ 7 is repeated till t=62s. After that, the entire weight is removed. The result of the time period from 14s to 26s is enlarged in Fig. 5.8(a).

The results show the behavior of Type I and Type II strain creep responses. For instance, the partial weight II is added at t=20s, resulting in the strain to linearly increase initially. After that, the strain gradually increases until t=24s, although additional dead weight has not been added. This is the Type I strain creep. At t=17s, the partial weight II is removed, causing the strain to linearly decrease. After that, the strain gradually decreases until t=20s, although additional static weight has not been removed. This is Type II strain creep. The difference between the Type I and Type II strain creep responses is:

- Type I strain creep takes place after loading
- Type II strain creep takes place after partial unloading

This definition of Type I and II is consistent with those defined in the stress relaxation.

The same experiments are conducted after flipping over the skin sensor, with results shown in Fig. 5.7 and Fig. 5.8(b). At t= 50s, the entire weight is released to press upon the skin sensor (Step 5 in the procedures). This step is the loading phase and the strain decreases, indicating that the strain gage is subject to compression. The results also show the Type I and Type II strain creep responses, just like the previous experiments when the strain gage is subject to tension.

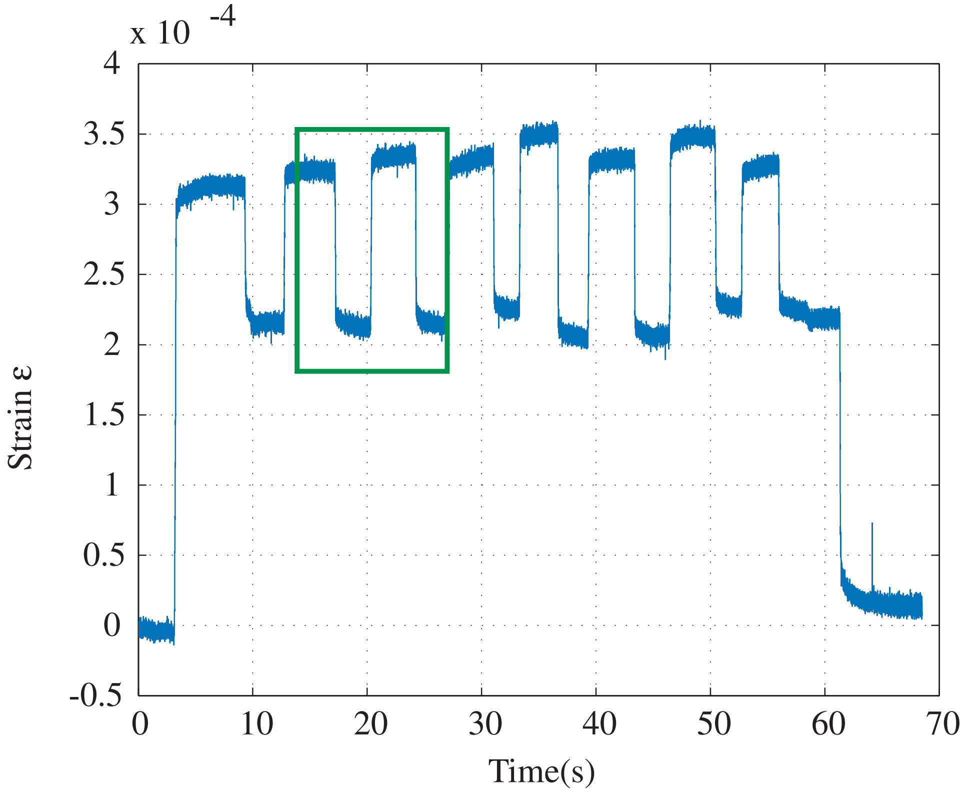

Figure 5.6: The strain creep response when the strain gage is under tension

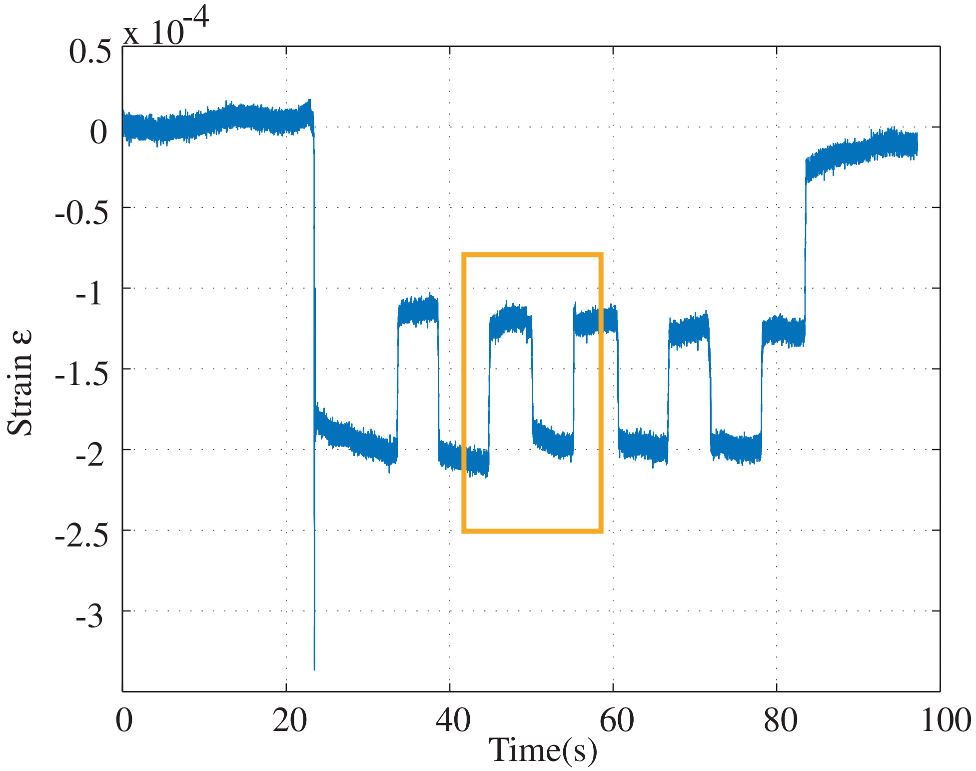

Figure 5.7: The strain creep response when the strain gage is under compression

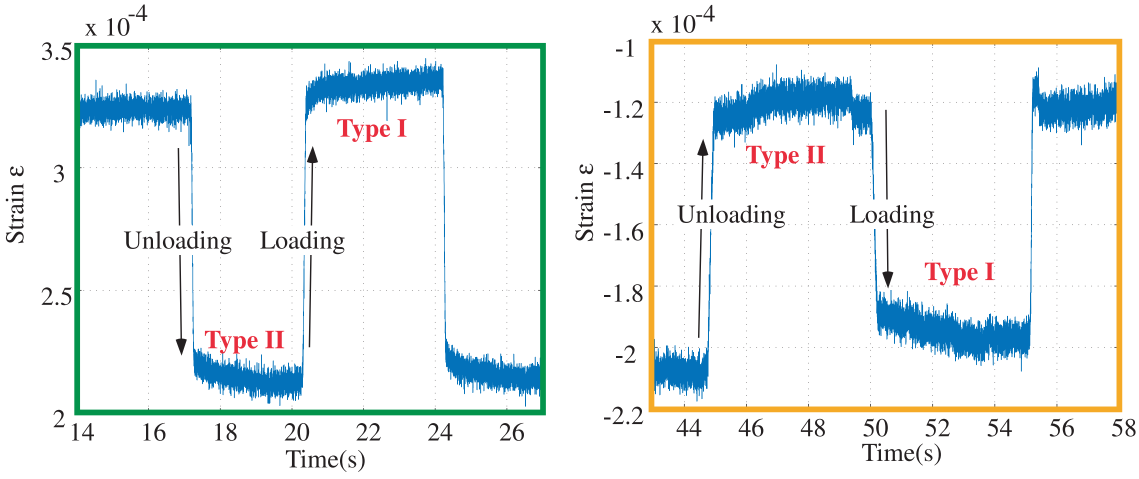

(a) (b)

Figure 5.8: Enlargement of parts of Fig. 5.6 and Fig. 5.7

The shapes of the Type I and Type II strain creep responses appear to be opposite to each other when the strain gage is subject to tension or compression. This is because the strain changes into the opposite directions during loading and unloading. To clarify the results, we can say that in strain creep the magnitude of the strain gradually increases after loading and decreases after unloading. In other words, the direction of strain creep is the same as the direction of the preceding loading or unloading.

The results make sense from the viewpoint of potential energy, as illustrated in Fig. 5.10. Fig. 5.10(a) is associated with the experimental results. The clockwise loop in the small loop means energy is dissipated during the repeating loading and unloading. This is consistent with the behavior of physical systems. Usually, energy is dissipated into heat. On the other hand, if the directions of Type I and Type II strain creep are opposite, as shown in Fig. 5.10(b), the loop becomes counterclockwise which means energy is created. This violates the principle of physics.

5.4 SIMULATION

Based on the model presented in Eq. (5.1), MATLAB is used to simulate the strain creep response for the evolution of displacement subject to force control. The procedures of simulation and results are presented in the following subsections.

5.4.1 Simulation Procedures

(1) The strain distribution immediately after loading or unloading is not uniform, but follows the pattern illustrated in Fig. 5.4. When time approaches infinity, the strain will become uniformly distributed, and the strain will approach the equilibrium strain asymptotically.

(2) The material is divided into several elements axially, as illustrated in Fig. 5.3.

(3) Arrange the initial strain of each element, as illustrated in Fig. 5.4. At this time,

the strain of the external element is assumed to be equal to the equilibrium strain ε_e.

(4) Determine a time period and calculate the strain rate $\dot{\varepsilon}$ using Eq. (5.2). Next, update the strain ε for each element.

(5) Calculate the displacement of each element, and the total displacement is the sum of the displacement of all elements.

(6) Repeat 4 and 5 until all element reach the equilibrium strain ε_e.

5.4.2 Simulation Results

Fig. 5.9 shows the results of simulation based on the model presented in Eq. (5.2), corresponding to the experimental results in Fig. 5.8. The procedures of simulation are described in the previous section. It can be seen from the results that the trend of Type I and Type II strain creep in simulation is similar to that of the experimental results.

5.5 DISCUSSIONS

The shapes of stress relaxation and strain creep may look similar; however, one significant difference is the direction of the strain change (increasing or decreasing). The direction of strain creep is the same as the preceding loading or unloading. On the other hand, the direction of stress relaxation is opposite to the preceding loading or unloading. The change of direction in stress relaxation very likely will produce high frequency signals due to the change of the direction of signals. This will be the fingerprint of stress relaxation. On the other hand, the strain creep follows the same direction of strain in loading or unloading which does not generate such fingerprint of high frequency signals.

Human skins (epidermis and dermis) have fast adaptive and slow adaptive sensors. Possibly, the fast adaptive sensors are detecting such high frequency fingerprint; whereas, the slow adaptive sensors may be detecting the gradual increase or decrease after loading or

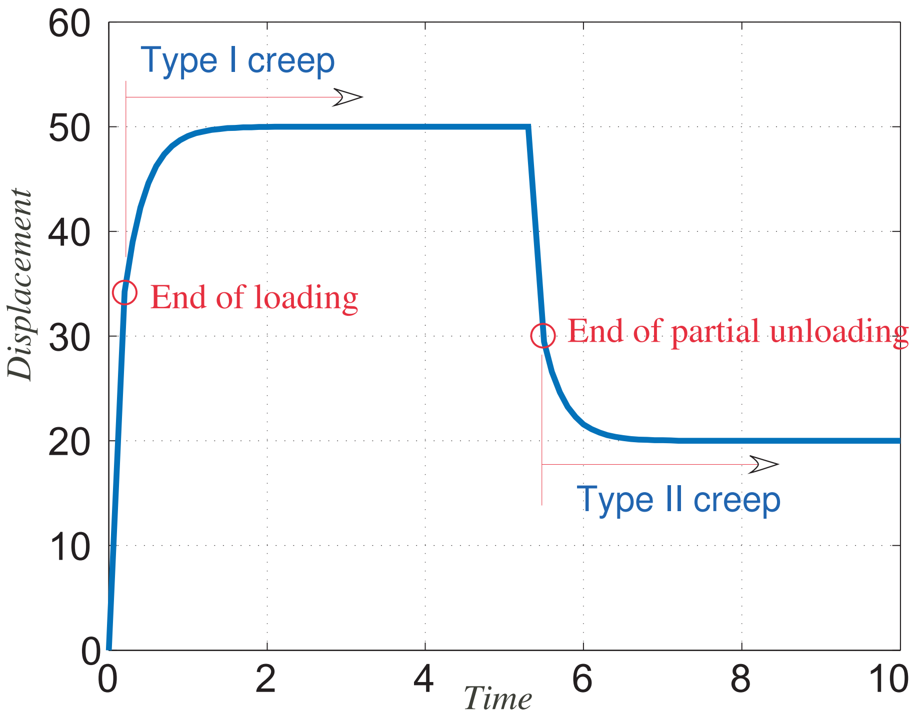

Figure 5.9: Results of simulation showing: (left) the end of loading, followed by Type I creep, and (right) the end of partial unloading, followed by Type II creep response.

unloading. The artificial skin sensor shows that the strain creep can finish in a few seconds. Human skin is capable of detecting a touch as a beginning but the sensation will gradually attenuate in a few seconds. This can be extrapolated to suggest that human skin is utilizing the temporal responses, stress relaxation or strain creep, to detect and/or distinguish a touch. More study is needed in this area in order to ascertain if this indeed is one mechanism of tactile sensing in humans.

In this Chapter, we presented the experimental study and simulation of strain creep. It was found that the latency model can indeed be employed to explain the creep responses under force control, just as it can explain the physical behavior of stress relaxation under position control. This makes intuitive sense because stress relaxation and strain creep are two sides of the same coin, representing the same physics of materials behavior. There are, however, apparent differences in the fingerprints of signals based on their frequency ranges. This may open an avenue to the intelligent detection and diagnosis of tactile sensing and sensor design by exploiting the viscoelastic nature of biomedical materials.

5.6 CONCLUSIONS

Type I and Type II strain creep responses are experimentally observed in artificial skin sensor when constant forces are controlled by applying static weights. Although the mechanism regarding how strain is propagated within the skin sensor material is much more complicated than the uniaxial compression, which is the case in previous work [67], the artificial skin sensor showed similar strain creep. Furthermore, in this experiment, the strain creep is perceived when loading causes tension as well as compression. The increase or decrease of strain creep (Type I or II) is consistent with the energy principle. Based on the frequency response analysis of Type I or II stress relaxation versus strain creep, it may be inferred that human skins employ temporal responses of viscoelasticity for enhancing the capability of tactile sensing. This result can inspire design and analysis of tactile sensors in the future.

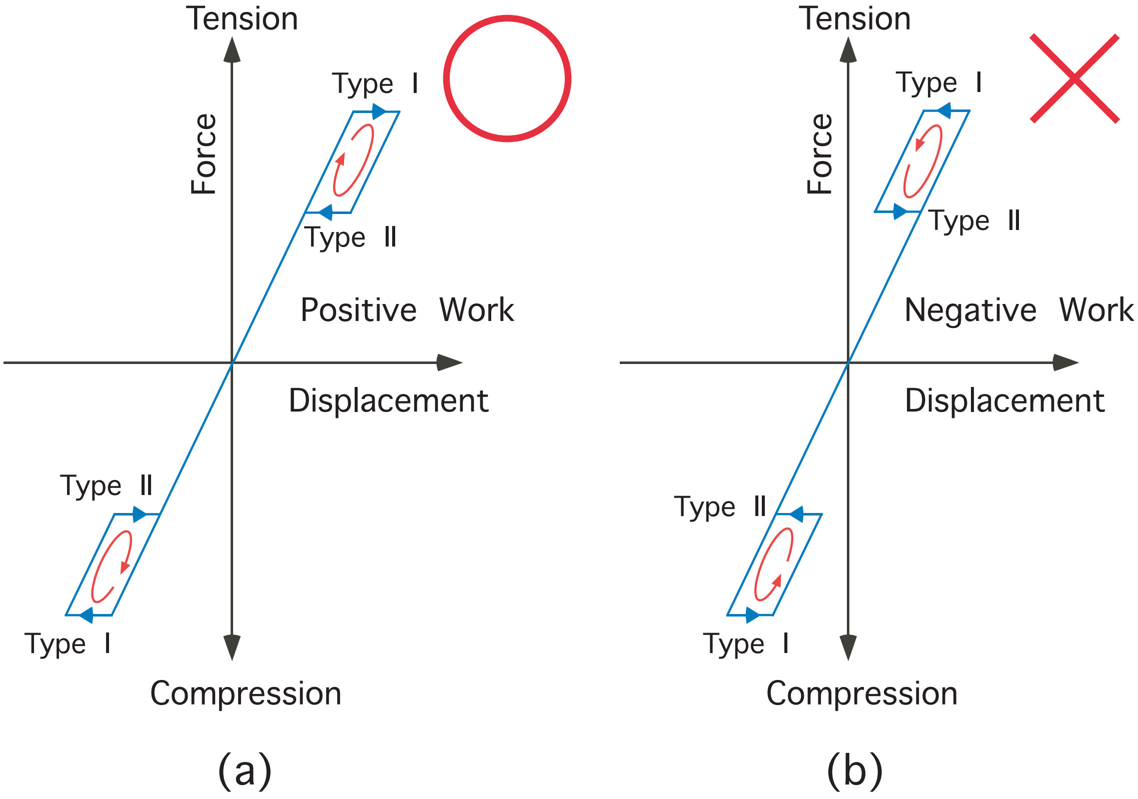

Figure 5.10: The directions of Type I and Type II strain creep

Chapter 6

Flexible and durable tactile sensors composed of carbon nanotubes (CNTs)

6.1 INTRODUCTION

A tactile sensor which is sensitive to small stimuli and durable to large stimuli, such as human skin, is necessary for the dexterous manipulations by robot hands. The sensitive range of a tactile sensor is limited and sensing all types of stimuli by only one sensing element is not realistic. For instance, human skin has four types of sensing elements which are called mechanoreceptors and each mechanoreceptor senses different types of stimuli. Human skin, especially on finger tips, is incredibly sensitive to small forces and durable under large forces. For examples, the fingertips are incredibly sensitive when tracing a surface with small force and can detect a step less than few micrometers and at the same time durable when strongly grasping an object though the sensitivity is decreased. The tactile sensors sensitive to a specific stimulus and durable to other stimuli are desirable for the artificial skin sensor which can be used in robot hands.

There are some strain (tactile) sensors sensitive to small strain (stimulus), such as semiconductor strain gages, but those are not durable to large strain. The strain gages are designed to measure the strain of hard materials, such as steel or concrete. Therefore, the strain is small and the strain gages are much softer than the hard materials, which results in accurate strain measurement. However, if a strain gage is used with a soft material, such as rubber, the strain gage cannot follow the strain of the soft material because strain gages are much harder than the soft materials, so the strain gage will delaminate from the soft material or change the strain distribution in the soft material. Therefore, strain gages are inappropriate for the large deformation with soft materials.

Carbon nanotubes (CNTs) was discovered by Iijima in 1991 and the applications of CNTs have been studied because of its unique properties. One of the interesting properties of CNTs is the piezoresistive effect which shows the change of electrical resistance depends on applied mechanical strain. In addition, CNTs are durable and flexible. Therefore, CNTs are an ideal candidate for the tactile sensing element which needs both high sensitivity and durability. Strain sensing by CNT/Polymer composite films is studied in [69, 70, 71, 72] and used for a sensor to detect slippage [73]. Schmitz *et al.* [74] sprayed a thin layer of conductive silicon and silicone/carbon-particles composite on the surface of a silicone foam to make an artificial fingertips.

In this Chapter, a prototype of tactile sensor based on CNTs is fabricated by spraying diluted CNTs on the surface of a soft material and preliminary tests for the sensitivity and durability are conducted.

6.2 Experiments

6.2.1 Fabrication of the tactile sensor based on CNTs

Diluted CNTs are sprayed by airbrush on the surface of the target soft material to make the thin CNT layer on the surface as shown in Fig. 6.1. The diluted CNTs were bought from Ohashi Kasuga Tsusyo Inc. In the diluted CNTs, multi-walled CNTs with a specific surface treatment are dispersed in water at 2 weight present. The more detailed specification of the CNTs provided by Ohashi Kasuga Tsusyo Inc. is shown in Fig. 6.2. After the spraying of the diluted CNTs, the solution (water) is air-dried.

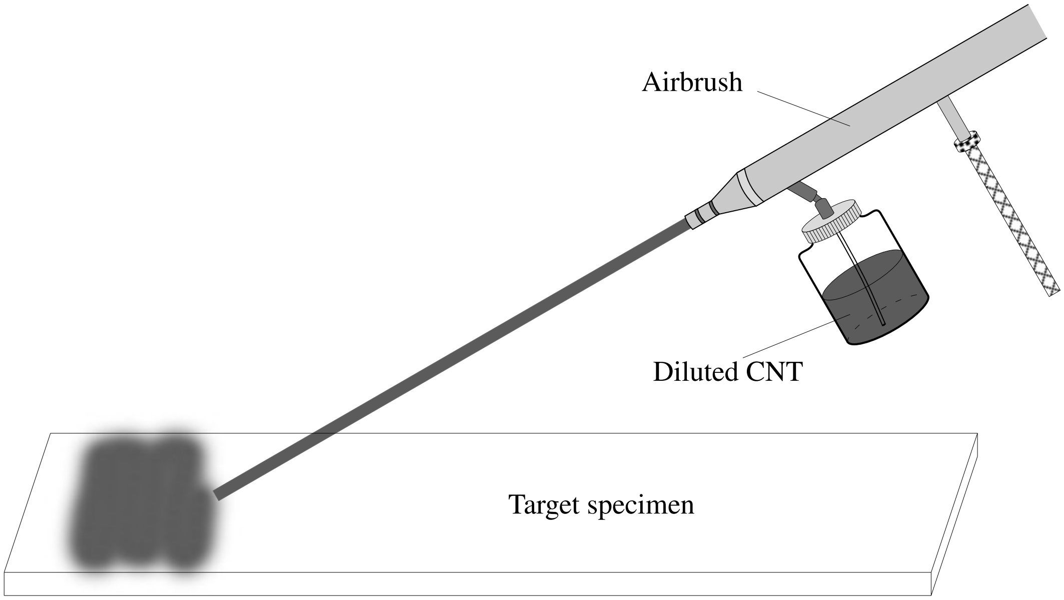

Figure 6.1: Spray diluted CNTs on the surface of a specimen by airbrush

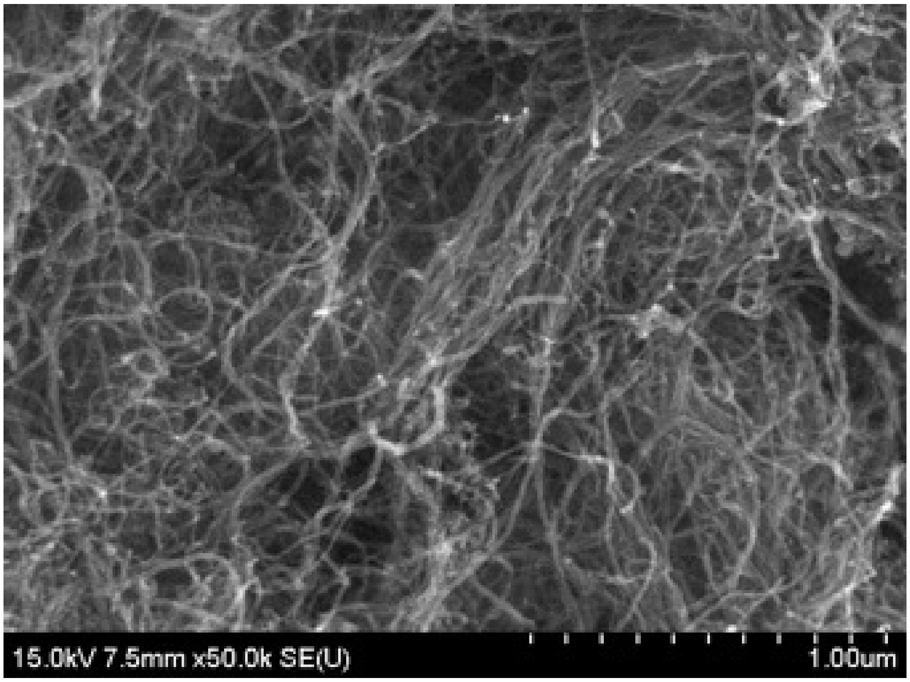

(a) SEM image x50k

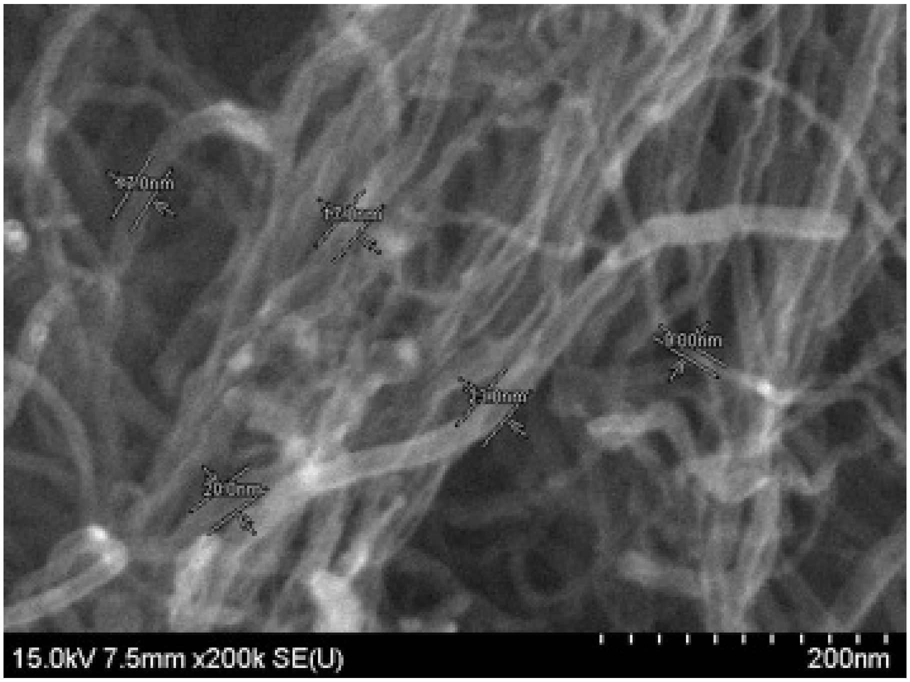

(b) SEM image x200k

Figure 6.2: The images captured by SEM (Scanning Electron Microscope). The external diameter is 5$\sim$30 (nm) and the length is 5 $\sim$ 30 (μm). (Provided by Ohashi Kasuga Tsusho Inc.)

Thereafter, high power laser is applied on the CNTs layer to make patterns. Fig. 6.3 shows the laser system. The specimen is placed on the X-Y linear stage controlled by a PC and the laser is directed perpendicular to the X-Y linear stage by the lens and mirror. The high power laser will burn out the CNTs where the laser is focused and by controlling the X-Y linear stage, three electrically isolated rectangular islands are created as shown Fig. 6.4. The size of each island is 4 mm height and 40 mm width.

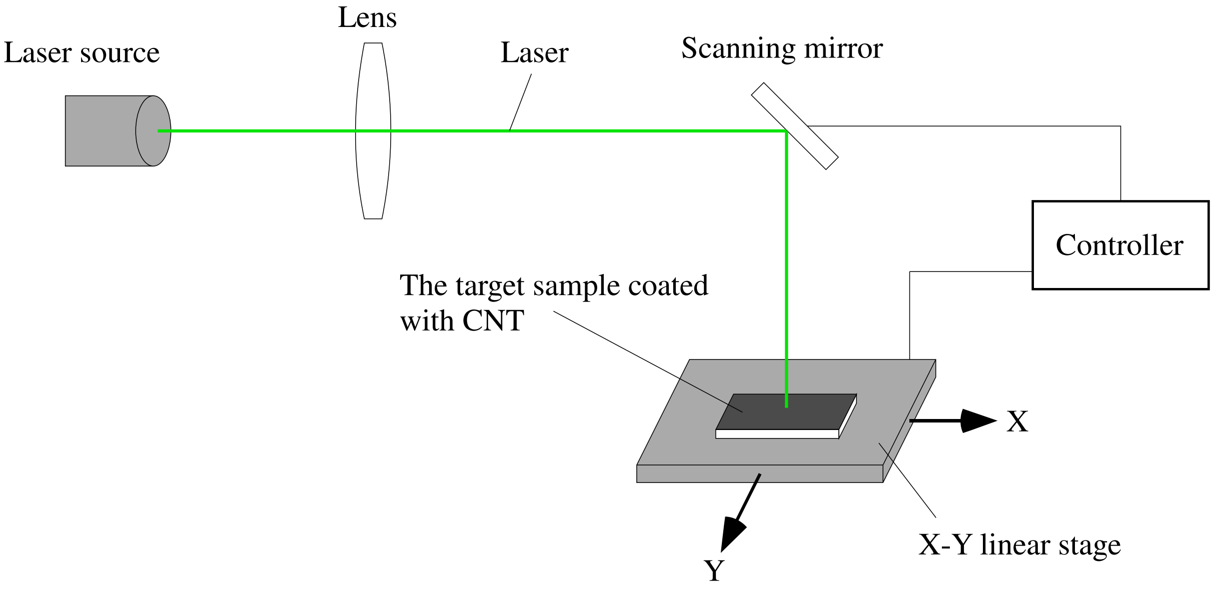

Figure 6.3: Apply laser on the surface of a specimen

The electrical resistance of the soft material is practically infinite and only CNTs are conductive, so the patterns where electricity will flow can be made by removing CNTs by the high power laser. The pictures in the bottom of Fig. 6.4 show the places where the laser is applied and not applied. The electrical isolation is confirmed by measuring the electrical resistance between islands. From the results, it is confirmed that we can create some specific patterns in the CNT layer such as the serpentine pattern used in metal foil strain gages which increases the length in a specific direction and enhances the sensitivity.

Two lead wires are attached to the both sides of each island by silver paste to measure the electrical resistance of each island. Silver paste was chosen because of silver's excellent conductivity. In theory, CNTs shows piezoresistive effect, so the readings of the electrical resistance of each island should change when mechanical strain is applied on the specimen and work as tactile sensor.

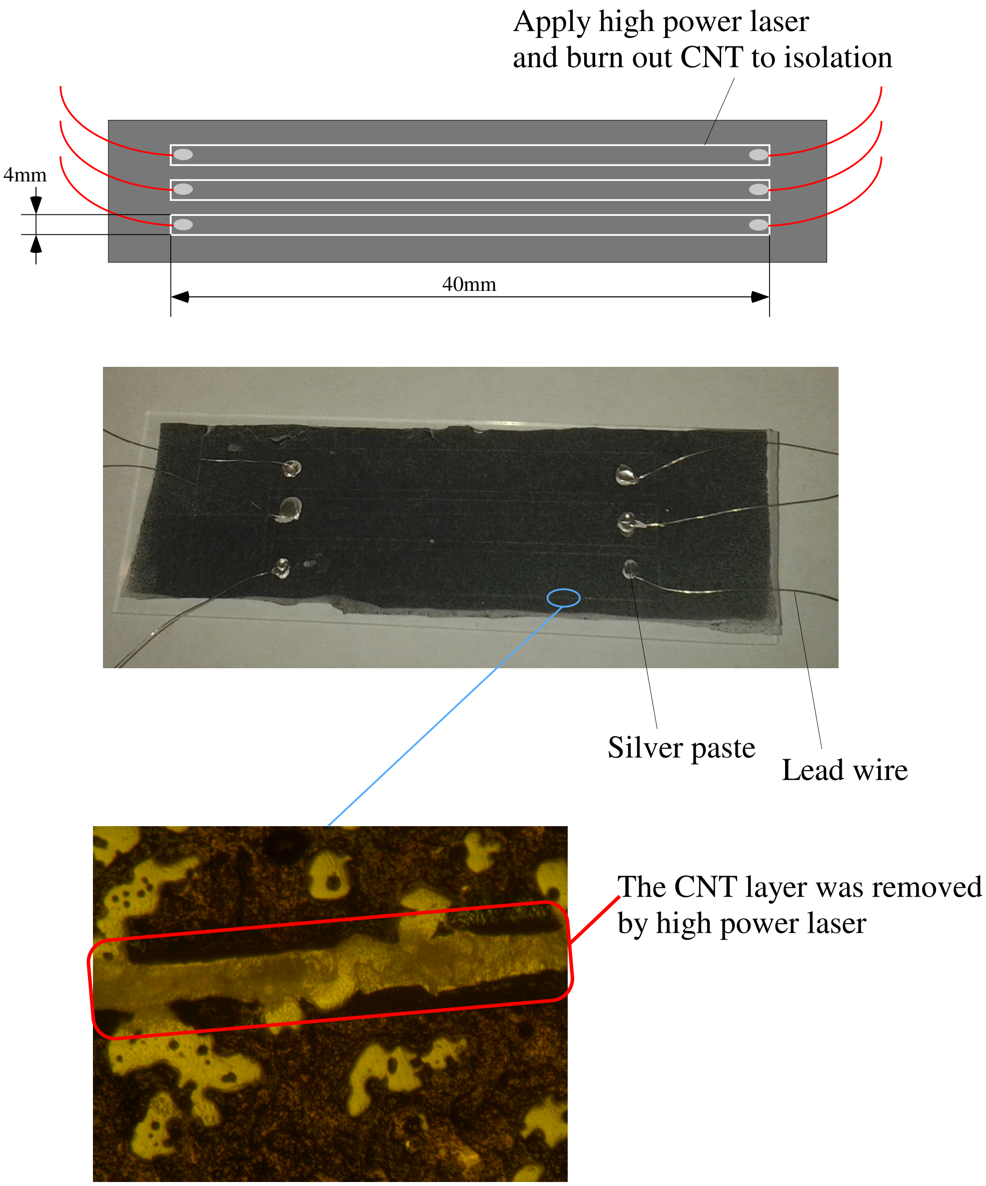

Figure 6.4: Pattern making by high power laser

6.2.2 Experimental setup

The change in electrical resistance when mechanical strain is applied on the specimen is very small, so Wheatstone bridge and differential amplifier are used to measure the small change as shown in Fig. 6.5. This system is similar to the system used with strain gages in Fig. 4.10 in Chapter 4. The main differences are the differential amplifier is simplified and the registers in the Wheatstone bridge are 100 KΩ. It is known that the change in electrical resistance in response to mechanical strain of CNTs is much higher than metal foil gages. Therefore, the necessary amplifying gain is smaller for the CNT based sensor, so amplifying only by one operational amplifier is enough and two operational amplifiers can be removed. The amplifying gain is set to 20 which is about 100 times smaller than the amplifying gain for the strain gages. The electrical resistance of each island in the fabricated specimen are about 100KΩ, so 100KΩ registers are used to create the Wheatstone bridge. The two lead wires attached to the both sides of the isolated island in the CNT layer are connected to the Wheatstone bridge through R_3. The system is configured to the output signal, V_o, is proportional to the electrical resistance of the CNT-based sensor, R_3, and the output signal V_o is recorded by the data acquisition system.

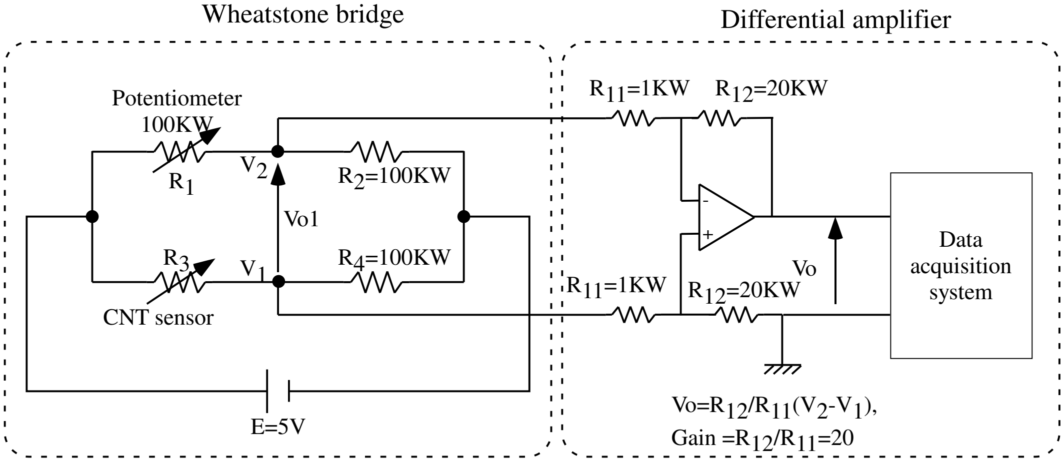

Figure 6.5: Amplifying circuit

6.2.3 Stability test

As tactile sensors, ideally, the output from the sensor should be the same without mechanical strain. However, it is well known that other factors such joule heating also change the output from the sensor, which is called as sensor drift. Therefore, the output from the CNT-based sensor, V_o, is recorded by the data acquisition system without any mechanical strain and Fig. 6.6 shows the results. The 5V power supply to the Wheatstone bridge is powered on at 10s and powered off at 340s. During the 330s, the change of output signal is 100mV and the change is less than 5%. Therefore, the change of output signals more than 100mV can be considered because of mechanical strain.

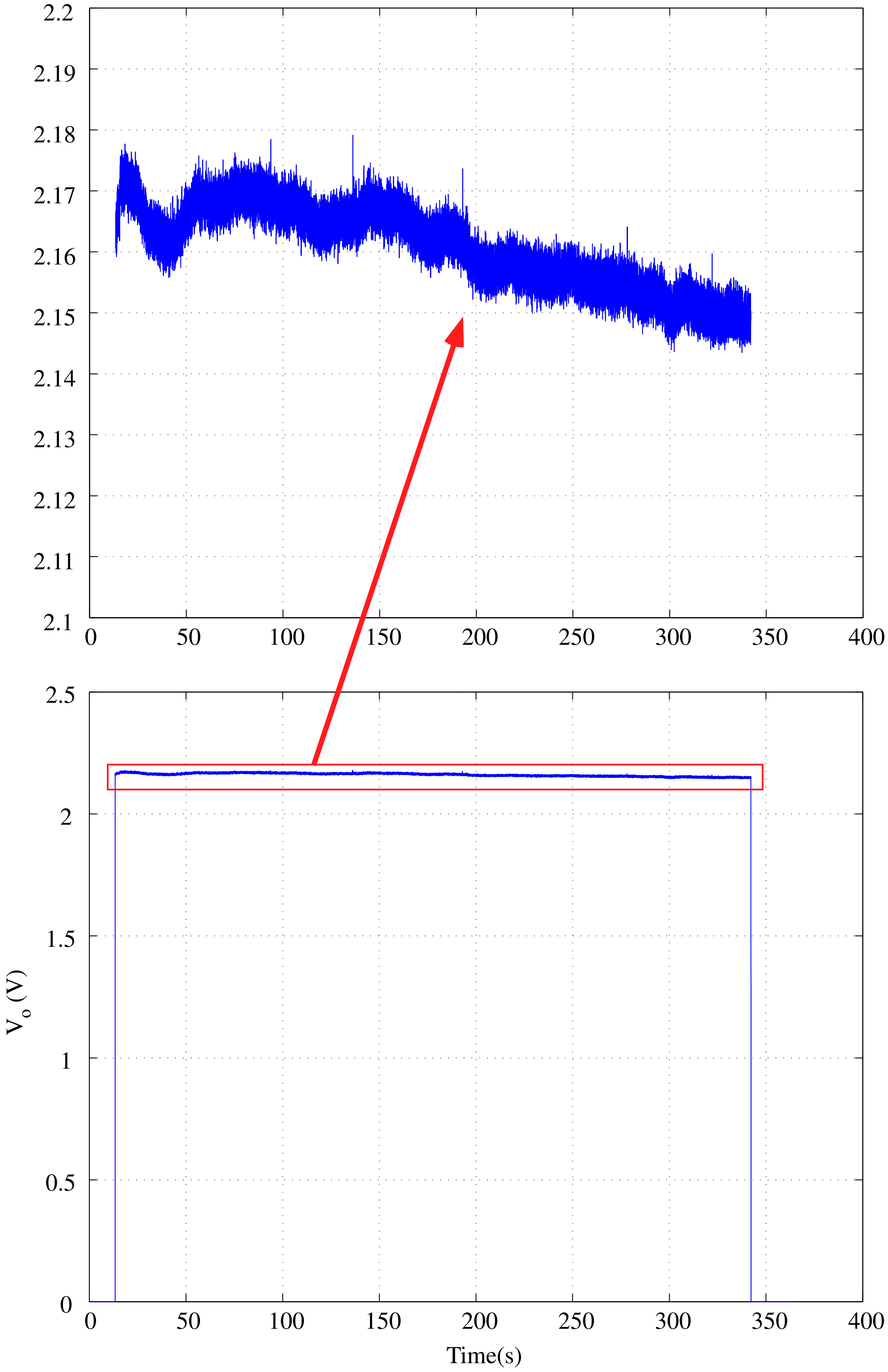

Figure 6.6: Stability test

6.2.4 Bending tests

Tension and compression are applied on the CNT-based tactile sensor by bending and the output signal is recorded by the data acquisition system. By Euler-Bernoulli beam theory, the convex surface will be under tension and the concave surface will be under compression by bending, so both tension and compression can be applied to the CNT layer on the tactile sensor. The CNT-based tactile sensor is put on the equipment consists of the two metallic plates connected by hinges as shown in Fig. 6.7. The left plate is fixed and the right plate is moved up and down to apply compression and tension to the CNT layer. The CNT layer is on the top surface, so the CNT layer will be under compression when the right plate is moved up and under tension when the right plate is moved down. The displacement is defined to positive when the right plate is moved down (tension).

In the experiments, tension is applied to the CNT layer by bending down 4 times and thereafter compression is applied to the CNT layer by bending up 4 times. The experimental results show that the output signal, V_o, goes up when tension is applied in the CNT layer and goes down when compression is applied. The output signal, V_o, is set to be proportional to the electrical resistance of the CNT-based sensor, so the resistance is increased by tension and decreased by compression. These results make sense because the electrical resistance is proportional to the distance between electrodes. These results show that the CNT-based tactile sensor can detect the mechanical strain in both directions. The amount of change of output signal when mechanical strain is applied is in the similar range with the experimental results with metal foil strain gages shown in Chapter 4 although the amplifying gain is about 100 times smaller. This high sensitivity is excellent for tactile sensors because the amplifying circuit amplifies both desired signal and noise. Decreasing the amplifying gain improves the signal-noise ratio which shows the quality of signal.

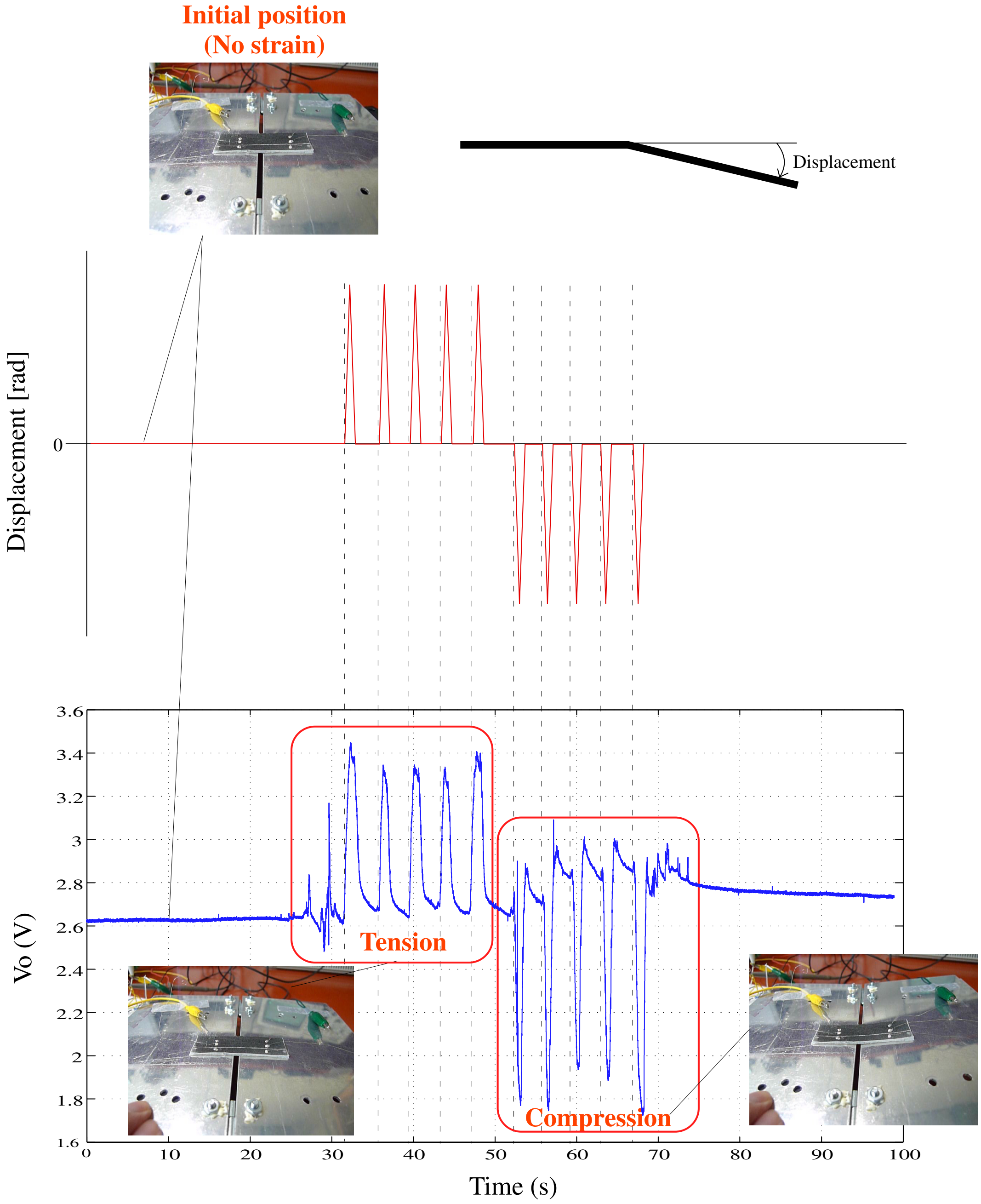

Figure 6.7: Bending tests

6.2.5 Uniaxial tension tests

Uniaxial tension is applied on the CNT-based sensor by clamping on both sides of the CNT-based sensor and changing the position of upper side as shown in Fig. 6.8. First, the displacement is increased by 0.4 mm and kept for 10 seconds in a step function as illustrated in Fig. 6.8. This step is repeated 10 times. Thus, the total displacement after 10 repetitions is 4 mm and the maximum strain is 10% $(\varepsilon = 0.1)$. After the displacement reaches the maximum value at 4 mm, the specimen is kept at 4 mm displacement for 60 seconds. After that, the displacement is decreased by 0.4 mm and kept for 10 seconds in a step function. This step is repeated 10 times to return to the original position.

The experimental results show that the trend of the signal of the CNT-based sensor gradually increases by increasing the displacement in loading, and decreases by decreasing the displacement in unloading. When the displacement is applied by steps, in both directions of loading and unloading, a spike is detected before the signals are quickly and exponentially decayed in the interval of 10 seconds.

A total of 10% strain $(\varepsilon = 0.1)$ is applied during the experiments without damaging the CNT-base sensor. This is not recommended for typical strain gages, such as foil strain gages. For instance, the maximum allowable strain for the strain gages used in Chapter 4 is about 0.15% $(\varepsilon = 0.0015)$. In addition, the sprayed CNT layer did not appear to suffer any damage. The CNTs remain attached to the silicone substrate very well after experiments. The flexibility and durability are some of the advantages of the CNT-based sensor. Furthermore, the spike signal after changing the displacement is the most significant in the response which is similar to the responses of Fast-Adapting (FA) mechanoreceptors in human skin as shown in Fig. 4.2. Therefore, the CNT-based sensor can be an excellent choice for artificial skin sensors.

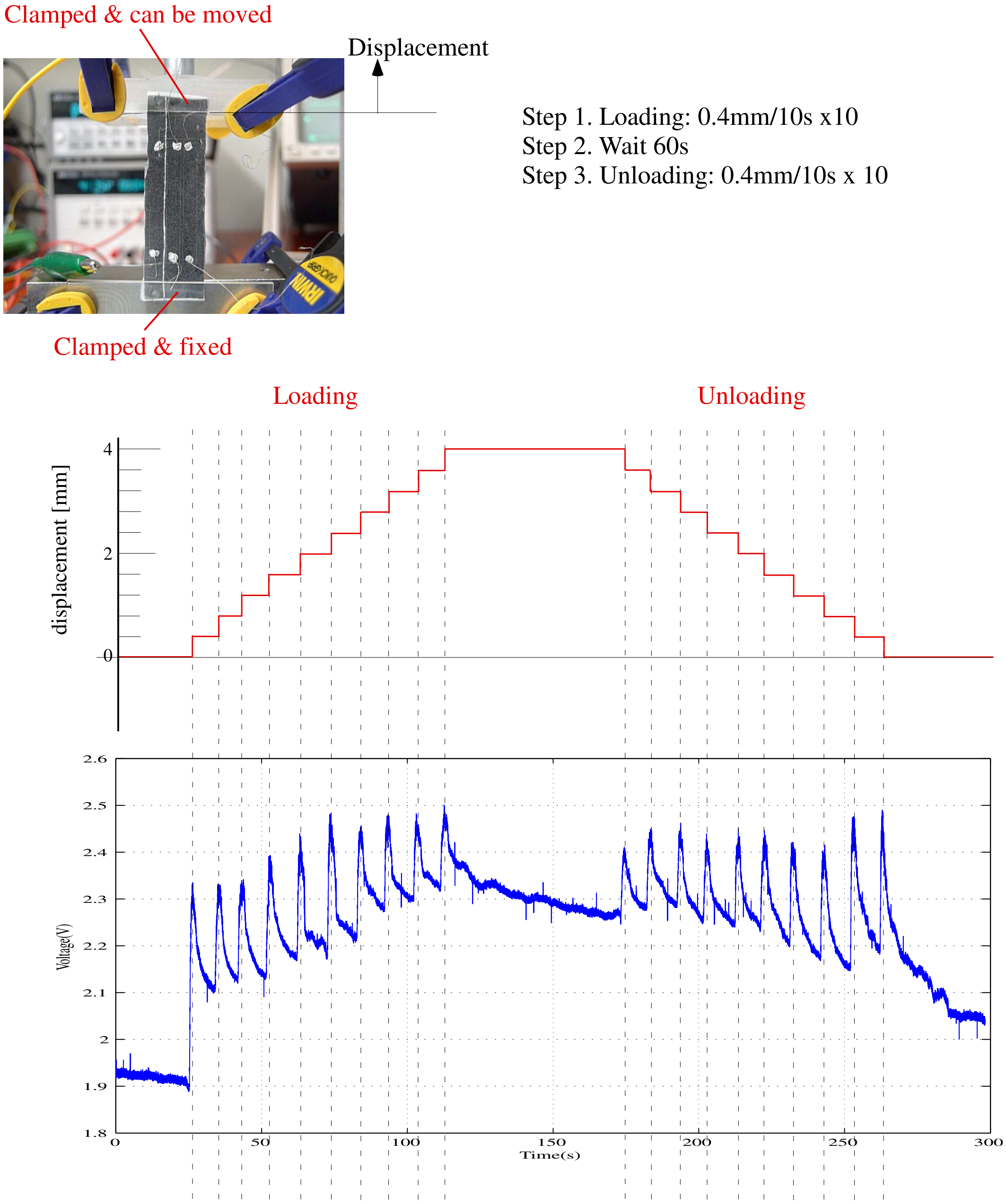

Step 1. Loading: 0.4mm/10s x10
Step 2. Wait 60s
Step 3. Unloading: 0.4mm/10s x 10

Figure 6.8: Uniaxial tensile tests

6.3 Summary of CNT-based sensor

There are two reasons why the sensitivity of the CNT based sensor is higher than typical metal foil strain gages. One is the gage factor, which shows the sensitivity of material, of CNTs is higher than metals. The other is the CNT layer is flexible and can be deformed by following the large deformation of soft material. In contrast, if a metal foil strain gage is used with a soft material, the strain gage is much harder than the soft material, so the deformation of the strain gage is much smaller than the deformation of the soft material at the same loading conditions. The stiffness mismatch between the strain gage and soft material causes relative motions and complex strain concentration at the boundary and sometimes the direction of output signal (*i.e.*: tension vs. compression) is opposite to intuition. For instance, in experiments, it is observed that the tension or compression determined by the strain gages attached on the surface of the beam made by soft material contradicted the beam-theory. In addition, the stiffness mismatch will cause delamination when large deformation is applied and the sensor will no longer function properly. In the experiments, the CNT-based tactile sensor showed high sensitivity and the flexibility compatible with soft materials, so the CNT-based tactile sensor is better suited to make artificial skin sensors. Future work, based on the initial study, is proposed in Chapter 9.

Chapter 7

The effects of a core in a soft finger

7.1 Introduction

Grasping and dexterous manipulation by robot hands has been studied for a long time and modeling and analysis of the contact forces between fingertips and objects are important issues. In most of cases, point contacts between robot fingertips and target objects are assumed and the friction cone derived from Coulomb friction is used to analyze and model the contact forces between the fingertips and the objects. Fig. 7.1 shows an example of the friction cone where N is applied normal force, F_t is applied tangential force, F_c is contact force, and μ is coefficient of friction. The contact force, F_c, must be inside of the friction cone defined by μ. If tangential force, F_t, is greater than the maximum friction force, μN, and the vector composition of normal and tangential forces, $F_t + N$, is outside of the friction cone, the contact force F_c is limited by the friction cone and the excessive force, $F_t - \mu N$, causes slip at the contact point.

$$F_c = \begin{cases} N + F_t & \text{if } 0 \le F_t \le \mu N \quad \text{(Maintain contact)} \\ N + \mu N & \text{if } \mu N < F_t \quad \text{(Slip)} \end{cases} \tag{7.1}$$

In grasping and manipulation by robot hands, typically, rigid body and point contacts are assumed because it is easier to analyze. However, practically, the fingertips of robot hands are covered with soft materials such as rubber to increase stability. The outer soft

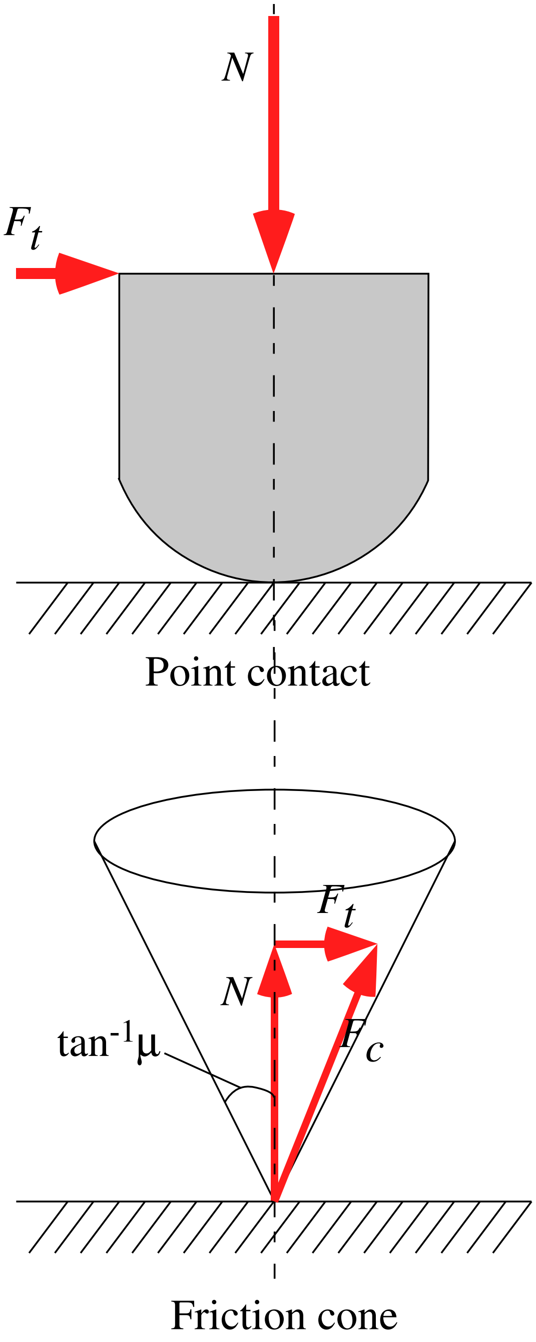

Figure 7.1: Friction cone

layer increases the coefficient of friction and decreases the contact pressure by increasing the contact area. It is very important to handle fragile objects. The soft material will deform during the grasping and manipulations, so the contact between the soft material and target objects becomes area contact. The modeling and analysis of the area contacts with soft finger was proposed by Cutkosy and friction limit surface correspond to friction cone in point contacts are studied [75, 76, 77, 78, 79, 80, 81, 82]. The friction limit surface is defined by the equation for ellipse

$$\frac{F_t^2}{(F_{t\,max})^2} + \frac{M^2}{(M_{max})^2} = 1 \tag{7.2}$$

where $F_{t\,max}$ is the maximum tangential force at contact given by the Coulomb friction law, and m_{max} is the maximum moment that can be exerted by the area contact, without tangential force, before sliding. The combination of contact forces, F_t and M, must be inside of the limit surface and if the combination of contact forces, F_t and M, at the outside of the limit surface are applied, it causes slip. Point contact cannot maintain contact with any moment but area contact can maintain some moment, so area contact is more stable than point contact.

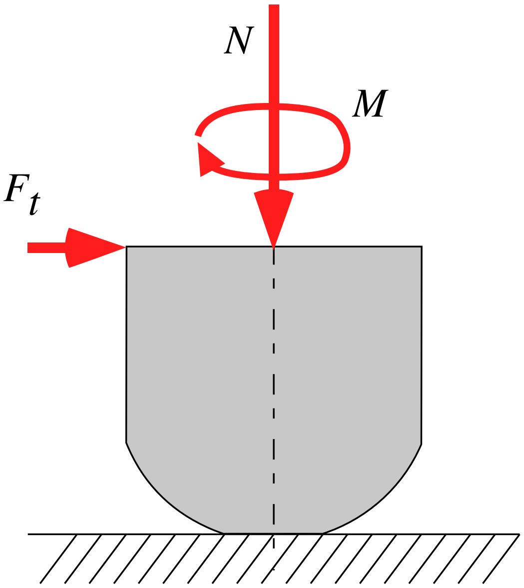

Area contact

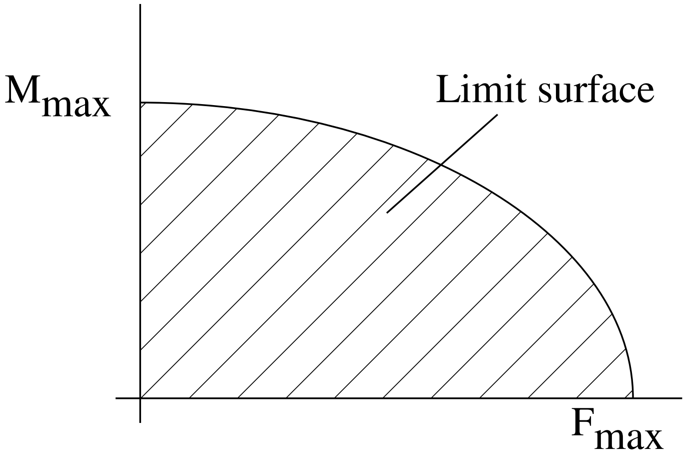

Figure 7.2: Limit surface

In area contact, the relationship between normal force and contact area is necessary to estimate the contact force and Hertzian contact [83, 84] is the fundamental theory which shows the relationship between the radius of contact area a and the applied normal force N at the contact between sphere and plate as shown in equation (7.3) and Fig. 7.3.

$$a = cN^{\frac{1}{3}} \tag{7.3}$$

where c is a constant.

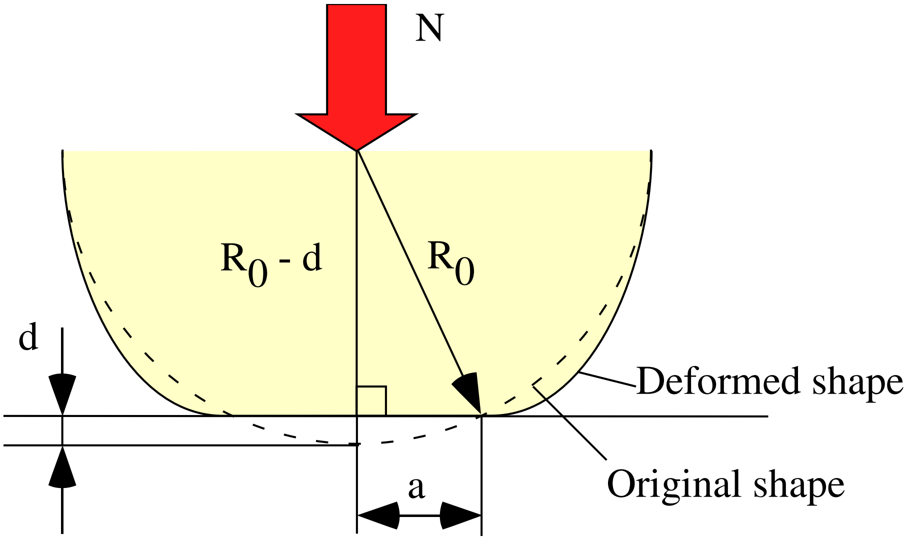

Figure 7.3: The contact interface between hemisphere and rigid plate

Hertzian contact is limited to linear elastic materials and small deformations, however, soft materials typically show nonlinear elasticity and large deformation. Therefore, the theory is extended by Xydas and Kao [63, 62] to nonlinear elastic materials and large deformations by the power-law equation

$$a = cN^{\gamma} \tag{7.4}$$

where the exponent γ is a parameter which has the range of $0 \leq \gamma \leq \frac{1}{3}$ and depends on material properties. Hertzian contact is a special case of the power-law equation where the exponent $\gamma = \frac{1}{3}$.

The current study of soft fingertips based on power-law theory focuses on homogeneous material. However, most of the artificial fingertips in robot hands are inhomogeneous because they are made from a hard core covered with much softer material similar to human fingertips which consist of hard bones covered with soft subcutaneous tissue and skin.

This Chapter discusses the effect of the hard core on the power-law equation. First, hemispherical soft fingertips composed of homogeneous nonlinear elastic material are analyzed by Finite Element Method (FEM) and the results are compared with experimental results to verify the accuracy of the FEM model. Thereafter, soft fingertips with a rigid core are analyzed by FEM and based on the results, the effects of the core in soft fingertips and design criteria of soft fingertips are discussed.

7.2 Finite Element Method (FEM) modeling and simulation

By using ABAQUS, a standard FEM software, hemispherical soft fingertips are modeled and the radius of contact, *a*, of the fingertip pushed against a rigid plate is simulated and the results are compared with experimental results to ensure the accuracy of the modeling in FEM.

7.2.1 FEM modeling

A cross section of the hemispherical soft fingertip model composed of incompressible, homogeneous nonlinear elastic and isotropic material is illustrated in Figure 7.4(a). The loading of the fingertip is normal to the rigid plane in contact with the fingertip (i.e., along the 2 direction), and the fingertip is fully constrained on the upper surface as shown. In addition, only half of the fingertip is considered in the analysis due to symmetry. Appropriate constraints in the *x* direction (direction 1 in Figure 7.4) are imposed along the axis of symmetry. The element size is gradually increased for locations away from the contact surface as shown in Figure 7.4(b). This helps to reduce the size of the problem which results in reduction of computational time.

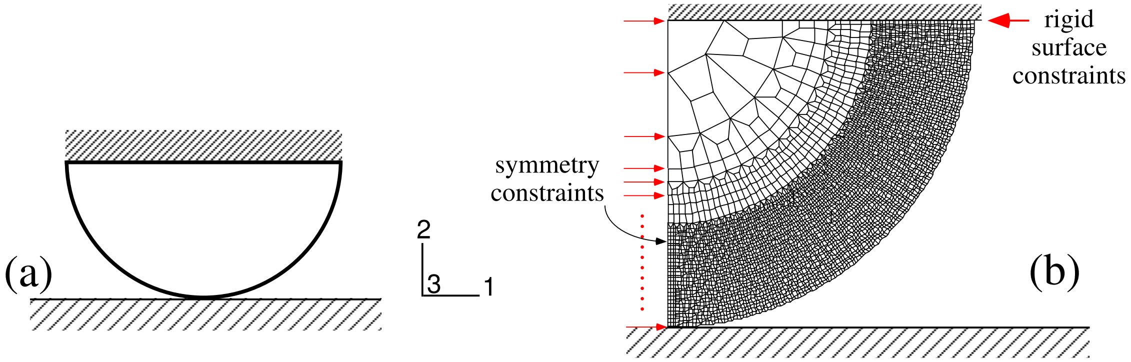

Figure 7.4: (a) Symmetric cross section of the FEM fingertip model (1, 2, and 3 directions correspond to *x*, *y*, and *z*). (b) The nodes on the top are fully constrained. The nodes located along the axis of symmetry are fully constrained along one direction to satisfy the equilibrium condition. At the tip-object contact pair the friction coefficient is 0.89. This was obtained through experiments. Displacement boundary condition is imposed on the upper rigid surface.

The fingertips are modeled with 5530 4-noded, axisymmetric, quadrilateral, hybrid, and reduced integration elements. In order to have sufficient spatial resolution to calculate the contact radius, a, approximately square elements of $0.109\,mm$ are used at the contact interface. The size of contact elements has been optimized to provide enough resolution, and at the same time to prevent termination of the process due to severe element distortion caused by the small size of the element mesh.

7.2.2 Modeling of the nonlinear elasticity

Usually, soft materials show nonlinear elasticity, so the nonlinear elastic model of the ABAQUS software package is used with the material properties obtained from uniaxial compression test. INSTRON Model 1011 tensile testing machine was used to compress a parallelepiped specimen made of neoprene rubber and its geometry is $18.69 \times 21.67 \times 21.79\,mm$. Before the compression test, petroleum jelly was applied on the loading plates of the test machine to minimize the friction at the contact interface and prevent the bulging of the sides. During the test, the velocity of the compression testing machine was set to 0.25 in/min to satisfy quasi-static conditions and to reduce hysteresis effects. Figure 7.5 shows the nonlinear elasticity, stress-strain relation, of the specimen obtained by the experiments. ABAQUS provides the HYPERELASTIC [85] option with Ogden [86] parameter and the experimental results are used to model the nonlinear elastic constitutive relation in the FEM analysis.

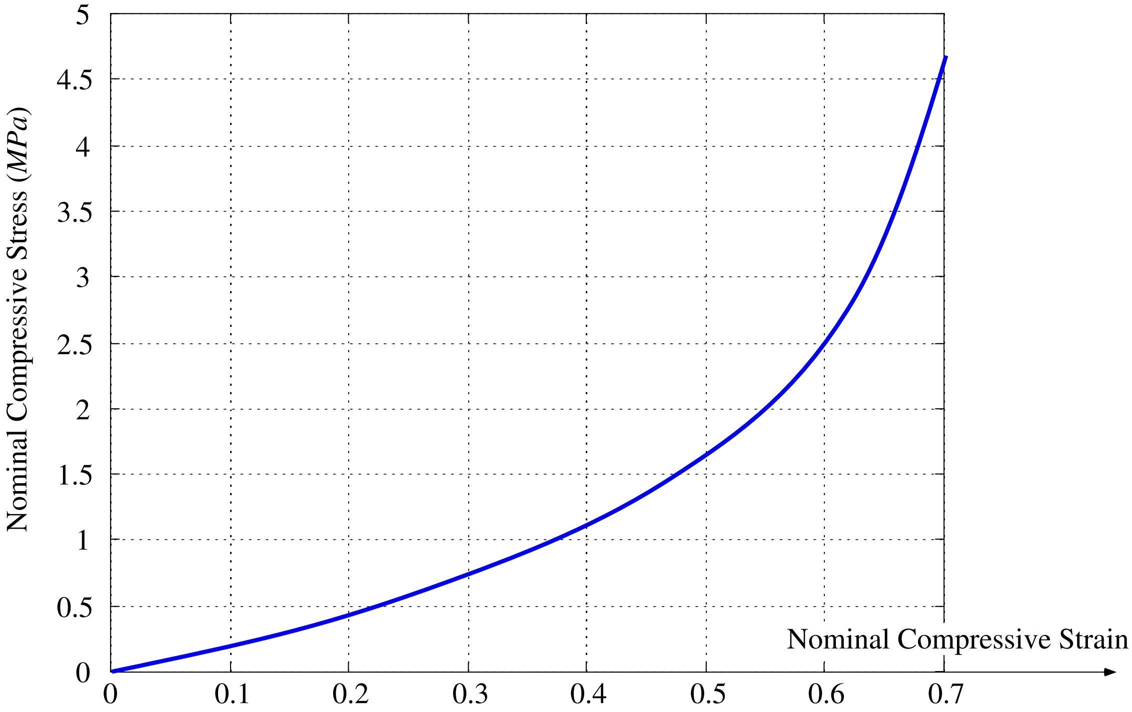

Figure 7.5: Experimental results of uniaxial compression test for Neoprene rubber, with the size of $18.69 \times 21.67 \times 21.79\,mm$

The nonlinear stress-strain relation of the specimen is simulated by FEM with previously obtained nonlinear elastic constitutive relation and compared with the experimental results to confirm the accuracy of the nonlinear elastic constitutive relation. Non-frictional boundary conditions were used at the top and the bottom of the model to simulate exactly the non-friction contact between the specimen and the compression plates. Figure 7.6 illustrates the simulation of uniaxial compression of the rubber block. The undeformed as well as the deformed positions of the specimen are indicated.

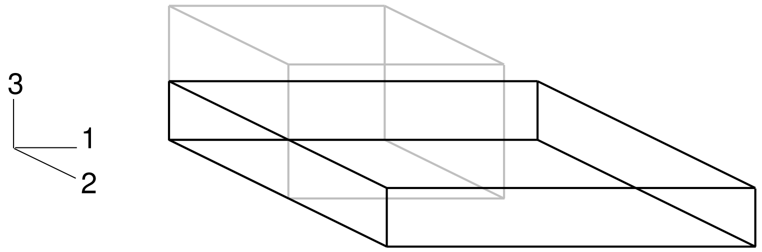

Figure 7.6: Simulation of uniaxial compression of a $18.69 \times 21.67 \times 21.79\,mm$ specimen. The original position is indicated in light grey lines while the deformed in dark solid lines.

Figure 7.7 compares the experimental results with the simulated force-displacement results. A difference of less than 5% was observed by comparing the compression test results with the simulated results and the simulation validates the constitutive relationship calculated by ABAQUS.

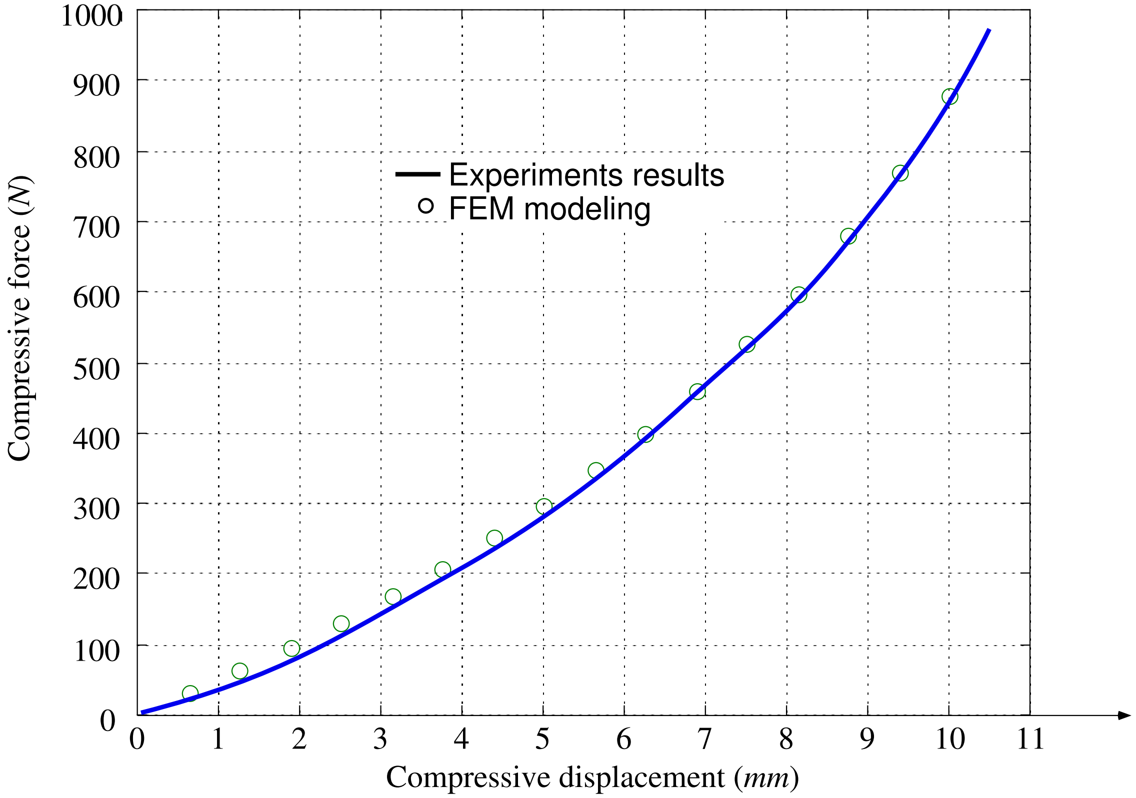

Figure 7.7: Comparison between experimental and simulated force-displacement results shows very good agreement.

7.2.3 Comparison of FEM vs. experimental results

Three hemispherical fingertips of the same material but different sizes, with $7.65mm$, $12.61mm$, and $17.45mm$ radii of curvature were tested by FEM and experiments and results are compared to confirm the accuracy of the FEM model.

In experiments, the fingertips are composed of neoprene rubber balls that have been halved and glued with epoxy adhesive to the metallic rigid posts to form artificial soft fingers. Fig. 7.8 shows the experimental setup. INSTRON Model 1011 tensile testing machine was used for the experiments. The load capacity of the system is $11,330N$ ($2,546lb$). The fingertip was mounted on a load cell and pushed against the rigid smooth plate of the machine. The fingertip is first coated with a thin layer of very fine toner dust so that it would

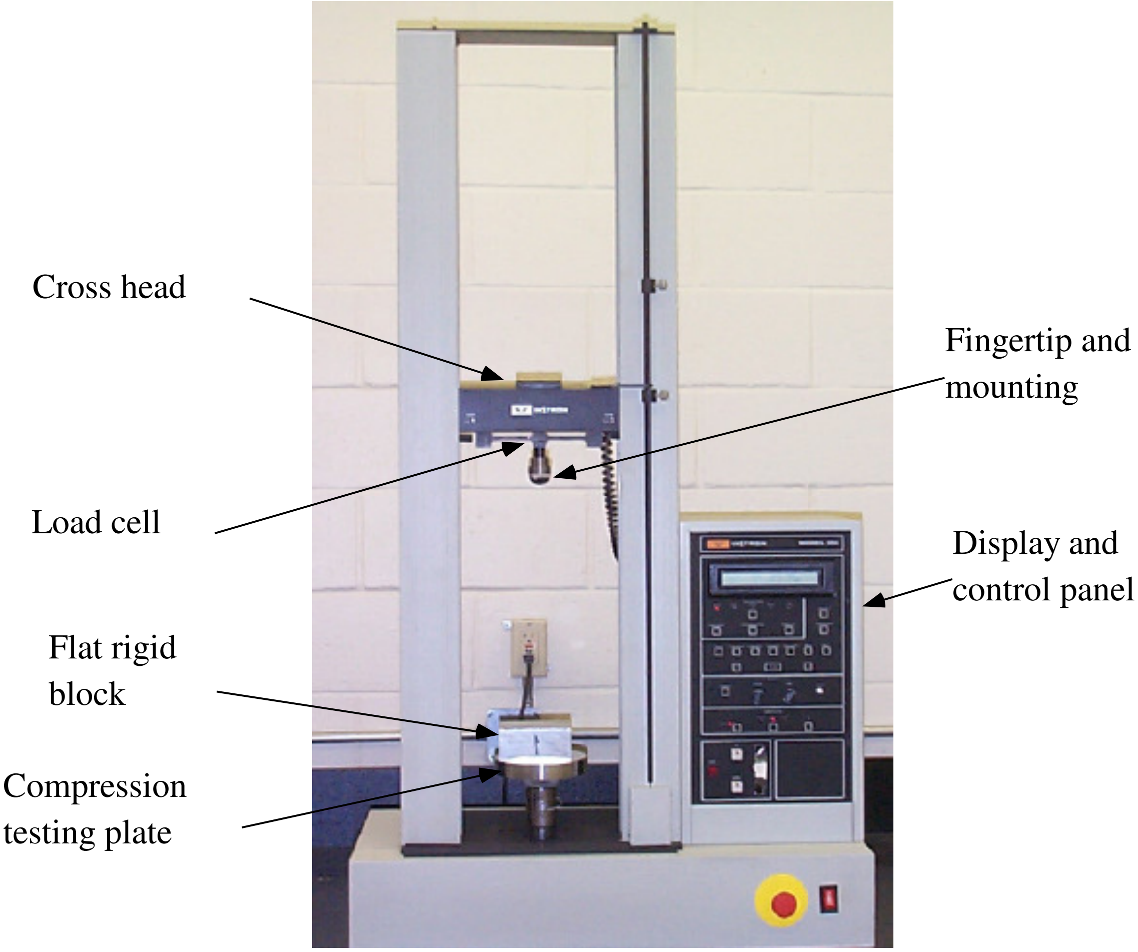

Figure 7.8: Experimental setup of soft fingertips

leave a clean and vivid finger print upon contact with the recording paper. The radii of contact for a wide range of normal forces of the rubber fingertips for various configurations were measured on the recording paper. The normal forces are accurately measured by the load cell and displays on INSTRON 1011.

In FEM, the normal force N is measured at the reference node associated with the top rigid surface and the area of contact is calculated based on the number of elements contacting with the lower rigid plane. The deformation of the fingertip simulated by FEM is illustrated in Figure 7.9.

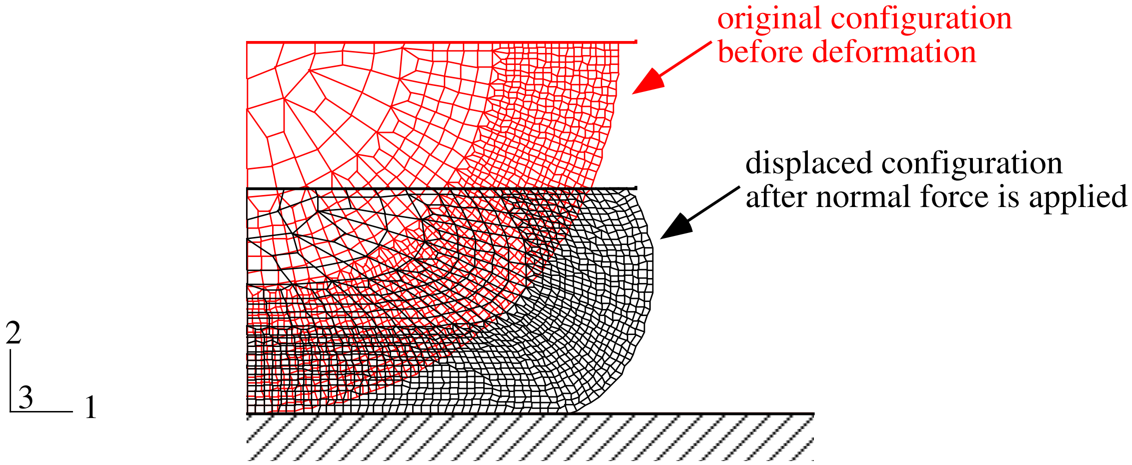

Figure 7.9: m Displaced fingertip after vertical displacement was imposed during FEM analysis. The original and displaced positions are indicated.

Figure 7.10 shows the results of contact radius vs. normalized normal force for FEM analysis and experiments for all three fingertips. For the case where $R_0 = 7.65\,mm$, $R_0 = 12.61\,mm$ and $R_0 = 17.45\,mm$, it is noted that errors less than 5% are observed for $\frac{a}{R_0} > 0.2$, $\frac{a}{R_0} > 0.23$ and $\frac{a}{R_0} > 0.29$, respectively.

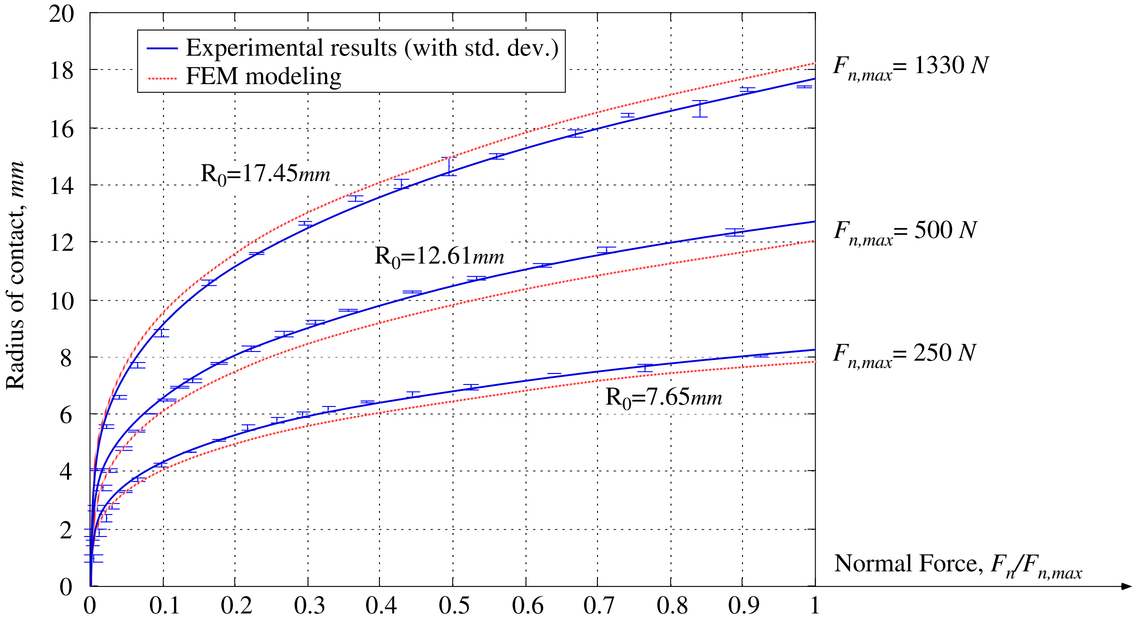

Figure 7.10: Comparison between FEM analysis and experimental results for fingertips with radii $R_0 = 7.65\,mm$, $R_0 = 12.61\,mm$ and $R_0 = 17.45\,mm$. The force is normalized for comparison purposes. The range of the forces applied to each fingertip is $0 \sim 250N$, $0 \sim 500N$, and $0 \sim 1350N$ for small, medium, and large fingertips, respectively.

Table 7.1: The best-fit power-law equations for three hemispherical fingertips with different radii of curvature.

Radius of curvature	*Power-Law equation*	
$R_0 = 7.65\,mm$	FEM	$a = 1.59\,N^{0.2901}$
	experiments	$a = 1.75\,N^{0.2812}$
$R_0 = 12.61\,mm$	FEM	$a = 1.91\,N^{0.2962}$
	experiments	$a = 2.15\,N^{0.2864}$
$R_0 = 17.45\,mm$	FEM	$a = 2.39\,N^{0.2819}$
	experiments	$a = 2.22\,N^{0.2879}$

The coefficients of c and γ in the power-law equation are obtained by the weighted least-squares fitting [87, 88, 62] and tabulated in Table 7.1. The results from FEM and experiments show good agreement and it verifies the accuracy of the modeling of the hemispherical soft fingertips.

7.3 The effects of the core in soft fingertips

Most artificial fingertips are made from a core covered with soft skin. This Section describes the effects of the core as simulated by FEM and design criteria to determine the thickness of the soft skin are discussed. Three types of fingertips with the same outside radius, $R_c = 17.45mm$, and different inside core radii, $R_c = 0\,mm, 12.7\,mm$, and $R_c = 14.1\,mm$, as shown in Fig. 7.11 are analyzed by FEM. The FEM model created and verified in the previous Section is reused and the existence of a rigid core is modeled by adding the constraint to the boundary between the rigid core and soft skin. By following the same step with previous FEM analysis, the contact radius vs. normal force curves are simulated by FEM (ABAQUS) and results are shown in Fig. 7.12. Thereafter, the coefficients of c and γ in the power-law equation are computed and tabulated in Table 7.2.

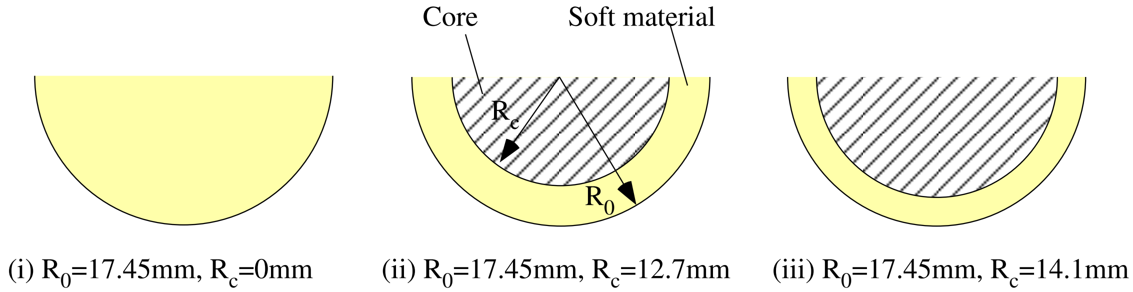

(i) R_0=17.45mm, R_c=0mm (ii) R_0=17.45mm, R_c=12.7mm (iii) R_0=17.45mm, R_c=14.1mm

Figure 7.11: The cross section of hemispherical fingertips used in the analysis

Radius of Core (R_c)	Power-law Equation
0 mm	$a = 2.39\,N^{0.2819}$
12.7 mm	$a = 1.89\,N^{0.2662}$
14.1 mm	$a = 1.82\,N^{0.2530}$

Table 7.2: The best fit power-law equations for three different core radii configurations

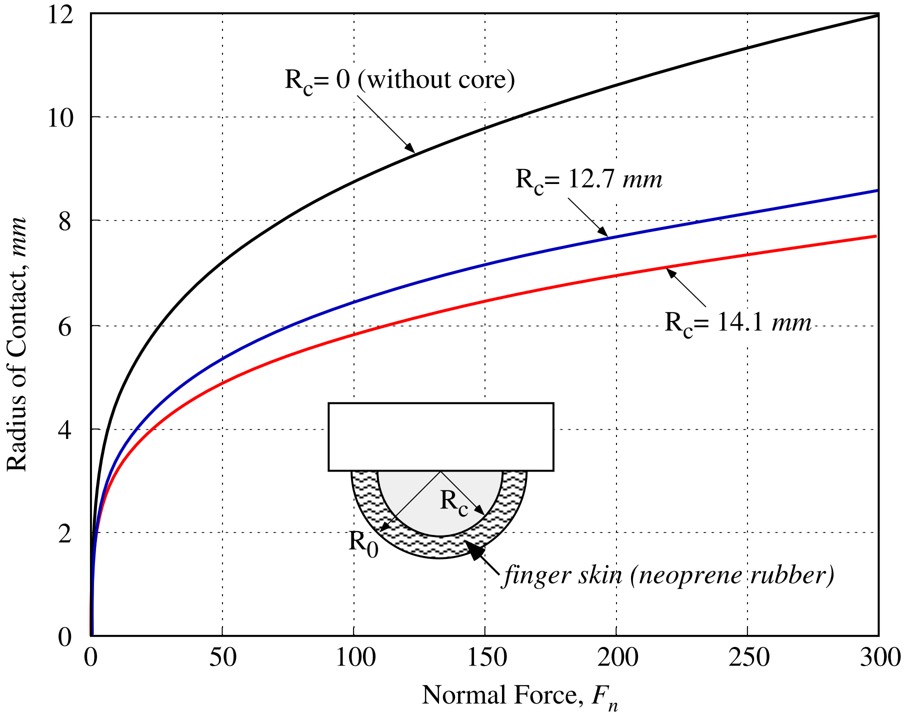

Figure 7.12: Normal force vs. radius of contact for fingertips with different core sizes. The outside radius of all three fingertips is $R_0 = 17.45\,mm$, and the material is neoprene rubber.

Figure 7.13 shows the effects of a rigid or elastic core on the exponent, γ, and the coefficient, c, in the power-law equation. Without a core, the exponent, γ, was almost the same if the change is only by scaling as shown in Table 7.1. However, with a core, the geometry is not similar because the total size R_0 is kept constant while the radius of the core R_c is increasing simultaneously, thus modifying the exponent, γ, by increasing the thickness of the soft layer. With a core, the exponent, γ, should be the same if the ratio between R_0 and R_c is constant and the only change is scaling.

The initial value of the exponent, γ, depends on a rigid core or elastic core. With a elastic core, the exponent, γ, shows discontinuity in the very beginning. In this Chapter, rigid means impossible to deform and no deformation at all by any applied forces. Thus, with a rigid core only and with the thickness of the soft layer, $(R_0 - R_c)$, at zero, there is no deformation, so the exponent, γ, and the coefficient, c, should be zero. Thereafter, the exponent, γ, and the coefficient, c, are continually increased by increasing the thickness of the soft layer as shown in Figure 7.13(a). With an elastic core only, such as metal, and with the thickness of the soft layer at zero, the deformation is very small, $\frac{a}{R_0} << 1$ and shows Hertzian-contact, so the coefficient, c, is

$$c = \left(\frac{3R_0}{4E^*}\right)^{\frac{1}{3}} \times 1000,\; E^* = \frac{E_c}{1-\nu_c^2} \tag{7.5}$$

Where E_c is Young's modulus and ν_c is Poisson's ratio of the elastic core. In this case, the unit of the contact radius, a, obtained by the power-law equation (7.4) is *mm*. For instance, if the elastic core is polystyrene, $E_c = 3.5\,GPa$ and $\nu_c = 0.35$, so $c = 0.15$ and $\gamma = 1/3$ at $R_0 = R_c$. If the exponent, γ, is $1/3$ and the thickness of the soft layer is zero, the exponent, γ, suddenly decreases after adding a thin soft layer and gradually increases by increasing the thickness of the soft layer as shown in Figure 7.13(b) and the exponent γ is discontinuous. The discontinuity can be explained by the sudden change of the dominant material properties which decide the deformation pattern because of strain concentration in the thin soft layer.

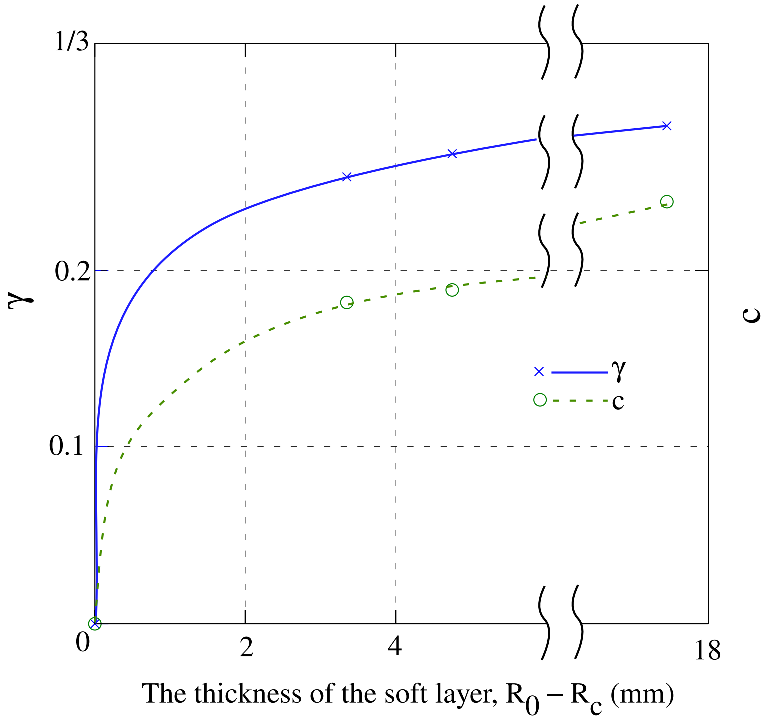

(a) With a rigid (impossible to deform) core, the exponent γ is zero when $R_c = R_0$, rigid core only, because there is no deformation at all.

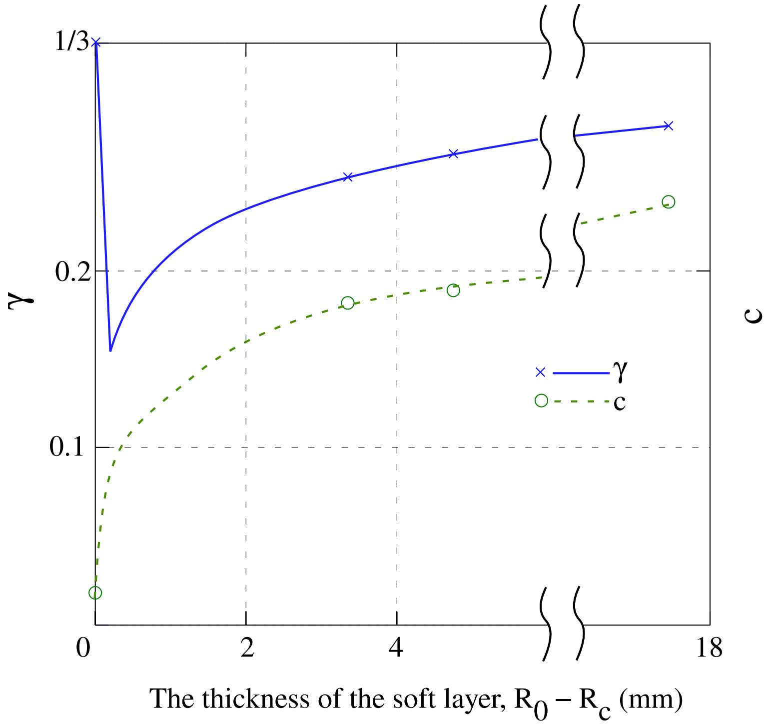

(b) With a elastic core, such as metal, the exponent γ is $1/3$ when $R_c = R_0$, elastic core only, because the deformation is very small, $\frac{a}{R_0} << 1$, and the elastic core shows Hertzian-contact.

Figure 7.13: The effects of a core on the the exponent, γ, and the coefficient, c, of the power-law equation.

Figure 7.14 models a fingertip with a thin soft layer and an elastic core by two cylinders to show the strain concentration in the soft layer and explain the discontinuity. To simplify, the cross section is assumed to be the same, A. The equivalent spring constants of the core, k_c, and of the soft layer, k_s, are

$$k_c = \frac{AE_c}{L_c},\ k_s = \frac{AE_s}{L_s} \tag{7.6}$$

Where E_c and L_c represent Young's modulus and the length of the core, respectively and E_s and L_s represent Young's modulus and the length of the soft layer, respectively. The displacements of the core, δ_c and the displacement of the soft layer δ_s can be calculated as follows

$$\delta_c = \frac{FL_c}{E_cA},\ \delta_s = \frac{FL_s}{E_sA} \tag{7.7}$$

Therefore, the strain ration $\frac{\delta_s}{\delta_c}$ is

$$\frac{\delta_s}{\delta_c} = \frac{L_sE_c}{L_cE_s} \tag{7.8}$$

For example, the strain ratio $\frac{\delta_s}{\delta_c}$ is 111.1 if $L_c = 0.9L$, $L_s = 0.1L$, $E_c = 3.5\,GPa$, and $E_s = 3.5\,MPa$. Although the thickness of the soft layer is only 10 percent of the fingertip, it bears more than 99 percent of the strain. The exponent, γ, in the power-law equation determines the deformation pattern, so that if the most of deformation is because of the thin soft layer, the properties which mainly determine the exponent, γ, should come from the soft layer although it is thin. The dominant properties which decide the exponent, γ, suddenly changes from the core to the soft layer. When adding a thin soft layer, this sudden change can cause the discontinuity of the exponent, γ, as shown in Figure 7.13(b).

The strain will concentrate in the soft layer in the beginning, however, usually soft materials show non-liner stiffness and at some point, the stiffness becomes similar to the elastic core and the deformation of the elastic core is also considerable. Figure 7.15 shows the non-liner stiffness of the soft layer which is getting closer to the stiffness of the elastic core. The stiffness of the soft layer is numerically calculated based on the experimental results shown in Figure 7.5. When the spring constant of the soft layer, K_s, is much smaller

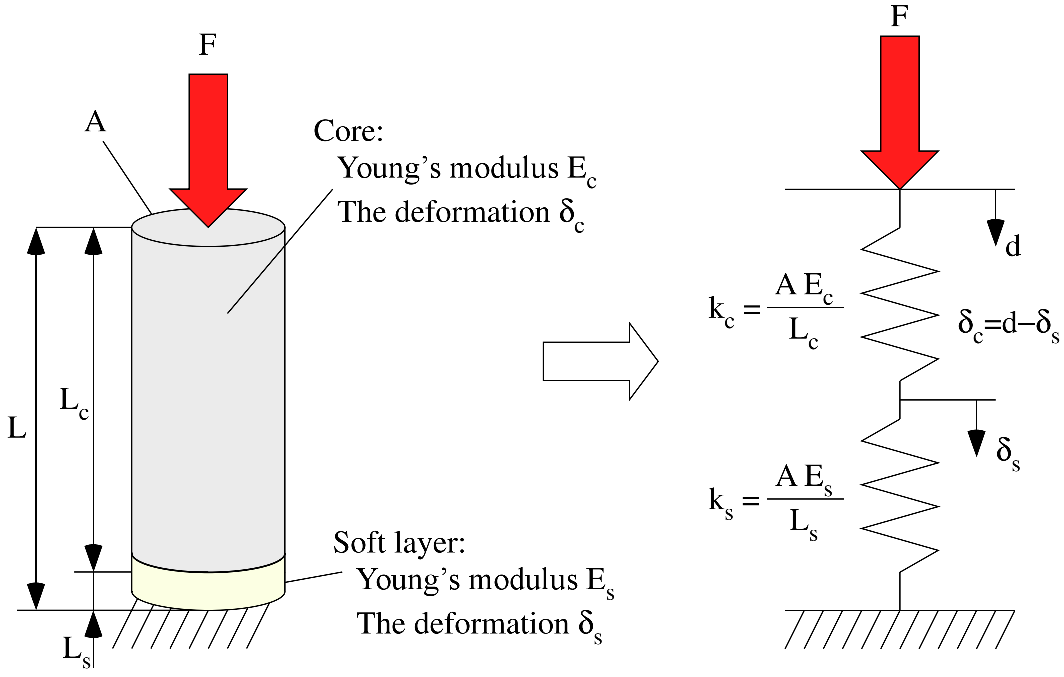

Figure 7.14: The composite model with a thin soft layer and a core

than the spring constant of the elastic core, K_c, the properties of the soft layer dominate the total displacement, d, and the parameters in the power-law equation, however, after the stiffness of the soft layer increases by increasing the strain of the soft layer, the properties of both the soft layer and the elastic core will affect the total displacement, d, and the parameters in the power-law equation. Here, we assume that the properties of the soft layer are dominant when

$$K_c \geq 20K_s \tag{7.9}$$

or

$$0.05C_s \geq C_c \tag{7.10}$$

where C_c and C_s are the compliance of the elastic core, $\frac{1}{K_c}$, and the compliance of the soft layer, $\frac{1}{K_s}$, respectively. In the previous example, this threshold is exceeded when the Young's modulus of the soft layer exceeds $17GPa$ and from Figure 7.15, the corresponding strain is about 0.6. This value is affected by the thickness of the soft layer because the spring constant is affected by the initial length as shown in equation (7.6), the Young's modulus of the soft layer, and the elastic core.

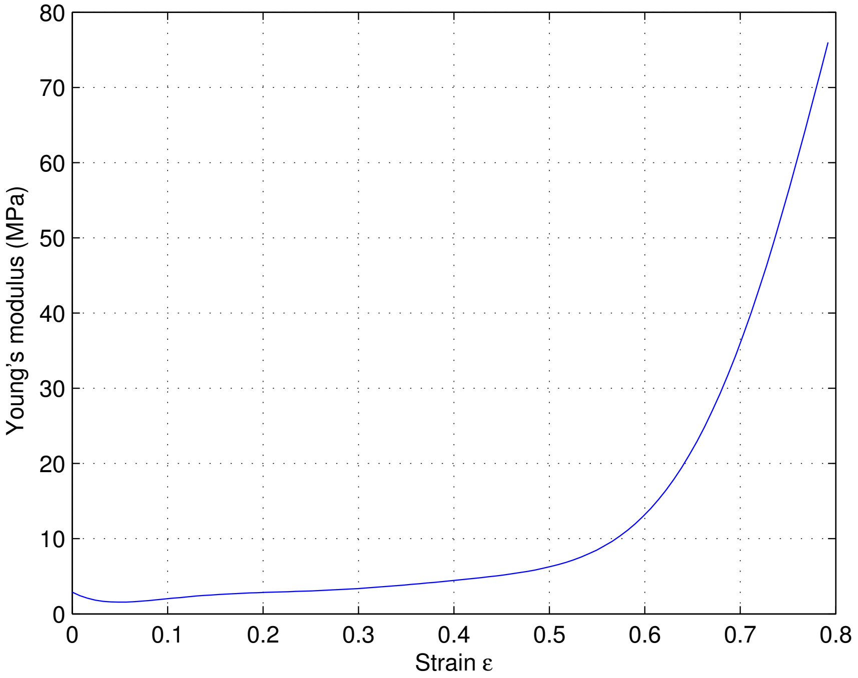

Figure 7.15: The strain-young's modulus curve of the soft material

Figure 7.16 illustrates an example of how the total amount of displacement in the direction of normal force, d, comes from the displacement of the elastic core, δ_c, and the displacement of the soft layer, δ_s. The displacement of the elastic core is calculated by equation (7.7), and it shows liner property. The displacement of the soft layer is calculated from the experimental results shown in Figure 7.5, and it shows non-liner property. Although the thickness of the soft layer, L_s, is 10% of the total length, L, the total displacement, d, and the displacement of the soft layer, δ_s, are nearly the same until the strain of the soft layer, ε_s, exceeds 0.5 and shows the nonlinear property of the soft layer. Thereafter, the difference between d and δ_s because of δ_c becomes visible. The properties, as a composite structure, look almost the same as the properties of the soft layer in the beginning although the thickness of the soft layer is very thin.

In the previous examples, the vertical displacement in the direction of normal force,

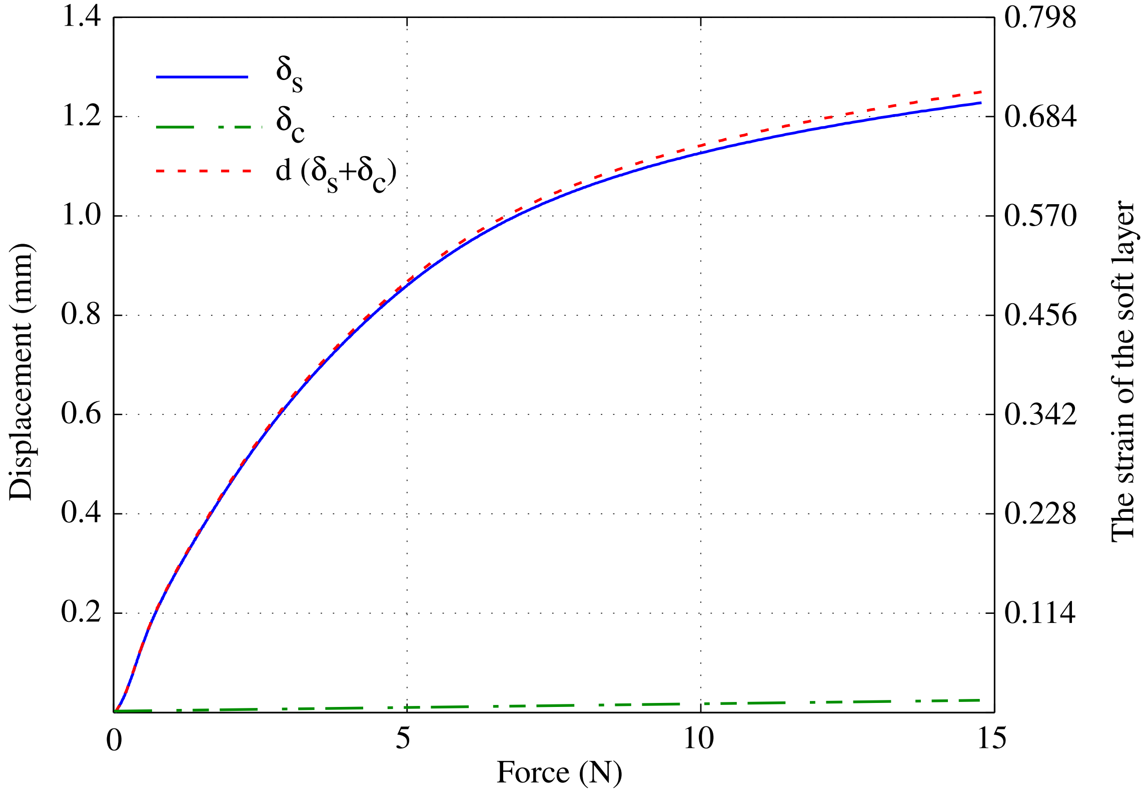

Figure 7.16: An example of displacement distribution in the composite model where $L_c = 15.79\,mm$, $L_s = 1.754\,mm$, $A = \pi(1\times10^{-3})^2\,m^2$, $E_c = 3.5\,GPa$, δ_c is calculated by equation (7.7), δ_s is transformed from the experimental results shown in Figure 7.5 by equations $\delta_s = \varepsilon L_s$ and $F = \sigma A$, and $d = \delta_c + \delta_s$.

d, is discussed instead of the radius of contact area, a, to simplify. The relationship between the vertical displacement, d, and the radius of contact area, a, can be geometrically explained as shown in Figure 7.17 and equation (7.11.)

$$R_0^2 = (R_0 - d)^2 + a^2 \tag{7.11}$$

In addition, the power-law equation can be re-arranged by geometric transformation and assuming $d \ll R_0$ in equation (7.12) [29].

$$d = \left(\frac{c^2}{2R_0}\right) N^{2\gamma} \tag{7.12}$$

Therefore, in general, the properties of the soft layer are dominant in the parameters of the power-law equation, c and γ, until the soft layer is compressed into the half thickness of the initial thickness, $\varepsilon_s < 0.5$.

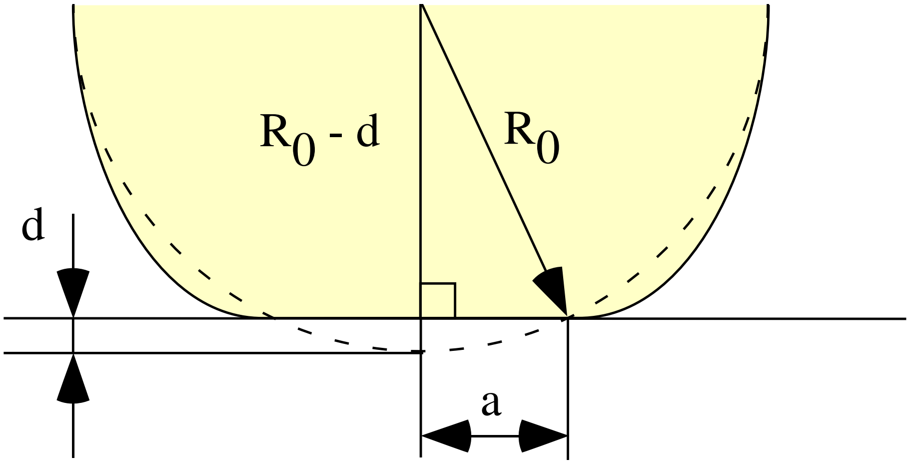

Figure 7.17: The geometric relationship between the vertical displacement *d* and the contact radius *a*

7.3.1 Design criteria for soft fingers with a core

In most of the cases, it is assumed that the effect of the soft layer is only increasing the coefficient of friction, but as previously discussed, the thin soft layer dramatically changes the behavior of the contact interfaces because of the strain concentration in the soft layer. Therefore, design criteria for the thickness of the soft layer is necessary.

As shown in Figure 7.13, the thinner soft layer has lower γ and if the γ is small, the radius of contact area, a, will quickly increase in the beginning and thereafter increase slowly as shown in Figure 7.18. If the contact area is nearly constant, one variable can be removed and it makes controller design easier. From this point of view, a thinner soft layer is better. However, the larger contact area with the thicker soft layer also has advantages, such as decrease the contact pressure. or instance, when holding a fragile object, such as an egg, it is very important to decrease the contact pressure by increasing the contact area. Therefore, a design criterion to decide the thickness of the soft layer is as follows. First, determine the maximum contact radius, a_{max}, based on the contact pressure which will not damage target objects. Then, decide the thickness of the soft layer to the contact radius, a, becomes a_{max} when the vertical displacement, d, is half of the thickness of the soft layer, t, as shown in Figure 7.19. The effects of the thin soft layer is more than an increase of the coefficient of friction only and it is very important to analyze the contact behavior, such as contact forces and slippage conditions. However, usually, the soft layer is applied based on intuition, so a more detailed theoretical analysis is necessary and this will be an interesting topic in the manipulation of soft robot fingers.

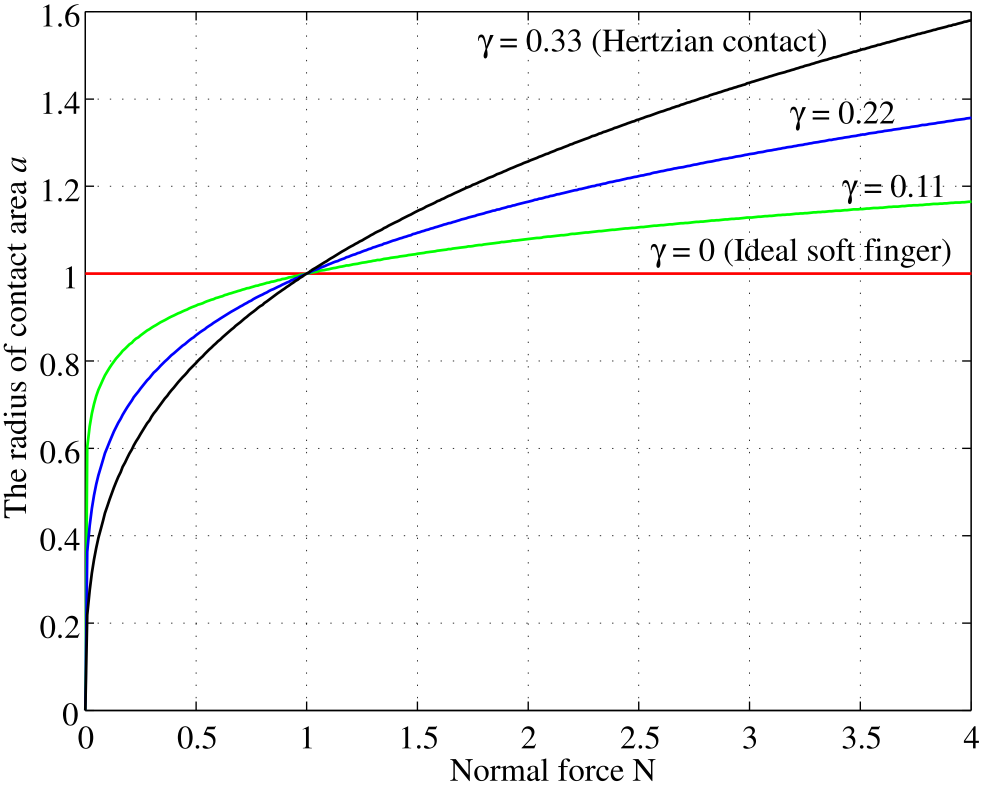

Figure 7.18: The effects of the coefficient γ on the power-law equation

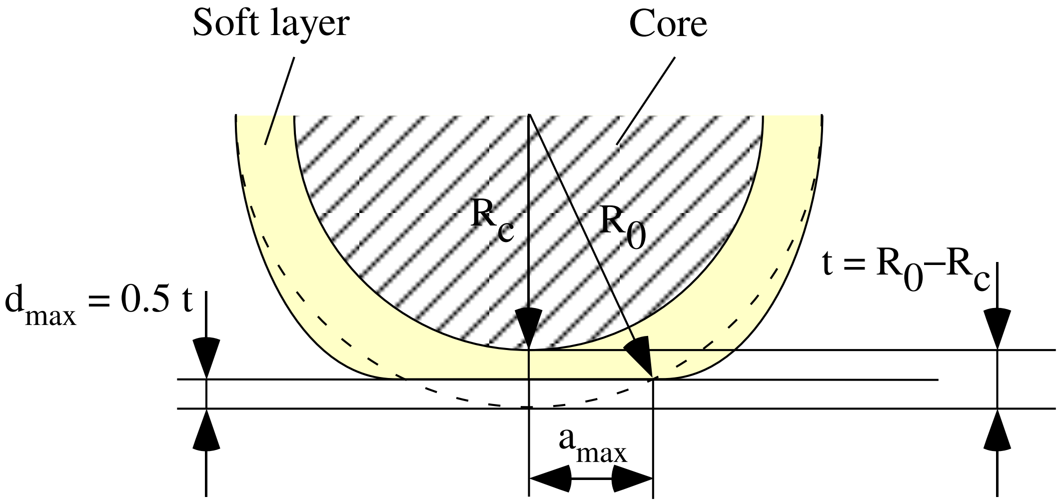

Figure 7.19: An example to how to decide the thickness of the soft layer

Chapter 8

Contact Interface Analysis and Stiffness-based Biomedical Diagnoses with Sensing Technology for a Better Quality of Life

8.1 Introduction

The modeling of contact interface, which is the interface in which two entities are brought to interact with each other, is crucial in the understanding of robotics and biomedical research where such interface will determine important engineering properties. The contact interface presented in this dissertation can be broken into two categories:

- direct contact, or
- non-direct contact.

The modeling and analysis of direct contact interface and non-direct contact interface are presented in this dissertation, using the modeling and analysis:

(1) Direct contact interface modeling: as applied in the analysis and experimental study of bio-inspired artificial skins using strain gages or CNT piezo-resistive sensors

(2) Non-contact contact interface modeling: as applied in the modeling and analysis for the measurement of IOP using the air-puff tonometry

The modeling and analysis include stiffness analysis, static and dynamic modeling, frequent responses, relationship between force and displacement, pressure distribution at the contact interface, viscoelastic properties, tactile sensing, signal processing, and others. The techniques presented in this dissertation are relevant to the applications in biomedical analysis and robotic modeling.

Accurate analysis and modeling of stiffness of human organs or tissues are important in biomedical diagnoses and robotic analysis. For instance, tumor tissues are stiffer than normal tissues and patients with higher Intra-Ocular Pressure (IOP), pressure and stiffness of eyeballs, have higher risk of glaucoma. These diseases can be detected based on the stiffness of human organs or tissues through contact interface modeling.

8.2 Stiffness at the contact interface

Stiffness considered here is different from typical stiffnesses used in mechanical engineering such as spring constant or Young's modulus, and cannot be measured by typical testing machines such as tensile testing machine (*e.g* Fig. 7.8). Therefore, specific modeling of contact interface with appropriate sensing technologies are necessary to measure the stiffness of human organs or tissues, especially when applied in vivo examination such as IOP measurement.

In principle, the stiffness is determined by an applied force and the corresponding deformation. For instance, in the measurement of IOP using the Goldmann applanation tonometry (GAT), an external force is applied directly on the cornea by a probe and the deformation of the cornea is observed by the prescribed diameter of the contact interface. In the case of an air-puff tonometry, an external force is applied on the cornea, not through direct contact interface, but by an air puff which deforms the cornea surface from which the deformation of the cornea is observed by the infrared light reflected from the deformed cornea. In vivo examination, the contact interface where an external force is applied is not flat uniform surface and the contact pressure on the contact interface is not uniform.

Therefore, the analysis and modeling of the contact interface is necessary to estimate the stiffness by the relationship between an applied force and the deformation as presented in Chapters 2 and 3.

Human organs or tissues show time-dependent viscoelastic response, as proposed by Y. C. Fung [6]; therefore, the modeling of the viscoelastic property is important in diagnoses. As an example, the viscoelastic property in IOP measurement can be measured by the ocular response analyzer (ORA), manufactured by Reichert Inc., which is similar to air-puff tonometry [89]. Better understanding of viscoelastic property of soft materials as the contact interface and the proper sensing technologies are necessary for the modeling and analysis in diagnosis involving contact interface. The Fung's model was extended to viscoelastic contact interface by Tsai and Kao and viscoelastic responses are studied by observing the deformation patterns [90]. In this dissertation, the study of viscoelastic responses are furtherer extended by embedding sensing elements in soft materials, as presented in Chapters 4 and 5. In addition, the sensing technology to detect the viscoelastic behavior is studied inspired by human tactile sensing.

8.3 Direct contact and bio-inspired sensing at the contact interface

Human fingertips are excellent for tactile sensing. Experienced physicians can make diagnosis by touching a patient's body and feeling the stiffness and sense the viscoelasticity. As another example, when touching mattresses or pillows made from viscoelastic foam manufactured by Tempur-Pedic Inc., humans can sense the viscosity although it is difficult to express in words. If artificial skin sensors can quantify the feeling, it will be useful for the diagnosis of human organs or tissues which also show viscoelastic property. Such quantified data can be used to enhance the analysis and help in diagnosis.

In addition, artificial skin sensors can be attached to a tip of endoscope to measure the stiffness of human organs or tissues located in the places where surgeons' fingertips are difficult to access. The development of new sensing technology by analyzing and modeling of contact interface can enhance the biomedical diagnosis base on stiffness. With better biomedical diagnosis, diseases can be detected in early stage and treated successfully. Health care is important part of the quality of life; thus, new sensing technologies based on the advances in modeling and analysis of contact interface is important for better quality of life.

8.4 Summary

The modeling and analysis of contact interface, either direct or non-direct contact interface, are presented with applications in the air-puff tonometry (non-direct contact) and bio-inspired skin sensing. Both theoretical modeling and experimental analysis are studied and discussed.

Chapter 9

Proposed Future Work

The CNT-based tactile sensor presented in Chapter 6 showed promising results. Thus, the fabrication of soft fingertips which can detect the slippage at the contact interface and dexterous manipulation by the CNT-based fingertips are proposed. It is known that humans are controlling grasping force by detecting the initiation of slippage between fingertips and grasped objects. For instance, the grasping force is increased when the initiation of slippage is detected. This strategy is suitable for minimizing the grasping force and preventing the damage in the grasped objects. Therefore, the robot hands with the soft fingertips sensitive to the initiation of slippage can enhance the dexterity and prehension.

To this end, the sensitivity to shear force has to be examined by applying shear force on the CNT layer and analyzing the output signals. In the previous experiments, the types of applied force are limited, so applying different types of stimuli to the CNT-based sensors to study the response is necessary for the better understanding of the sensor design. It is known that the output signals from the tactile sensors show characteristic patter during the initiation of slippage where the stick-and-slip takes place in the contact interface. From the experimental results shown in Chapter 6, the CNT-based sensor is more sensitive when external stimuli is dynamic, instead of static stimuli, are applied which is the characteristic of Fast-Adapting (FA) mechanoreceptor as shown in Fig. 4.2. Therefore, CNT-based sensors are expected to have excellent sensitivity for the initiation of slippage.

In addition to the study of the sensitivity to shear force, a fingertip can be fabricated by spraying diluted CNTs on a hemispherical soft material as shown in Fig. 9.1. In this case, a protective layer is necessary to prevent the surface wear of the CNT layer. Ideally, the protective layer works as the epidermis in the human skin and emphasizes the external stimuli. The manufacturing process and the pattern of the surface of the protective layer should be studied. In Chapter 4, the strain gages embedded in soft material showed some good responses, such as those for dynamic stimuli, although the stiffness mismatch caused some issues. Thus, strain gages may work properly if they are put on the rigid plate and deep in the soft material as shown in Fig. 9.1. The strain gages are expected to work in a manner similar to Ruffini or Pacinian in human skin. Different types of configuration, such as the thicknesses of CNT layer and protective layer, should be tested for better sensitivity.

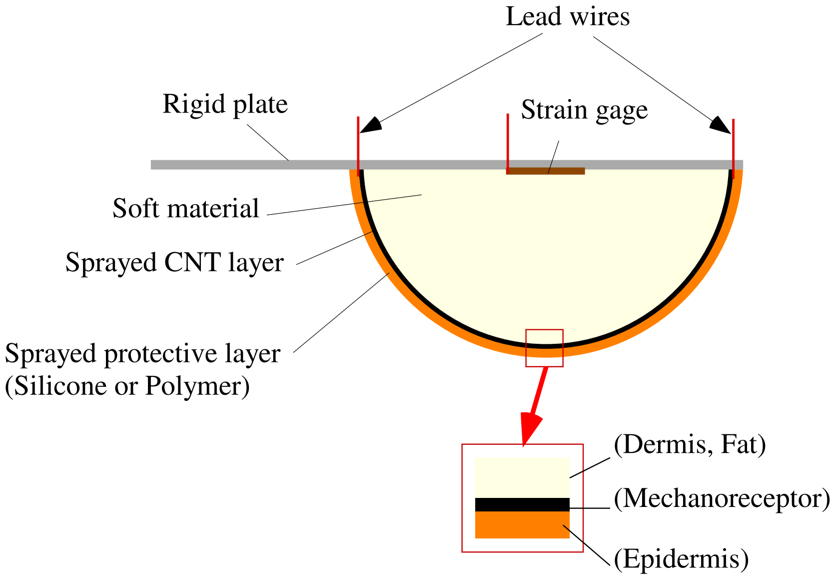

Figure 9.1: Fabrication of artificial soft fingertip with CNT-based tactile senor

As discussed in Chapter 7, soft fingertips have advantages in grasping and manipulation. If we can add sensing elements near the contact interface, the tactile sensitivity necessary for manipulation can be enhanced. In general, placing sensing elements near the stimuli can improve the sensitivity. However, stiffness mismatch can cause problems in soft material if typical stiff sensing elements, such as strain gage or load cell, are placed in near the stimuli. When the sensing elements are located far away from the contact interface, such as the location of the strain gage shown in Fig. 9.1 [91], the sensitivity and accuracy are not good. The CNT- based tactile sensors can resolve these issues and can be located near the contact interface. The sensing elements near the contact interface make it possible to detect the stimuli. For instance, Meissner and Merkel's disk located near the surface of human skin can detect stimuli that Pacinian and Ruffini located far from the surface of human skin cannot detect. Therefore, the manipulation by bio-inspired soft fingertips, as shown in Fig. 9.2, is an interesting topic for further study.

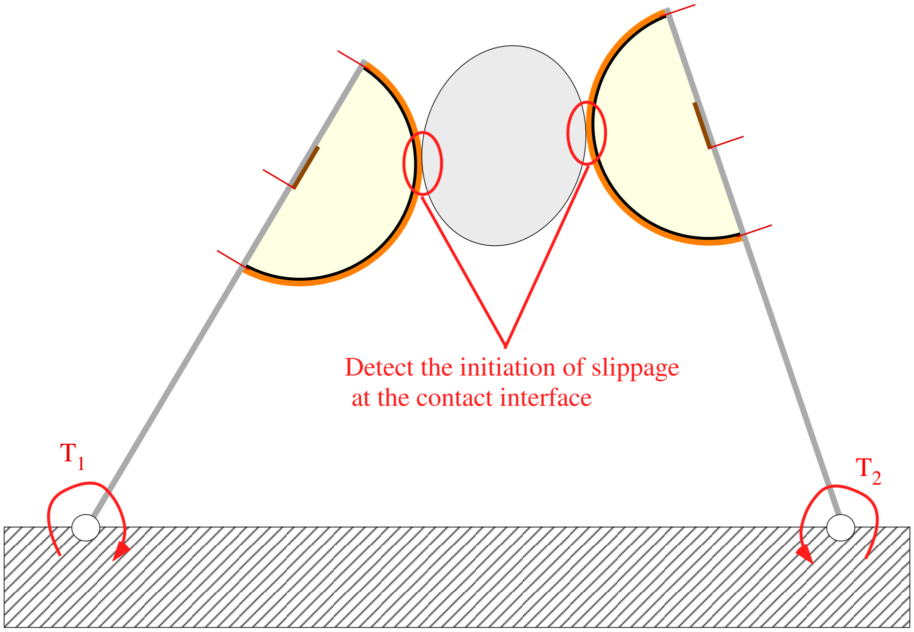

Figure 9.2: Grasping and manipulation by the soft fingertips with CNT-based tactile sensor which can detect the slippage at contact interface

Bibliography

[1] D. Purves, G. Augustine, D. Fitzpatrick, L. Katz, A. LaMantia, J. McNamara, and S. Williams, editors. *Neuroscience*. Sinauer Associates, Inc, 2nd edition, 2001.

[2] Y. Kurita, Y. Iida, R. Kempf, M. Kaneko, H. K. Mishima, H. Tsukamoto, and E. Sugimoto. Dynamic sensing of human eye using a high speed camera. In *IEEE Int. Conf. on Information Acquisition*, pages 338–343, Hong Kong and Macau, China, June 2005.

[3] M. Kaneko, R. Kempf, Y. Kurita, Y. Iida, H. K. Mishima, H. Tsukamoto, and E. Sugimoto. Measurement and analysis of human eye excited by an air pulse. In *IEEE Int. Conf. on Multisensor Fusion and Integration for Intelligent Systems*, pages 353–358, Heidelberg, Germany, September 2006.

[4] RS. Johansson and AB Vallbo. Tactile sensory coding in the glabrous skin of the human hand. *Trends in Neuroscience*, 6, 1983.

[5] M. Konyo, M. Nakamoto, T. Maeno, and S. Tadokoro. Reflective grasp force control of humans induced by distributed vibration stimuli on finger skin with icpf actuators. *TVRSJ*, 11(1):3–10, 2006.

[6] Y. C. Fung. *Biomechanics: Mechanical Properties of Living Tissues*. Springer-Verlag, 1993.

[7] S. Patel and W. Illahi. Non-contact tonometry over soft contact lenses: effect of contact lens power on the measurement of intra-ocular pressure. *Contact Lens & Anterior Eye*, 27:33–37, 2004.

[8] S. Patel and G. Stevenson. Influence of lens material and intra-ocular pressure on the outcome of non-contact tonometry over soft contact lenses. *Contact Lens & Anterior Eye*, 32:68–72, 2009.

[9] PG. Firat, C. Cankaya, S. Doganay, M. Cavdar, S. Duman, E. Ozsoy, and B. Koc. The influence of soft contact lenses on the intraocular pressure measurement. *Eye*, 26:278–282, 2012.

[10] M.S. Insler and R.G. Robbins. Intraocular pressure by noncontact tonometry with and without contact lenses. *Arch Ophthalmol*, 105:1358–1359, 1987.

[11] C.W. McMonnies. Noncontact tonometry through soft contact lenses. *Am J Optom Physiol Opt*, 63:948–951, 1986.

[12] Y. Liu, J Huang, I. Wang, F. Hu, and Y. Hou. Intraocular pressure measurement with the noncontact tonometer through soft contact lenses. *J. of Glaucoma*, 20(3):179–182, 2011.

[13] K. Ogbuehi. The influence of lens power and center thickness on the intraocular pressure measured through soft lenses: A comparison of two noncontact tonometers. *Contact Lens & Anterior Eye*, pages 118–128.

[14] G.K. Krieglestein, W.K. Waller, H. Reimers, and M.E. Langham. Augeninnendruckmessung auf weichen kontaktlinsen. *Graefes Arch Clin Exp Ophthalmol*, 199:223–229, 1976.

[15] G.D. Scibilia, W.H. Ehlers, and P.C. Donshik. The effects of therapeutic contact lenses on intraocular pressure measurement. *Contact Lens Association of Ophthalmologists*, 22:262–265, 1996.

[16] J.B. Rubenstein and T.A. Deutsch. Pneumatonometry through bandage contact lenses. *Arch Ophthalmol*, 103:1660–1661, 1985.

[17] J. Liu and C. J. Roberts. Influence of corneal biomechanical properties on intraocular pressure measurement: Quantitative analysis. *J. Cataract Refract Surg*, 31:146–155, 2005.

[18] G. J. Orssengo and D. C. Pye. Determination of the true intraocular pressure and modulus of elasticity of the human cornea in vivo. *Bull. Math. Biol.*, 61:551–572, 1999.

[19] A. Elsheikh, D. Alhasso, and D. Pye. Goldmann tonometry correction factors based on numerical analysis. *J. of Biomech. Eng.*, 131:111013–111021, November 2009.

[20] M. Kohlhaas, A. G. Boehm, E. Spoerl, A. Pürsten, H. J. Grein, and L. E. Pillunat. Effect of central corneal thickness, corneal curvature, and axial length on applanation tonometry. *Arch Ophthalmol.*, 124(4):471–476, 2006.

[21] N. Feltgen, D. Leifert, and J. Frunk. Correlation between central corneal thickness, applanation tonometry and direct intracameral iop readings. *Br. J. of Ophthalmol.*, 85:85–87, 2001.

[22] Thor Eysteinsson, Fridbert Jonasson, Hiroshi Sasaki, Arsaell Arnarsson, Thordur Sverrisson, Kazuyuki Sasaki, Einar Stefánsson, and Reykjavik Eye Study Group. Central corneal thickness, radius of the corneal curvature and intraocular pressure in normal subjects using non-contact techniques: Reykjavik eye study. *Acta Ophthalmologica Scandinavica*, 80(1):11–15, 2002.

[23] P-A Tonnu, T Ho, T Newson, A El Sheikh, K Sharma, E White, C Bunce, and D Garway-Heath. The influence of central corneal thickness and age on intraocular pressure measured by pneumotonometry, non-contact tonometry, the tono-pen xl, and goldmann applanation tonometry. *Br. J. of Ophthalmol.*, 89(7):851–854, 2005.

[24] M. Kaneko, K. Tokuda, and Tomohiro Kawahara. Dynamic sensing of human eye. In *Proc. IEEE Int. Conf. on Robotics and Automation*, pages 2871–2876, Barcelona, Spain, April 2005.

[25] Kelechi C Ogbuehi. Assessment of the accuracy and reliability of the topcon ct80 non-contact tonometer. *Clinical and Exp.Optometry*, 89(5):310–314, 2006.

[26] S. Boyd and L. Vandenberghe. *Convex Optimization*. Cambridge Univ. Press, 7th edition, 2009.

[27] Y. Kurita, R. Kempf, Y. Iida, J. Okude, M. Kaneko, H. Mishima, H. Tsukamoto, E. Sugimoto, S. Katakura, K. Kobayashi, and Y. Kiuchi. Contact-based stiffness sensing of human eye. *IEEE Transaction on Biomedical Engineering*, 55(2), February 2008.

[28] Loenard Meirovitch. *Fundamentals of vibration*. McGrawHill, 1 edition, 2001.

[29] I. Kao and F. Yang. Stiffness and contact mechanics for soft fingers in grasping and manipulation. *the IEEE Trans. of Robotics and Automation*, 20(1):132–135, February 2004.

[30] M. H. Lee and H. R. Nicholls. Tactile sensing for mechatronics - a state of theart survey. *Mechatronics*, 9:1–31, 1999.

[31] Y. Zhang, Y. Mukaibo, and T. Maeno. A multi-purpose tactile sensor inspired by human finger for texture and tissue stiffness detection. In *Proc. IEEE Int. Conf. on Robotics and Biomimetics*, pages 159–164, 2006.

[32] P. Puangmali, K. Althoefer, L. Seneviratne, D. Murphy, and P. Dasgupta. Sensing for minimally invasive surgery. *IEEE Sensors Journal*, 8:371–381, 2008.

[33] V. J. Lumelsky, M. S. Shur, and S. Wagner. Sensitive skin. In *IEEE Sensor J., vol. 1, no. 1*, pages 41–51, 2001.

[34] Y. Hidaka, Y. Shiokawa, K. Tashiro, T. Maeno, and M. Konyo. Development of an elastic tactile sensor emulating humangfingers for tele-presentation systems. In *Proc. IEEE SENSORS Conference*, pages 1919–1922, 2009.

[35] S. Takamuku, K. Hosoda G. Gomez, and R. Pfeifer. Haptic discrimination of material properties by a robotic hand. In *In IEEE Int. Conf. on Development and Learning, ICDL*, pages 1–6, 2007.

[36] T. Mukai, M. Onishi, T. Odashima, S. Hirano, and Z. Luo. Development of the tactile sensor system of a human-interactive robot ”ri-man”. In *IEEE Tran. on robotics, vol. 24, no. 2*, pages 505–512, 2008.

[37] M. Shimojo, A. Namiki, M. Ishikawa, R. Makino, and K. Mabuchi. A tactile sensor sheet using pressure conductive rubber with electrical-wires stitched method. In *IEEE Sensor J., vol. 4, no. 5*, pages 589–596, 2004.

[38] T. G. Beckwith, R. D. Marangoni, and J. H. Lienhard. *Mechanical measurement*. Addison Wesley publishing company, 1993.

[39] P.S. Theocaris and N. Papadopoulou. Propagation of stress waves in viscoelastic media. *Polymer*, 19(2):215 – 219, 1978.

[40] D. Turhan and Y. Mengi. Propagation of initially plane waves in nonhomogeneous viscoelastic media. *International Journal of Solids and Structures*, 13(2):79 – 92, 1977. NONHOMOGENEOUS VISCOELASTIC MEDIA;WAVE PROPAGATION;.

[41] Paul Stucky and William Lord. Finite element modeling of transient ultrasonic waves in linear viscoelastic media. *IEEE Transactions on Ultrasonics, Ferroelectrics, and Frequency Control*, 48(1):6 – 16, 2001. Linear viscoelastic media;.

[42] J.M. Pereira, J.J. Mansour, and B.R. Davis. Dynamic measurement of the viscoelastic properties of skin. *Journal of Biomechanics*, 24(2):157 – 162, 1991. Collagen Network;Dynamic Wave Propagation Method;Proteoglycan Gel;Skin Strain Properties;Skin Viscoelastic Properties;.

[43] R. Fowles and R. F. Williams. Plane stress wave propagation in solids. *Journal of Applied Physics*, 41(1):360 – 363, 1970.

[44] W. Flugge. *Viscoelasticity*. Blaisdell Publishing Company, 1967.

[45] N. Sakamoto, M. Higashimori, T. Tsuji, and M. Kaneko. An optimum design of robotic hand for handling a visco-elastic object based on maxwell model. In *Proc. IEEE Int. Conf. on Robotics and Automation, ICRA 2007*, pages 1219–1225, Roma, Italy, April 10-14 2007.

[46] D. T. V. Pawluk and R. D. Howe. Dynamic contact of the human fingerpad against a flat surface. *ASME Jour. of Biomechanical Engineering*, vol. 121(6):605–611, 1999.

[47] R. D. Howe, N. Popp, I. Kao, P. Akella, and M. R. Cutkosky. Grasping, manipulation, and control with tactile sensing. In *Proc. IEEE Int. Conf. on Robotics and Automation, ICRA*, Cincinnati, OH, 1990.

[48] K. B. Shimoga and A. A. Goldenberg. Soft robotic fingertips - part I and II: A comparison of construction materials. *Int. Jour. of Robotic Research*, 15(4), 1996.

[49] F. Barbagli, A. Frisoli, K. Salisbury, and M. Bergamasco. Simulating human fingers: a soft finger proxy model and algorithm. In *Proc. IEEE Int. Symp. on Haptic Interface, HAPTICS'04*, 2004.

[50] Y. Li and I. Kao. A review of modeling of soft-contact fingers and stiffness control for dextrous manipulation in robotics. In *Proc. IEEE Int. Conf. on Robotics and Automation, ICRA*, pages 3055–3060, Seoul, Korea, 2001.

[51] H. Takagi, M. Takahashi, R. Maeda, Y. Onishi, Y. Iriye, T. Iwasaki, and Y. Hirai. Analysis of time dependent polymer deformation based on a viscoelastic model in thermal imprint process. *Microelectronic Engineering*, 85:902–906, 2008.

[52] T. Inoue and S. Hirai. Elastic model of deformable fingertip for soft-fingered manipulation. *IEEE Trans. in Robotics*, 22:1273–1279, 2006.

[53] T. Inoue and S. Hirai. Quasi-static manipulation using hemispherical soft fingertips by means of minimum d.o.f. two-fingered robotic hand. *J. of the Robotics Society of Japan*, 24:945–953, 2006.

[54] M. Kimura, Y. Sugiyama, S. Tomokuni, and S. Hirai. Constructing rheologically deformable virtual objects. In *Proc. IEEE Int. Conf. on Robotics and Automation, ICRA*, pages 3737–3743, 2003.

[55] W. N. Findley and J. S. Y. Lay. A modified superposition principle applied to creep of non-linear viscoelastic material under abrupt changes in state of combined stress. *Trans. of the Society of Rheology*, vol. 11(3):361–380, 1967.

[56] D. B. Adolf, R. S. Chambers, and J. Flemming. Potential energy clock model: Justification and challenging predictions. *Journal of Rheology*, 51(3):517–540, 2007.

[57] A. Z. Golik and Y. F. Zabashta. a molecular model of creep and stress relaxation in crystalline polymers. *Mekhanika Polimerov*, pages 969–975, 1971.

[58] P. Tiezzi and I. Kao. Modeling of viscoelastic contacts and evolution of limit surface for robotic contact interface. *IEEE Transaction on Robotics*, 23(2):206–217, April 2007.

[59] P. Tiezzi, I. Kao, and G. Vassura. Effect of layer compliance on frictional behavior of soft robotic fingers. *Advanced Robotics*, 21(14):1653–1670, 2007.

[60] P. Tiezzi and I. Kao. Characteristics of contact and limit surface for viscoelastic fingers. In *IEEE Int. Conf. on Robotics and Automation, ICRA 2006*, pages 1365–1370, Orlando, Florida, May 15-19 2006.

[61] P. Tiezzi, I. Kao, and G. Vassura. Effect of layer compliance on frictional behavior of soft robotic fingers. In *Proc. IEEE Int. Conf. on Intelligent Robots and Systems (IROS 2006)*, pages 4012–4017, Beijing, China, October 2006.

[62] N. Xydas and I. Kao. Modeling of contact mechanics and friction limit surface for soft fingers in robotics, with experimental results. *Int. J. of Robotic Research*, 18(8):941–950, 1999.

[63] N. Xydas and I. Kao. Modeling of contacts and force/moment for anthropomorphic soft fingers. In *Proc. of Int. Conf. on Intelligent Robots and Systems, IROS*, pages 488–493, Victoria, Canada, 1998.

[64] C. D. Tsai, I. Kao, N. Sakamoto, M. Higashimori, and M. Kaneko. Applying viscoelastic contact modeling to grasping task: an experimental case study. In *International Conference on Intelligent Robots and Systems, IROS*, pages 1790–1795, September 2008.

[65] C. D. Tsai and I. Kao. The latency model for viscoelastic contact interface in robotics: Theory and experiments. In *Proc. 2009 IEEE Int. Conf. on Robotics and Automation (ICRA 2009)*, pages 1291–1296, Kobe, Japan, May 2009.

[66] C. D. Tsai, I. Kao, K. Yoshimoto, M. Higashimori, and M. Kaneko. An experimental study and modeling of loading and unloading of nonlinear viscoelastic contacts. In *International Conference on Intelligent Robots and Systems, IROS*, pages 3737–3743, St. Louis, USA, October 2009.

[67] C. D. Tsai, I. Kao, A. Shibata, K. Yoshimoto, M. Higashimori, and M. Kaneko. Experimental study of creep response of viscoelastic contact interface under force control. In *International Conference on Intelligent Robots and Systems, IROS*, pages 4275–4280, Taipei, Taiwan, October 2010.

[68] C. D. Tsai, J. Nishiyama, I. Kao, M. Higashimori, and M. Kaneko. Study of the relationship between the strain and strain rate for viscoelastic contact interface in robotic grasping. In *International Conference on Intelligent Robots and Systems, IROS*, pages 592–597, Taipei, Taiwan, October 2010.

[69] I. Kang, M. J. Schulz, J. H. Kim, V. Shanov, and D. Shi. A carbon nanotube strain sensor for structural health monitoring. *Smart Mater. Struct.*, 15, 2006.

[70] K. J. Loh, J. P. Lynch J. Kim, N. W. S. Kam, and N. A. Kotov. Multifunctional layer-by-layer carbon nanotube-polyelectrolyte thin films for strain and corrosion sensing. *Smart Mater. Struct.*, 16:429–438, 2007.

[71] M. Park, H. Kim, and J. P Youngblood. Strain-dependent electrical resistance of multi-walled carbon nanotube/polymer composite films. *Nanotechnology*, 2008:055705, 2008.

[72] S. M. Vemuru, R. Wahi, S. Nagarajaiah, and P. M. Ajayan. Strain sensing using a multiwalled carbon nanotube film. *J. Strain Analysis*, 44:555–562, 2009.

[73] S. Teshigawara, K. Tadakuma, A. Ming, M. Ishikawa, and M. Shimojo. Development of high-sensitivity slip sensor using special characteristics of pressure conductive rubber. In *Proc. IEEE Int. Conf. on Robotics and Automation (ICRA)*, pages 3289–3294, 2009.

[74] A. Schmitz, M. Maggiali, L. Natale, B. Bonino, and G. Metta. A tactile sensor for the fingertips of the humanoid robot icub. In *Proc. IEEE Int. Conf. on Intelligent Robots and Systems (IROS)*, pages 2212–2217, 2010.

[75] I. Kao. *Quasistatic Manipulation with Compliance and Friction*. PhD thesis, Department of Mechanical Engineering, Stanford University, December 1990.

[76] R. Howe, I. Kao, and M. Cutkosky. Sliding of robot fingers under combined torsion and shear loading. In *Proceedings of 1988 IEEE International Conference on Robotics and Automation*, volume 1, pages 103–105, Philadelphia, Pennsylvania, April 24-29 1988.

[77] S. Goyal, A. Ruina, and J. Papadopoulos. Limit surface and moment function description of planar sliding. In *Proceedings of 1989 IEEE International Conference on Robotics and Automation*, pages 794–799, Scottsdale, Arizona, May 1989.

[78] Suresh Goyal, Andy Ruina, and Jim Papadopoulos. Planar sliding with dry friction: Part 1. limit surface and moment function. *Wear*, 143:307–330, 1991.

[79] Suresh Goyal, Andy Ruina, and Jim Papadopoulos. Planar sliding with dry friction: Part 2. dynamics of motion. *Wear*, 143:331–352, 1991.

[80] I. Kao and M. R. Cutkosky. Dextrous manipulation with compliance and sliding. *International Journal of Robotics Research*, 11(1):20–40, February 1992.

[81] R. D. Howe and M. R. Cutkosky. Practical force-motion models for sliding manipulation. *Int. Jour. of Robotics Research*, 15(6):555–572, 1996.

[82] I. Kao and M. R. Cutkosky. Comparison of theoretical and experimental force/motion trajectories for dextrous manipulation with sliding. *International Journal of Robotics Research*, 12(6):529–534, December 1993.

[83] H. Hertz. *On the Contact of Rigid Elastic Solids and on Hardness*, chapter 6: Assorted Papers by H. Hertz. MacMillan, New York, November 1882.

[84] K. L. Johnson. *Contact Mechanics*. Cambridge University Press, first paperback edition edition, 1985.

[85] ABAQUS. *ABAQUS User Manual, Version 5.7*. Hibbit,Karlsson and Sorensen Inc., Pawtucket, RI, USA, 1997.

[86] P. Raos. Modeling of elastic behavior of rubber and its application in FEA. *Plastics, Rubber and Composites Processing and Applications*, 19:293–303, 1993.

[87] R. P. Bevington. *Data Reduction and Error Analysis for the Physical Sciences*. McGraw-Hill, 1969.

[88] I. Kao, M. R. Cutkosky, and R. S. Johansson. Robotic stiffness control and calibration as applied to human grasping tasks. *IEEE Transaction on Robotics and Automation*, 13(4):557–566, August 1997.

[89] D. A. Luce. Determining in vivo biomechanical properties of the cornea with an ocular response analyzer. *Journal of Cataract and Refractive Surgery*, 31(1):156 – 162, 2005.

[90] C.H. Tsai. *Nonlinear Modeling on Viscoelastic Contact Interface: Theoretical Study and Experimental Validation*. PhD thesis, Stony Brook, 2010.

[91] V.A. Ho, D. V. Dao, S. Sugiyama, and S. Hirai. Development and analysis of a sliding tactile soft fingertip embedded with a microforce/moment sensor. *IEEE Transaction on Robotics*, 27(3):411–424, 2011.